LENS - European Laboratory for Non-linear Spectroscopy

Doctoral Thesis

One dimensional bosons: Atoms to molecules

Author:
Avinash Kumar

Supervisor: Prof. Giovanni Modugno

Coordinator: Prof. Francesco Pavone

Referee: Prof. Gabriele Ferrari

A thesis submitted in fulfilment of the requirements
for the degree of Doctor of Philosophy

in the

Atomic and molecular spectroscopy
XXVI Cycle - FIS/03

April 2014

Dedicated to my mother

Contents

Contents ii

List of Figures iv

Introduction 1

1 One-dimensional bosons with disorder 7
- 1.1 One dimensional bosons and their characteristics . . . 7
  - 1.1.1 Condensation and phase fluctuations . . . 8
  - 1.1.2 Interaction and disorder . . . 10
  - 1.1.3 Theory . . . 14
- 1.2 Preparation of the system . . . 15
  - 1.2.1 Disordered potential . . . 15
  - 1.2.2 Experimental control parameters . . . 16
  - 1.2.3 One-dimensional Bose gas . . . 18
  - 1.2.4 Momentum distribution . . . 20
- 1.3 Dynamics . . . 21
  - 1.3.1 Momentum evolution analysis . . . 22
- 1.4 Clean system . . . 26
- 1.5 Disordered system . . . 28
- 1.6 Conclusions . . . 30

2 Towards ultracold mixture and molecules 36
- 2.1 Long range dipolar interaction . . . 36
  - 2.1.1 Dipolar systems . . . 37
  - 2.1.2 1D Bose gas of polar molecules . . . 38
  - 2.1.3 $^{39}K^{87}Rb$ system . . . 40
- 2.2 Production scheme . . . 40
  - 2.2.1 $^{39}K^{87}Rb$ Feshbach resonance . . . 41
  - 2.2.2 Ground state transfer . . . 41
- 2.3 Simulation of optimal trapping geometaries for a binary Mott insulator of K and Rb atoms . . . 43
  - 2.3.1 Present Experimental Setup . . . 45
  - 2.3.2 Strategies to produce an efficient overlap of K and Rb . . . 49
  - 2.3.3 Calculation of Densities . . . 53
  - 2.3.4 Numerical Simulation . . . 56

2.4 Conclusions 57

3 Realization of an ultrastable laser setup for molecular transfer 61
3.1 Ultracold molecules 61
3.1.1 Coherent transfer scheme 62
3.2 Diode lasers 65
3.2.1 Tuning of primary laser 65
3.3 Scanning the Fabry Perot cavity 70
3.3.1 Optical cavity setup 73
3.4 Pound–Drever–Hall laser frequency stabilization 77
3.4.1 PDH setup scheme 78
3.4.2 Cavity linewidth using the EOM modulation 80
3.4.3 Feedback 81
3.5 Noise spectrum 82
3.5.1 Power spectral density 82
3.5.2 Calculation of line-width 83
3.6 Phase locking 86
3.6.1 Frequency comb 86
3.6.2 Locking scheme 87
3.7 Wavemeter 92
3.7.1 Wavemeter and Frequency comb 94
3.8 Conclusions 94

Acknowledgements 97

List of Figures

1.1 The confining potential for a one dimensional Bose gas. 8
1.2 A one dimensional system of two particles in a box. When their interaction energy exceeds the kinetic energy of each particle, they separate to decrease the interaction; this regime is called Tonks-Girardeau regime . . 11
1.3 The effect of increasing lattice strength on the Wannier wave functions. . 12
1.4 (a) Phase diagram for one dimensional bosons under the interplay of random disorder and interaction (Luttinger parameter)[12]. (b) A similar phase diagram for one dimensional bosons in a lattice with density $n = 1$ [13]. 14
1.5 A lattice potential being perturbed by a secondary lattice to create a quasi-periodic disorder. 15
1.6 The potential for a two body collision. A Feshbach resonance takes place when the energy state of the free atoms E in the open channel V_{bg} resonantly couples with one of the molecular bound states in the closed channel V_c. The energy separation between the two states can be controlled by means of the magnetic field provided that the magnetic moments of the closed and open channel are different. 17
1.7 Scattering length vs magnetic field in the vicinity of ^{39}K Feshbach resonance at 400G. In the work reported in this thesis we exploit the scattering length in the range from 350G (zero crossing) to 400G. 18
1.8 Schematic diagram for experimental realization of a set of 1D quasi-condensates using two strong horizontal lattices and a quasi-periodic lattice superimposed along vertical direction. 19
1.9 A time of flight image of the system shown in figure 1.8 and an averaged momentum distribution of all subsystems obtained by integrating this image along the horizontal. 20
1.10 A cartoon showing the shift in harmonic potential leading to oscillation of the 1D subsystem. 21
1.11 Momentum distribution without kick ($t^* = 0$) and with kick ($t^* = 0.8\mu s$) in a non-disordered lattice with interaction energy $U/J = 1.26$. 22
1.12 Time evolution of peak momentum in a non-disordered lattice with interaction energy $U/J = 1.26$ and density $n = 3.6$. The dot-dashed line is the momentum oscillation without damping. The experimental data points are fitted to the damped oscillation in the starting with $\gamma/2\pi = 135Hz$ and later with $\gamma/2\pi = 600Hz$ 23
1.13 The broadening of the momentum peak after strong damping 23
1.14 The evolution of the momentum (a) and the difference between experimental data and initial damping fit (b) to estimate the critical momentum p_c. 25

1.15 The dependence of critical momentum on the interaction energy U for a non-disordered lattice. The arrow marks the theoretically predicted critical interaction energy for the transition to Mott insulator for $n = 2$. 26
1.16 A plot showing critical momentum versus interaction energy. The dots are experimental data points, dashed-dotted curve is theoretical curve $p_c(U)$ for the quantum phase slip model and the dashed curve is for the thermal phase slip model. 27
1.17 The dependence of initial damping rate on the interaction energy. 28
1.18 Time evolution of momentum at different disorder strengths $\Delta/J = 0$(dots), $\Delta/J = 3.6$ (triangles), $\Delta/J = 10$ (squares) and a fixed interaction energy $U/J = 1.26$. 28
1.19 The critical momentum p_c (dots) and rms width of momentum distribution at equilibrium δp (open circles) versus disorder strength Δ/J at an interaction energy $U/J = 1.26$. The piece wise linear fit (dashed) is to find Δ_c and solid line is a sigmoidal fit of δp 29
1.20 Critical disorder Δ_c/U to enter the insulating phase versus total interaction energy nU/J. The experimental data(dots) are fitted with the curve 1.38. Large error bars are due to error on calibration of disorder (20%). . 30

2.1 Interaction among polar molecules. 37
2.2 Interaction energies of polar molecules inside a one dimensional lattice. U is the on site interaction energy and V is the inter site interaction energy. 38
2.3 Mott insulator phase of polar molecules in a lattice with an occupancy $n = 1$ when $V < U$. 38
2.4 Density wave phase of polar molecules in a lattice with an occupancy $n = 1$ when $V > U$. 38
2.5 Excitation properties of a Mott insulator and a Haldane insulator. 39
2.6 The phases of 1D gas of polar molecules in a lattice under different on-site and itersite interaction strengths as predicted in [8]. 39
2.7 The $\Delta - V$ phase diagram for polar molecules for two kinds of disorder at a fixed interaction energy $U/t = 5$ [8]. 40
2.8 The interspecies Feshbach resonances (left) and $^{39}K^{87}Rb$ molecular levels coupled to atoms (right) setting the energy of free particles at zero. 41
2.9 KRb molecular potentials. 42
2.10 A typical three level system(left) and a pulse sequence for the STIRAP transfer. 42
2.11 The setup of magneto-optic trap. 45
2.12 The MOT has both trapping as well as cooling effect. The atoms moving away from the center of the MOT absorbs photons of red detuned MOT beams and are on average pulled back to the center as well as slowed. . . 45
2.13 The selective evaporative cooling by transferring the high energy Rb atoms at the periphery of the Quic trap from $|F = 2, m_F = -2\rangle$ to $|F = 1, m_F = 1\rangle$, which is no longer trappable and hence lost. 46
2.14 A schematic showing three stages of evaporative cooling. The strength of the trap potential is ramped down to allow the faster atoms to escape, while the slow ones stay trapped. 47
2.15 The required distribution of atoms before they are bound together using a Feshbach resonance. 47
2.16 The distribution of the condensate in the optical trap 48

2.17 The potential and the distribution for the two species in the vertical direction. . . . 48
2.18 Left: Potential depths in vertical direction of K (blue) and Rb (Red) after they condense. Rb is shallower because of its heavy weight. Right: The Thomas Fermi distribution of condensates separated due to the gravitational sag. . . . 49
2.19 Energies of K (solid lines) and Rb (dashed lines) versus the magnetic field in their $F = 1$ and different m_F states. . . . 50
2.20 Left: Potential depths in vertical direction of K (blue) and Rb (Red) after they are condensed in magnetic field gradient of 550 G/m. Right: The condensates of K and Rb significantly overlapping after evaporation. . . . 51
2.21 Fine level scheme of an Alkali atom and the detuning of a frequency ω from the excited state splitting. . . . 51
2.22 Left: Potential depths in vertical direction of K (blue) and Rb (Red) after when both the dipole trap lasers have wavelength 808nm. Right: The overlapping Thomas Fermi distribution of condensates of K and Rb after evaporation. . . . 52
2.23 Left: Potential depths in vertical direction of K (blue) and Rb (Red) after when one of the dipole trap lasers have wavelength 808nm. Right: The overlapping Thomas Fermi distribution of condensates of K and Rb after evaporation. . . . 52
2.24 An approximation of Thomas Fermi distribution $n(x)$ of atoms along one dimension by taking its weighted mean over itself. The approximated distribution $\tilde{n}(x)$ is flat and have less volume to conserve the total number of atoms. . . . 54
2.25 The overlap of the two normalized density distributions. . . . 55
2.26 Tunable input parameters for the simulation. . . . 56
2.27 The output table showing calculation results of averaged trap frequencies, the trap depth, scattering length for K, occupancy in the optical lattice and the ratio of the interaction energy and the scattering energy. . . . 56
2.28 The temperature and the Critical temperature of K and Rb in nK. . . . 56
2.29 The potentials for K (blue) and Rb (red) along the vertical direction. . . . 57
2.30 The distribution of K and Rb along the vertical direction 57

3.1 The difference between the energy of two free K and Rb atoms and the rovibrational ground state. . . . 62
3.2 The transfer scheme from the KRb Feshbach molecules to the rovibrational ground state. . . . 63
3.3 Three level system involved in the STIRAP process. $|a\rangle$ is the weakly-bound Feshbach state, $|b\rangle$ is the excited electronic state and $|g\rangle$ is the absolute ground state of the dimer. . . . 63
3.4 Scheme to phase lock two lasers using a frequency comb reference. The frequency comb used is an Infra red fiber-based comb locked to a radio-frequency reference. . . . 65
3.5 Schematic of an assembly of a diode laser. The light emitted from the diode is get partially reflected back from the grating. The grating and the back end of the diode forms a resonator. The grating angle can be changed coarsely by a screw and precisely by applying voltage across the piezo which is pushing it. . . . 66

3.6 Gain curve, modes of cavity and modes inside the diode. 66
3.7 The wavelength versus the diode current of the laser, keeping all other tuning parameters fixed (T=20 °C). The plot shows one mode jump and a multimode region(missing points). 67
3.8 The wavelength versus the temperature of the laser keeping all other tuning parameters same (Current=113mA). The plot shows many mode jump and multimode region. 68
3.9 The wavelength versus the voltage across the piezo of the laser keeping all other tuning parameters same (T=25 °C, Current=113mA). The plot shows few mode jumps. 69
3.10 A cartoon showing a Fabry Perot Cavity with one plane mirror and the other concave mirror, separated by a distance to have the focus of concave mirror at the plane mirror. 71
3.11 The cavity scan with the laser injected showing the fundamental mode and higher order (transversal) modes. 72
3.12 The cavity under vacuum setup. 74
3.13 The cavity scan with the 1320nm laser injected and well aligned showing the fundamental mode and higher order (transversal) modes. 75
3.14 The transmission lines from the cavity injected with 1320nm wavelength laser. 77
3.15 Schematic of PDH locking loop. 78
3.16 The simulated reflection and PDH signals. 78
3.17 Line width calculation using the side peaks produced by the EOM in the transmission line. 81
3.18 The fluctuations in error signal can be transformed into frequency fluctuations. 82
3.19 Area under the power spectral density curve. 84
3.20 The spectrum of the error signal after the lock with different PID gain values. 84
3.21 The spectrum of the error signal in linear scale the lock with different PID gain values. 85
3.22 Pulse train emitted from a frequency comb with a phase slip of the envelope. 86
3.23 The spectrum of a frequency comb with offset of first frequency mode from zero. 86
3.24 The locking scheme of the two lasers stabilized to an external cavity to an optical frequency comb. 88
3.25 The scheme to access the offset frequency. 89
3.26 Beat unit used to detect the beat between laser and the nearest comb teeth. 89
3.27 Beat signal from the frequency comb beating with 1320nm laser (left) and 855nm laser (right). 90
3.28 The schematic of the phase locking of the laser to the comb. 91
3.29 The phase difference between the beat signal and the reference signal, which changes continuously with time but seen like sawtooth because of the $+/-\pi$ bound on the angle. 91
3.30 The display panel showing the digitized error signal (phase difference) before and after lock. 92

3.31 Schematic diagram of the wavemeter based on moving Michelson interferometer. 92
3.32 The wavemeter reading versus the beat signal with one of the frequency comb lines. From the plot it is clear that we can estimate the frequency of the laser upto an accuracy of ∼50MHz by doing repeated measurements. 93

Introduction

A full understanding of many body quantum systems is one of the challenging problems is physics. These systems exhibit a variety of phases depending on the external potential, interaction among the particles, and their energy scales. In nature these parameters lack perfect order and can show many kind of disorders. These systems are hard to deal with both experimentally and theoretically. In theoretical quantum models, unlike classical ensembles of particles, the Hilbert space grows exponentially with the size of the system and hence makes it difficult to find the exact solutions for the macroscopic systems. Even the best algorithms to date can yield numerical solutions only for one dimensional systems of limited size. In the experiments with traditional ensembles like condensed matter systems, the difficult part is instead to have control over the relevant parameters like interactions, disorder etc.

A major boost in this field was the realization of Bose-Einstein condensation in ultracold dilute gases, in 1995 [1, 2]. A BEC is a coherent, macroscopic matter wave in a system of interacting particles. This is the same property of the particles which gives birth to condensed-matter phenomena like superconductivity and superfluidity. The external potential for a BEC can be made with optical fields and is precisely controllable. The zero temperature scattering resonances allow to control the interactions. These features make a BEC the best candidate to model condensed matter systems and open a new gateway to understand many body quantum systems. The realization of periodic potentials using a off-resonant standing waves, the optical lattices [3, 4], provides a clean, versatile and controllable model of solid-state periodic potentials. The potential strengths can be tuned to be large enough to fragment a three-dimensional gas into lower dimensions. Because of all these wonderful properties, BECs are being employed as quantum simulators of complex many-body problems [5].

The work of my thesis is in this broad field of quantum simulations with ultracold atoms. In particular, I've employed ultracold gases to explore the physics of one-dimensional bosons with interactions and disorder, an outstanding open problem in modern physics.

The properties of a quantum gas depend greatly on the dimensionality of the system. One-dimensional gases show different condensation phenomena, correlation properties and phase fluctuations as compared to 2D or 3D. In the case of bosonic systems, depending on the interaction strength, a 1D Bose gas can show either bosonic or fermionic properties [6]. Thus in condensed matter simulations, one dimensional gases are suitable to study the physics of strongly correlated systems. Another advantage is that 1D systems are relatively simpler to compute. They have established theoretical results and hence their experimental outcomes are theoretically validable.

The effect of external perturbations, particularly disorder, on many body quantum systems has been a topic of interest since fifty years. The main motivation for these studies originated from the interest to understand the effect of imperfections and disorder on the conduction properties of electrons in metals. The disordered potential tends to break the coherence of the system, giving rise to localizations. This phenomenon is called Anderson localization [7, 8]. When studying this phenomenon with quantum gases, the disorder can be added, controlled and quantified in a precise manner.

Interactions among particles play a crucial role in a disordered system. For bosonic particles, interactions screen the effect of disorder and tend to build back the coherence. This study of the interplay between interaction and disorder in quantum gases has recently acquired more attention [9, 10]. Control over the interaction using magnetic Feshbach resonances [11] is greatly advantageous in these experiments. However, atomic gases have only short range contact interactions. A recent advancement in this area was the realization a quantum gas of dipolar molecules with long range dipolar interactions [13, 14]. These type of interactions not only facilitate the research in the direction of condensed matter simulations but also their potentiality in the field of quantum computation.

In this thesis I report the work on quantum simulations with atoms, having short range interactions, and construction and design of a setup for future studies with polar molecules, which might allow similar studies in the presence of long-range interactions. The quantum simulations with atoms were done under controllable disorder and interactions. We tune interactions among atoms using a broad magnetic Feshbach resonance [12]. Interactions greatly influence the quantum phases of a system. However interactions among atoms are contact interactions, which are limited to a certain range. As a next step in the same direction, long range anisotropic interactions, as exhibited by polar molecules, can give rise to many interesting phases. For the purpose to study similar physics with long range interactions, our long term goal is to produce ultracold diatomic molecules using spectroscopy. This spectroscopic process constitutes the combining the degenerate near threshold atoms to deeply bound molecules using two

coherent Raman pulses. One pulse will excite the two atoms to one of their excited molecular state and the other will dump them to the deeply bound molecular state. To do this transfer, I have built a laser setup which will transfer the ultracold atoms to deeply bound molecules. Before combining the atoms we have to arrange the two component mixture to form a double Mott insulator with one pair of different atoms at each lattice site. For this I have done calculations and made computer simulations to find an efficient procedure to achieve a double Mott insulator.

The thesis is organized in three chapters, where I discuss separately the different aspects of the experimental research that constitute my thesis work.

In the first chapter the problem of conduction in disorder is addressed using a 1D Bose gas of ^{39}K atoms. The main motivation of this work was to find the crossovers among phases of one dimensional interacting bosons, under the competition of disorder and interaction strengths. The different phases were explored using the method of transport. As a first part of this investigation, during the transport, the mechanism of breakage of the superfluidity due to phase slip excitations, which leads to an insulating phase is explored. After that the affect of disorder and interaction strength on this crossover was studied. In the measurements the momentum evolution of an oscillating 1D gas is traced till a *critical momentum*, after which the superfluid breaks down due to stronger phase slips. The transition to an insulating phase is marked by the vanishing of the critical momentum. This methodology is first verified for a predicted superfluid to insulator crossover in clean lattice and then used for disordered lattice.

The work reported in second chapter deals with the step towards production of molecules with long range interactions. The production of molecules from an ultracold mixture necessitates the realization of an efficient double Mott insulator. Manipulation of a two component mixture is extremely difficult due their different masses, responses to external potentials and interaction characteristics. For this I wrote a simulation program which simulates the behaviour of a two component BEC in the lattices under our laboratory's trapping conditions. Using this program, as a result, I reported the procedure to achieve a double Mott insulator and simulated outputs.

After having a double Mott insulator, the pairs of atoms will be associated using a magnetic Feshbach resonance and then will be transferred spectroscopically to the deeply bound state. An efficient spectroscopic transfer requires an ultrastable laser system with a line width < 10kHz and a relative phase stability < 1kHz. For this I built a setup to meet the required stability conditions. Typically free running diode lasers have a larger line width (~ 100kHz) and can drift independently from each other. Therefore I line narrowed two diode lasers by locking them to a high finesse cavities. Then to control

their relative stability they were phase locked using a frequency comb. These locking schemes and their results are presented in third chapter.

Bibliography

[1] M. H. Anderson, J. R. Ensher, M. R. Matthews, C. E. Wieman, and E. A. Cornell, *Observation of Bose-Einstein condensation in a dilute atomic vapor*, Science 269(0) 198 (1995).

[2] K. B. Davis, M.-O. Mewes, M. A. Joffe, M. R. Andrews, and W. Ketterle, *Evaporative cooling of sodium atoms*, Phys. Rev. Lett. 74 5202 (1995).

[3] C. Salomon, J. Dalibard, A. Aspect, H. Metcalf, and C. Cohen-Tannoudji, *Channeling atoms in a laser standing wave*, Phys. Rev. Lett. 59, 1659 (1987).

[4] D. Jaksch, C. Bruder, J. I. Cirac, C. W. Gardiner, and P. Zoller, *Cold Bosonic Atoms in Optical Lattices*, Phys. Rev. Lett. 81, 3108-3111 (1998).

[5] Immanuel Bloch, *Ultracold quantum gases in optical lattices*, Nature Physics 1, 23-30 (2005).

[6] Cazalilla MA, Citro R, Giamarchi T, Orignac E, Rigol M, *One dimensional bosons: From condensed matter systems to ultracold gases*, Rev. Mod. Phys. 83, 1405–1466 (2011).

[7] J. Billy, V. Josse, Z. Zuo, A. Bernard, B. Hambrecht, P. Lugan, D. Clément, L. Sanchez-Palencia, P. Bouyer and A. Aspect, *Direct observation of Anderson localization of matter waves in a controlled disorder*, Nature 453, 891-894 (2008).

[8] G. Roati, C. D'Errico, L. Fallani, M. Fattori, C. Fort, M. Zaccanti, G. Modugno, M. Modugno and M. Inguscio, *Anderson localization of a non-interacting Bose–Einstein condensate*, Nature 453, 895-898 (2008).

[9] M. Pasienski, D. McKay, M. White and B. DeMarco, *A disordered insulator in an optical lattice*, Nature Physics 6, 677–680 (2010).

[10] B. Deissler, M. Zaccanti, G. Roati, C. D'Errico, M. Fattori, M. Modugno, G. Modugno and M. Inguscio, *Deolcalization of a disordered bosonic system by repulsive interaction*, Nature Physics 6, 354 - 358 (2010).

[11] C. Chin, R. Grimm, P. Julienne, E. Tiesinga, *Feshbach resonances in ultracold gases*, Rev. Mod. Phys. 82, 1225-1286 (2010)

[12] C. D'Errico, M. Zaccanti, M. Fattori, G. Roati, M. Inguscio, G. Modugno and A. Simoni, *Feshbach resonances in ultracold* ^{39}K, New J. Phys. 9, 223 (2007).

[13] K.-K. Ni, S. Ospelkaus, M. H. G. de Miranda, A. Péer, B. Neyenhuis, J. J. Zirbel, S. Kotochigova, P. S. Julienne, D. S. Jin, and J. Ye, *A high phase-space-density gas of polar molecules*, Science 322, 231 (2008).

[14] K. Aikawa, D. Akamatsu, J. Kobayashi, M. Ueda, T. Kishimoto and S. Inouye, *Toward the production of quantum degenerate bosonic polar molecules,* $^{41}K^{87}Rb$, New J. Phys. 11, 055035 (2009).

Chapter 1

One-dimensional bosons with disorder

The properties of ultracold quantum systems are strongly affected by the dimensionality. Even basic phenomena like Bose Einstein condensation change dramatically shen a system is confined in spatial dimensions lower than three. The change of behavior is particularly dramatic in one dimension (1D), where Bose Einstein condensate (BEC) exists only at $T = 0$ and a collection of bosonic particles can show either bosonic or fermionic properties, depending on the strength of interactions. The effect of disorder is more striking in 1D as compared to 2D and 3D due to large quantum and thermal fluctuations. In a 1D disordered system, at any value of the energy, all states are localized and the localization length increases linearly with the energy of the system. Since interactions can drive the behavior from bosonic to fermionic, it is possible to realize both bosonic and fermionic Bose glass as in 1D.

1.1 One dimensional bosons and their characteristics

In a one dimensional many body system the particles are free along one direction and confined along the other two directions (or radial direction). The wavefunction of a particle in such a potential can be written as

$$\Psi(z, r) = \psi(z)\,\phi(r) \tag{1.1}$$

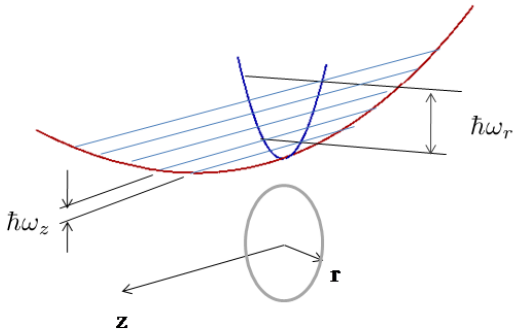

FIGURE 1.1: The confining potential for a one dimensional Bose gas.

Here $\psi(z)$ and $\phi(r)$ are wavefunctions along axial and radial directions respectively. In the case of ultracold gases the confinement can be approximated to be harmonic. Then the wavefunction along the radial direction is

$$\phi(r) \propto e^{-r^2/2a_r} \tag{1.2}$$

where $a_r = \sqrt{\hbar/m\omega_r}$ is the harmonic oscillator length, ω_r is the confining frequency along the radial direction and m is the mass of the particle. The quantized energy levels of the system along this direction have separation $\hbar\omega_r$.

Similarly along the axial direction the particle should ideally be free, but in laboratory is confined with a relatively much small confining frequency ω_z and the energy levels are separated by $\hbar\omega_z$. For a system to be one dimensional the energy separation along redial direction $\hbar\omega_r$ requires to be much larger than $\hbar\omega_z$, interaction energy and temperature. This ensures than the system remains in ground state along the radial direction.

1.1.1 Condensation and phase fluctuations

A general expression of the transition temperature of a non-interacting Bose gas is given by [4]

$$kT_c = \frac{N^{1/\alpha}}{[C_\alpha \Gamma(\alpha)\zeta(\alpha)]^{1/\alpha}} \tag{1.3}$$

here N is the number of particles, α is proportional to dimensionality of the system, the coefficient C_α depends on the geometry of the trap, $\Gamma(\alpha)$ is the gamma function and $\zeta(\alpha)$ is the Riemann zeta function.

In the case of particles in a box, $\alpha = d/2$ and the coefficient C_α takes the form

$$C_\alpha = \frac{Vm^\alpha}{2^{1/2}\pi^2\hbar^3} \tag{1.4}$$

where d is the dimensionality of the system, V is the volume of the system and m is the mass of the particles.

If we consider this system to have a finite size (N and V are finite), then due to the fact that the Riemann zeta function $\zeta(\alpha) \to \infty$ for $\alpha \leq 1$, from equation 1.3 the transition temperature is $T_c = 0$ for both one ($\alpha = 1/2$) and two ($\alpha = 1$) dimensional system.

When the trapping potential is harmonic, the parameter $\alpha = d$ and the coefficient C_α is

$$C_\alpha = \frac{1}{(\alpha-1)!\Pi_i\hbar\omega_i} \tag{1.5}$$

where ω_i are the trap frequencies along i^{th} direction and $i = 1, 2, ..., d$. In this case for finite N only for one dimensional system ($\alpha = d = 1$) the Riemann zeta function diverges and hence, according to equation 1.3, the transition temperature becomes zero.

d	Box	Harmonic
1	T_c=0	T_c=0
2	T_c=0	T_c >0
3	T_c >0	T_c >0

TABLE 1.1: Conditions for BEC in a box and a harmonic trap for different dimensionality of the system.

Above the transition temperature the system has phase fluctuations. For the case of one dimensional system the phase fluctuations increase linearly with the temperature and the length of the system. However, in a finite size system despite of phase fluctuations, a good phase correlation can be achieved even above the transition temperature. For a 1D system with phase fluctuations ($T \neq 0$), the distance within which the phase difference is less than one radian is given by

$$L_\phi = \frac{n_{1D}\hbar^2}{mkT} \tag{1.6}$$

where $n_{1D} = N/L$ is the density of the system, N is the total number of particles, L is the length of the system and k is the Boltzmann constant.

Here we see that by decreasing the temperature T, L_ϕ can be increased to exceed the length of the 1D system L and thus a good phase coherence can be established over the length of the system. The temperature for which the phase is well correlated through out the system, and the system behaves like a true condensate is given by

$$T \ll \frac{T_{1D}}{N} \tag{1.7}$$

here T_{1D} is the degeneracy temperature given by

$$T_{1D} = \frac{\hbar^2}{mk} n_{1D}^2 \tag{1.8}$$

below which the de Broglie wavelength is comparable to the inter-particle separation. At higher temperature the phase fluctuations increase and the system deviates from a true condensate, in this regime it is called a *quasicondensate*.

The correlation function at a finite temperature decays as $g(x) \sim exp(-x/\xi_T)$, where ξ_T is the thermal correlation length. The momentum distribution of such a system is given as

$$p(k) \sim \frac{1}{(2\pi\xi_T(k^2 + (\frac{1}{\xi_T})^2))} \tag{1.9}$$

which is a Lorentzian of width $1/\xi_T$.

1.1.2 Interaction and disorder

A perturbation over the external potential drives an ultracold system through various quantum states. In bosons this effect is shielded by the interaction among the particles. The interplay of disorder and interactions drives the system through various phases. In this section I will give a qualitative overview on the effect of interactions and disorder on a 1D Bose gas.

Interactions in 1D gas

The interactions we will consider in the context of this chapter are short range contact interactions. The general effective two-body interaction in three dimensional system is given by

$$U_{eff}(r, r') = U_0 \delta(r - r') \tag{1.10}$$

where

$$U_0 = \frac{4\pi\hbar^2 a}{m} \tag{1.11}$$

and a is the scattering length of the particles. An interacting 1D Bose gas consisting of N particles can be described by the Hamiltonian

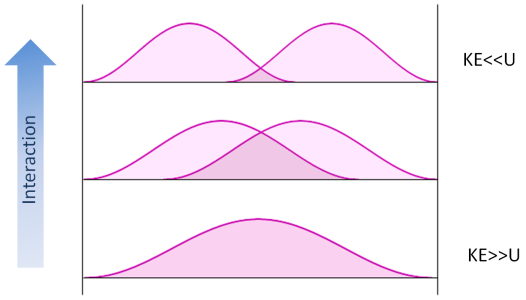

FIGURE 1.2: A one dimensional system of two particles in a box. When their interaction energy exceeds the kinetic energy of each particle, they separate to decrease the interaction; this regime is called Tonks-Girardeau regime

.

$$H = -\sum_{i=1}^{N} \frac{\hbar^2}{2m} \frac{\partial^2}{\partial x_i^2} + \sum_{i,j(i<j)}^{N} U^{(1)} \delta(x_i - x_j) \tag{1.12}$$

where $U^{(1)}$ is the effective interaction in the case of 1D systems, given by

$$U^{(1)} = \frac{U_0}{2\pi a_r^2} \tag{1.13}$$

A 1D Bose gas exhibits a different behaviour for different interaction strengths. At zero and low interactions the system shows a superfluid phase with bosonic properties. However, in contrast, as the interaction strength is increased it shows strongly correlated superfluid phase which has fermionic properties. This regime is called Tonks-Girardeau regime [1–3]. In this regime the interaction energy per particle becomes larger than the kinetic energy and the particles tend to avoid the spatial overlap with neighboring particles in order to reduce the interaction energy.

This behavior is characterized by a dimensionless parameter, the ratio of the interaction energy and the kinetic energy per particle:

$$\gamma = \frac{E_{int}}{E_{kin}} \simeq \frac{2a}{na_r^2}, \tag{1.14}$$

where a is the scattering length and n is the density of the system. For $\gamma \gg 1$ the system goes in the Tonks-Girardeau regime. As the interaction strength tends to be infinite the system behaves as non interacting fermions in 1D. Hence only for a 1D Bose gas by tuning the interactions both bosonic and fermionic characters can be realized.

Periodic potential

Since our motivation in experiments with ultracold gases is to simulate the condensed matter systems, the potential of our interest are *periodic potentials* as in the case of solid state system and *disordered potentials*, or a combination of both.

In the cold atoms experiments the periodic potential is prepared by optical lattices [5–8]. An optical lattice is a periodic variation of the electric field intensity made by a standing wave along one, two or three dimensions. The spatially periodic potential is given by

$$V = \frac{U_0}{2} cos\,(2qx) \tag{1.15}$$

where $q = 2\pi/\lambda$ and U_0 is the lattice potential depth. Usually the lattice strength is measured in terms of the recoil energy($E_r = \hbar^2 q^2/2m$) i.e. $U_0 = sE_r$.

When an optical lattice is superimposed to the BEC, the atoms exhibit different quantum phenomena depending upon the strength of the lattice and their mutual interaction. For small lattice strengths the atoms are completely de-localized throughout the lattice and behave like a superfluid. When the lattice strength is increased, the atoms tend to localize in the minima of the lattice sites decreasing the amount of tunnelling to the neighbouring sites giving rise to the Mott insulator phase.

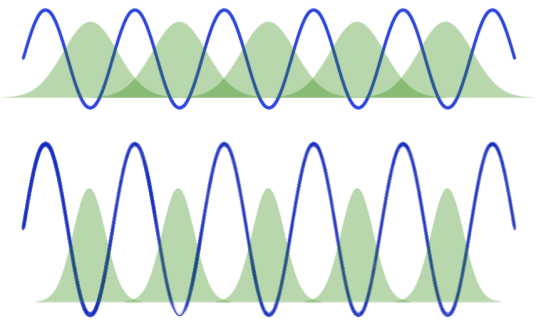

FIGURE 1.3: The effect of increasing lattice strength on the Wannier wave functions.

The model describing the physics of interacting bosons in an optical lattice is the Bose-Hubbard model [4]. This model approximates the minima of the lattice potential to a harmonic oscillator and considers the atoms to be in their lowest quantum state in the sites. Considering the basis of Wannier wave functions and limiting the tunnelling only to the neighbouring sites, the Bose Hubbard Hamiltonian for atoms in a uniform optical lattice can be written as

$$\hat{H}_{BH} = -J \sum_{<i,j>} \hat{a}_i^\dagger \hat{a}_j + U \sum_i \frac{\hat{n}_i(\hat{n}_i - 1)}{2} \tag{1.16}$$

here J is the tunnelling energy, $\hat{a}_i^\dagger$ and $\hat{a}_i$ are boson annihilation and creation operators, U is the on site interaction energy, $\hat{n}$ is the number operator and the sum $< i, j >$ extends only to nearest neighbours. This Hamiltonian comprises of two energy terms whose mutual competition decides the fluid or insulating regime of the system. The first term is a measure of kinetic energy of the particles. This energy term enforces the inter site tunnelling and hence delocalization of the particles throughout the periodic potential which corresponds to a superfluid phase. The second term is a measure of the interaction energy of the particles. This term tends to inhibit the tunnelling and enforces localization in single sites. For a commensurate (integer) filling this transition takes place when the interaction energy becomes larger than the kinetic energy.

$$\frac{E_{int}}{E_{kin}} = \frac{U}{2nJ} \geq 1 \tag{1.17}$$

Here the density n is expressed in terms of particles per site.

Disorder

A disordered potential dramatically affects the properties of a many body system. For a non-interacting system disorder tends to localize the particles at its minima. In the case of non-interacting particles this localization effect is called Anderson localization (AL) [9]. This effect arises from the multiple reflections of a matter waves from random potential barriers. In this localization the wavefunction decays as $|\phi(x)| \propto exp - |x| / \xi$, where the parameter ξ is called the localization length.

Anderson localization in 1D has been experimentally realized with ultracold gases [10, 11]. As the interaction comes into play the system deviates from Anderson localization and go through various phases [12, 14, 15]. This interplay of disorder and interaction is one of the unresolved problems of physics. A comprehensive experimental work on this interplay is under way, how ever in 1D bosonic system the effect of interaction driven de-localization on a disordered system has been reported [16].

In a system of 1D bosons the weak interactions screen the effect of disorder and thus decreases the localization, bringing back the coherence. The system forms locally coherent fragments separated by weak links and this phase is called *Bose glass*. Increasing the interaction these fragments keep joining till global coherence builds and the system becomes a disordered superfluid which has more phase fluctuations. When interactions are increased further the fermionic properties starts showing up and owing to the large interaction, the 1D system again splits into locally coherent fragments and forms a strongly correlated Bose glass. Since the interactions in 1D Bose gas drives behaviour

from bosonic to fermionic as discussed before, at higher interactions this bosonic system behaves like weakly interacting fermions undergoing AL in the disorder. The figure depicts the interaction driven phases in a disordered 1D gas.

1.1.3 Theory

One dimensional quantum gases are relatively simpler and they are theoretically solvable. For last two decades, very effective numerical techniques like *Density Matrix Renormalization Group* (DMRG)[17, 18] have been developed, which yields accurate solutions for quantum many body problem in one dimension.

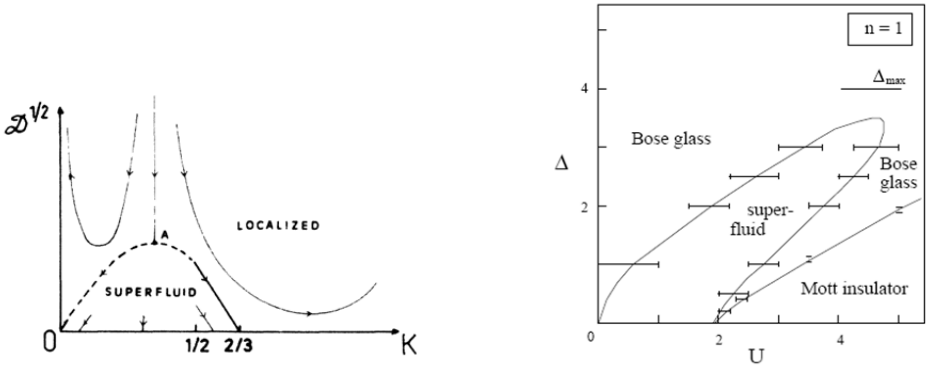

(A) (B)

FIGURE 1.4: (a) Phase diagram for one dimensional bosons under the interplay of random disorder and interaction (Luttinger parameter)[12]. (b) A similar phase diagram for one dimensional bosons in a lattice with density $n = 1$ [13].

Figure 1.4 shows the original theoretical work, predicting the phase diagram for one dimensional bosons. The left figure distinguishes between the superfluid and localized states. A large interaction localizes the system because of repulsions and the system behaves like one dimensional fermions (highly correlated). On the other side, at lower interactions the strength of disorder localizes the system. These are two localized phases having different correlations and separated from the multi-critical point A. At low disorder and within the interaction range $0 < K < 2/3$ there is a region of superfluid phase.

For the case when they are in a lattice with density $n = 1$ the localized phases have Bose glass as well as Mott insulator (MI) phases(figure 1.4b). The MI is separated from the superfluid by the Bose glass. The superfluid phase is inhibited both at higher and lower interactions and appears at moderate interactions.

These theoretical works had been started for one and two decades, but the experimental verification of these results are still to be done. These works makes the experiments with

one-dimensional systems even more appealing, because they make possible to compare experiment and theory, something that is more difficult for higher dimensional systems.

1.2 Preparation of the system

1.2.1 Disordered potential

Experimentally, a disordered potential can be prepared in two ways. One way is to use the potential created by laser speckles [19] field and another one is to create a quasi-periodic lattice.

The disorder we study is prepared by a quasi-periodic lattice. In this system the energies of the minima of a primary lattice are perturbed by super imposing a weak secondary lattice (figure 1.5). This perturbation is maximally randomized by imposing a condition of incommensurability for the two lattices i.e. the ratio of the wave vectors of the lattices $\beta = k_1/k_2$ is an irrational number. The quasi-periodicity of the potential is given by

$$D = \frac{d}{\beta - 1} \tag{1.18}$$

where d is the lattice site spacing of the primary lattice. Our system has a primary laser at a wavelength of 1064nm (Nd:YAG laser) and a secondary laser at a wavelength of 859nm (Ti:Sapphire laser). These wavelengths yield a quasi-periodicity of $4.2d$.

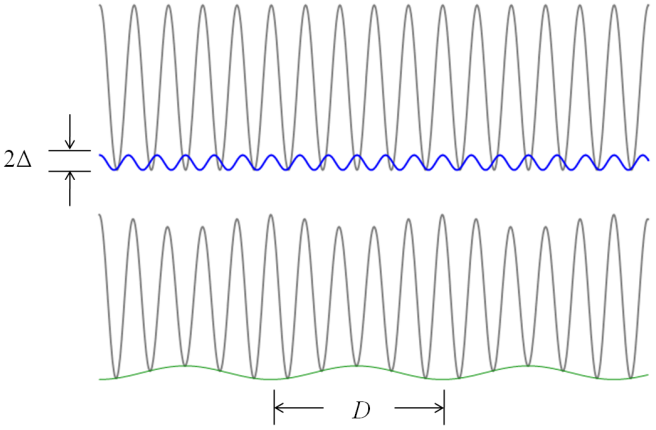

FIGURE 1.5: A lattice potential being perturbed by a secondary lattice to create a quasi-periodic disorder.

To write the Hamiltonian of an interacting Bose gas in quasi-periodic potential an additional energy term corresponding to strength of secondary lattice can be added to

equation 1.16 to obtain the following Hamiltonian

$$\hat{H}_{DBH} = -J \sum_{<i,j>} \hat{a}_i^\dagger \hat{a}_j + \Delta \sum_i cos\left(2\pi\beta i + \phi\right) \hat{n}_i + U \sum_i \frac{\hat{n}_i \left(\hat{n}_i - 1\right)}{2} \tag{1.19}$$

In the additional disorder energy term, Δ corresponds to the strength of the secondary lattice. J and U are the tunnelling energy and on site interaction energy with respect to the primary lattice. Since the secondary lattice is weak compared to the primary, it does not produce a significant change in J and U. In the absence of interactions ($U = 0$) this Hamiltonian converges to Aubry-André (AA) or Harper model [20].

The disorder prepared by a quasi-periodic lattice is less effective as compared to a random disorder. In contrast to a random disorder where the system gets localized by any amount of disorder, in AA model the system localizes only after a certain strength of disorder. This localization threshold depends on the ratio of the two wavelengths, β. For a perfect irrational condition, $\beta = (\sqrt{5} - 1)/2$, the system localizes at $\Delta/J = 2$. However for values of β different from this condition, the value of localization threshold deviates from 2 towards higher value [21]. After the transition, all exponentially localized eigenstates have a single localization length, which is

$$\xi_{loc} \approx \frac{d}{ln(\Delta/2J)} \tag{1.20}$$

1.2.2 Experimental control parameters

The energy terms in equation 1.19 can be controlled in the experiments. In the first term, the tunneling energy J depends on the strength of the primary lattice. It is proportional to the overlap of the Wannier wave-function at two neighbouring sites. By approximating the Wannier functions to have Gaussian distribution the tunnelling energy can be obtain as a function of primary lattice strength [21]

$$\frac{J}{E_{rec}} \simeq 1.43 s_1^{0.98} exp\left(-2.07\sqrt{s_1}\right) \tag{1.21}$$

Here E_{rec} is the recoil energy, and s_1 is the strength of primary lattice in units of E_{rec}. Hence from this equation the tunneling energy can be calculated and tuned from the strength of primary lattice.

In the second energy term, Δ corresponds to the disorder strength. It depends on the perturbation on the primary lattice and hence can be tuned by the strength of secondary lattice. Its dependence on the secondary lattice can be calculated to be [21]

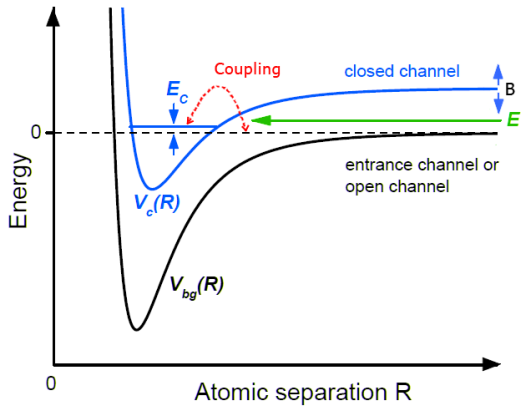

FIGURE 1.6: The potential for a two body collision. A Feshbach resonance takes place when the energy state of the free atoms E in the open channel V_{bg} resonantly couples with one of the molecular bound states in the closed channel V_c. The energy separation between the two states can be controlled by means of the magnetic field provided that the magnetic moments of the closed and open channel are different.

.

$$\frac{\Delta}{E_{rec}} = \left(s_2\beta^2/2\right) exp\left(-\beta^2/\sqrt{s_1}\right) \tag{1.22}$$

where s_2 is the strength of secondary lattice expressed in terms of recoil energy for the secondary lattice, E_{rec} is recoil energy for primary lattice.

Interactions

The third energy term depends on the on-site interaction energy which depends on the scattering length. In degenerate gases the dominant scattering is the s-wave scattering. The s-wave scattering length can often be tuned by magnetic fields and this phenomenon is called *Feshbach resonances* [22].

Feshbach resonances are a powerful tool to control the interaction between the atoms in ultracold atomic and molecular physics. A Feshbach resonance can be described using a potential plot of a two body atomic interaction. As illustrated in figure 1.6 we have two potential curves $V_{bg}(R)$ and $V_c(R)$. Here $V_{bg}(R)$ is the ground state potential and $V_c(R)$ is the excited state potential. For a large internuclear distance $V_{bg}(R)$ approaches to the energy of two free atoms. When the atoms collide with a small energy E, $V_{bg}(R)$ is the energetically open channel for the collision and is called the entrance channel. The other potential $V_c(R)$ is a closed channel but this may have a bound state close to the energy of two free atoms. A Feshbach resonance arises from the coupling between the free unbound atomic state to a molecular bound state. The closer is the molecular level with respect to the energy of the free atoms the stronger is the coupling. For the case in which the states corresponding to the two channels have different magnetic moments, the

energy of the closed channel can be tuned with respect to the open channel by applying and varying a magnetic field and therefore coupling between the free atoms state and a bound state can be changed. As a consequence of this, the scattering length modifies accordingly and can be tuned to a desired value. Mathematically, the expression for the dependence of the scattering length on the magnetic field in the vicinity of a Feshbach resonance can be written as

$$a(B) = a_{bg}\left(1 - \frac{\Delta_{FR}}{B - B_0}\right) \tag{1.23}$$

where B_0 is the resonance centre, Δ_{FR} is the resonance width and a_{bg} is the background scattering length, i.e. the scattering length far from resonance. The magnetic field at which scattering length crosses zero is called *zero-crossing magnetic field* and is given by $B_{zc} = B_0 + \Delta_{FR}$.

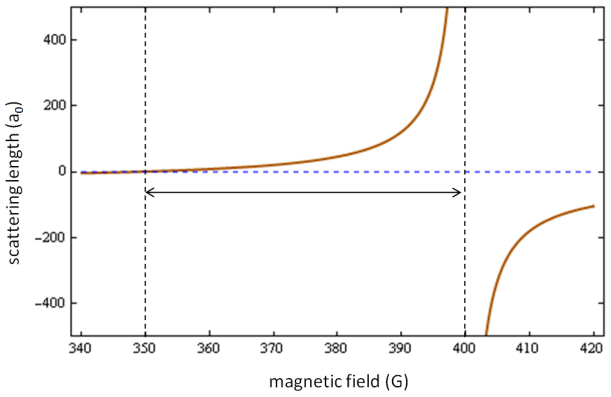

FIGURE 1.7: Scattering length vs magnetic field in the vicinity of ^{39}K Feshbach resonance at 400G. In the work reported in this thesis we exploit the scattering length in the range from 350G (zero crossing) to 400G.

In our experiment we realize a degenerate gas of Potassium-39 (^{39}K) atoms. This isotope offers a variety of Feshbach resonances [23]. We use a resonance centred at $B_0 \sim 400G$ (figure 1.7) for the ground state $|F = 1, m_F = 1\rangle$. This resonance has a width $\Delta_{FR} = 52G$ which gives us precise control over tunability of the scattering length from essentially zero up to a few hundreds of Bohr radii.

1.2.3 One-dimensional Bose gas

We start with a degenerate gas of ^{39}K containing nearly $N = 20000$ atoms with a scattering length at $a = 190a_0$.

We then prepare an array of one-dimensional quasi-condensates by confining the BEC in a two dimensional lattice as shown in figure 1.8. This lattice is adiabatically raised in 400ms using S-shaped ramps. They have two horizontal standing waves with a wavelength at 1064nm and a strength of $28E_r$ to suppress the tunnelling. Each of this 1D system has a radial confining frequency $\omega_r = 50$kHz and an axial confining frequency $\omega_z = 150$Hz. Each of this subsystem has on average 50 atoms. Along the axial direction a quasi-periodic lattice is ramped up in 300ms starting from 100ms after the 2D lattice started. It constitutes a primary lattice at $10E_r$ ($\lambda_1 = 1064$nm) and a secondary lattice at $0.5E_r$ ($\lambda_2 = 859$nm). This strength sets the tunnelling energy $J = h \times 150$Hz along the longitudinal direction.

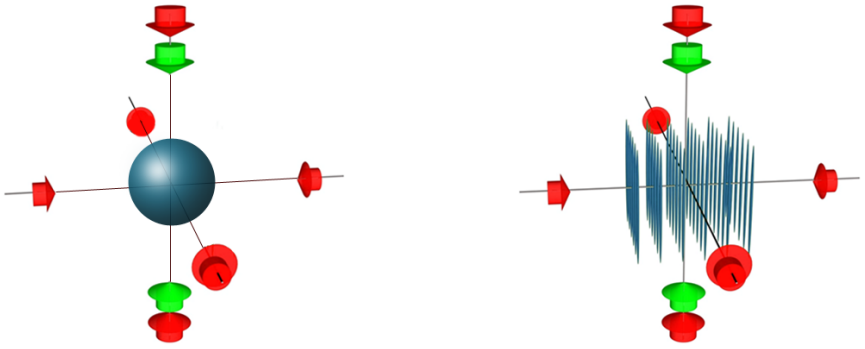

(A) (B)

FIGURE 1.8: Schematic diagram for experimental realization of a set of 1D quasi-condensates using two strong horizontal lattices and a quasi-periodic lattice superimposed along vertical direction.

In order to tune the interaction energy we tune the scattering length using a Feshbach resonance. The interaction energy is calculated from the scattering length as

$$U = \frac{\hbar^2}{m a_{1D}} \int \varphi(z)^4 dz \tag{1.24}$$

where $\varphi(z)$ is the Gaussian approximation of the Wannier function in a lattice site and a_{1D} is the 1D scattering length which depends on the 3D scattering length a as [24]

$$a_{1D} = \frac{a_r^2}{2a}\left(1 - \frac{1.03a}{a_r}\right) \tag{1.25}$$

Using Feshbach resonances the interaction energy U can be tuned within the range $(0.3 - 10)J$.

The atom number in each subsystem is calculated from the Thomas Fermi distribution of the density of the condensate in the optical dipole trap before ramping up the lattices.

After rearrangements the final number of atoms per subsystem can be derived as

$$N_{i,j} = \frac{5Nd^2}{2\pi R}\left[1 - \frac{(i^2+j^2)d^2}{R}\right] \tag{1.26}$$

where d is the lattice constant and R is the Thomas Fermi radius of the condensate. The average density in each subsystem is calculated using the formula

$$\bar{n}_{ij} = \frac{1}{5}\left(\frac{3N_{ij}m\omega_z}{\hbar}\right)^{2/3} a_{1D}^{1/3} \tag{1.27}$$

where ω_z is the axial trap frequency of the subsystem.

With this tuning range of interaction density in terms of mean atom number per site varies in the range 2 to 4.

1.2.4 Momentum distribution

We obtain the momentum distribution of this system from the absorption image after a time of flight of 16.5ms without interactions(figure 1.9). After this we integrate the image along the radial direction, getting an average momentum distribution.

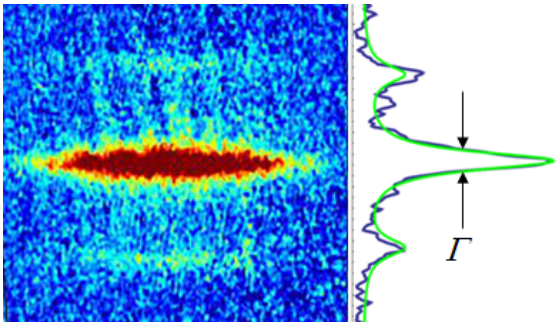

FIGURE 1.9: A time of flight image of the system shown in figure 1.8 and an averaged momentum distribution of all subsystems obtained by integrating this image along the horizontal.

In a regime of weak interactions and without disorder, we estimate the equilibrium temperature of this system from the width of the momentum distribution peak. After fitting a Lorentzian function to the momentum distribution peak, we calculate the thermal correlation length ξ_T from the half width at half maximum (HWHM) Γ using

$$\xi_T = \frac{0.74\hbar}{\Gamma} \tag{1.28}$$

which takes into account the finite width of the zero temperature. From ξ_T we calculate the temperature as

$$T = \frac{\hbar^2 n}{\xi_T d m^* k_B} \tag{1.29}$$

Here m^* is the effective mass of the atoms inside the primary lattice and k_B is the Boltzmann constant. From the above expressions we estimate the equilibrium temperature of our system to be $k_B T \simeq 3J$.

1.3 Dynamics

After preparation of the system, along the axial direction the set of 1D subsystems are confined by the harmonic potential created by lattice beams. We study the dynamics by switching off a magnetic field gradient that partially compensates gravity. This action shifts the center of harmonic potential by 4 μm. As a result of that the system starts to oscillate about the center of the new shifted confinement.

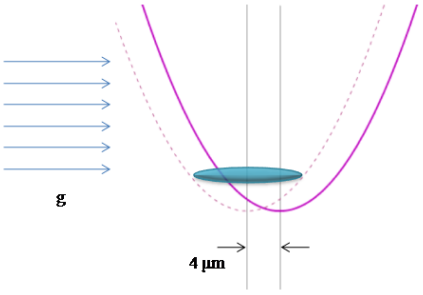

FIGURE 1.10: A cartoon showing the shift in harmonic potential leading to oscillation of the 1D subsystem.

This oscillation is perturbed because of the presence of a disordered lattice. To analyze the transport dynamics we trace the time evolution of momentum after the kick. For this we let the quasi-condensate gain momentum for some time t^* after the kick and then switch of all the fields to obtain a momentum space distribution. We restrict our analysis on the first Brillouin zone($|p| < h/\lambda_1$). In the momentum evolution we observe an asymmetry in the momentum distribution. This asymmetry reveals the mismatch between the peak momentum and the mean momentum, presumably due to an inhomogeneous damping throughout the axis. In absence of a detailed model of the inhomogeneous system, we decided to study the evolution of the peak momentum p_0. From the shift of the p_0 with respect to its equilibrium value we obtained the momentum Δp gained during time t^*.

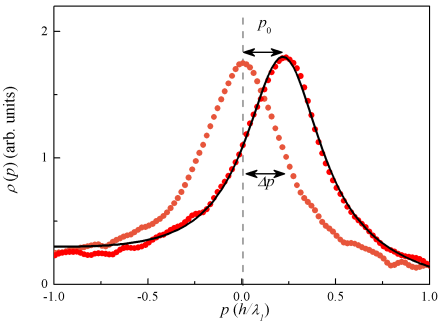

FIGURE 1.11: Momentum distribution without kick ($t^* = 0$) and with kick ($t^* = 0.8\mu s$) in a non-disordered lattice with interaction energy $U/J = 1.26$.

We increase this kick time starting from zero and obtain corresponding momenta gained. Then we plot these momenta vs kick time.

1.3.1 Momentum evolution analysis

We start with a clean system i.e. the 1D gas moves only in the primary lattice. In the case of only one lattice the atoms are expected to oscillate with a frequency

$$\omega^* = \omega_z \sqrt{m/m^*} \simeq 2\pi \times 90\text{Hz} \tag{1.30}$$

where m^* is the effective mass of the atoms in a lattice, which is $2.8m$ in our case. Figure 1.12 shows the time evolution of momentum at the interaction energy $U/J = 1.26$. We observe that the momentum undergoes damping from the beginning and deviates from the trail of ideal oscillation (dash-dotted line). The two curves fitted to the data are the momentum evolution for a damped oscillator model. In this model the evolution of peak momentum of particles in a lattice is given by

$$p_0(t) = \frac{m^*\omega^{*2} z_0}{\omega'} sin(\omega' t) e^{-\gamma' t} \tag{1.31}$$

where $\omega' = \sqrt{\omega^{*2} - \gamma^{*2}}$, $\gamma^* = \gamma m/m^*$ and γ is the damping rate. In the initial part of the evolution, the curve 1.31 is fitted with a damping rate $\gamma/2\pi = 135$Hz (continuous line). p_0 follows this behavior only up to a critical value, after which we observe a sudden increase of the damping, which leads to a rapid decrease of p_0 towards zero. In the later part of evolution we fit a damping rate $\gamma/2\pi = 600$Hz (dashed line).

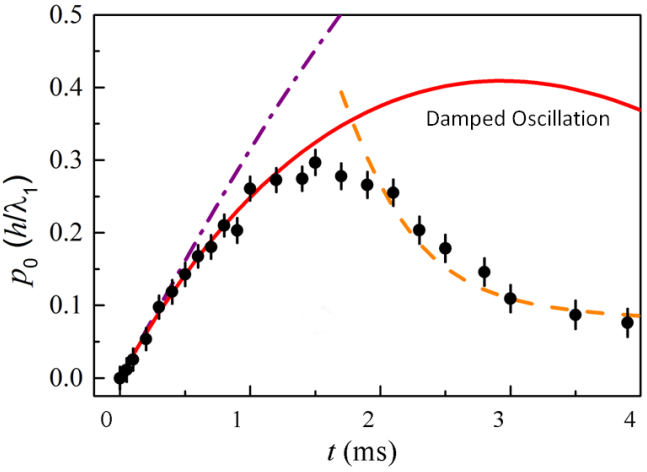

FIGURE 1.12: Time evolution of peak momentum in a non-disordered lattice with interaction energy $U/J = 1.26$ and density $n = 3.6$. The dot-dashed line is the momentum oscillation without damping. The experimental data points are fitted to the damped oscillation in the starting with $\gamma/2\pi = 135Hz$ and later with $\gamma/2\pi = 600Hz$

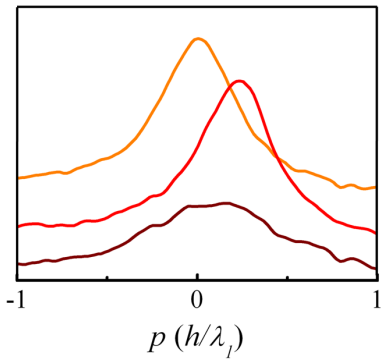

FIGURE 1.13: The broadening of the momentum peak after strong damping

In the momentum distribution analysis, the width of the distribution stays constant as the momentum increases up to a critical value with initial damping. When the damping increases suddenly the width of the momentum distribution increases indicating an instability (figure 1.13).

Theory comparison

There are no exact models for a damped oscillation over rapidly varying momentum and inhomogeneous density distribution. So we made a comparison of our observations with uniform superfluid decay models of interacting bosons [35–37]. In these models the initial damping and later instability is attributed to the nucleation of *quantum or thermal phase slips.*

The momentum dependent phase-slip nucleation is held responsible for damping in transport in various quantum systems like superfluid He in porous media [25–27], superconducting nanowires [28–32] or ultracold atoms [33–35, 41, 42]. In 1D systems this mechanism is stronger than in higher dimensions because of the larger quantum and thermal fluctuations. In a 1D system of bosons two different phase-slip regimes are present, depending on the temperature of the system [36]. This crossover temperature is calculated as

$$k_B T_0 = 0.21 \frac{2\sqrt{2}}{\pi} \sqrt{nJU} \sqrt{\frac{\pi}{2} - \frac{p\lambda_1}{2\hbar}} \tag{1.32}$$

here p is the momentum of the 1D system, n is the density of the system, J is the tunneling energy, U is the interaction energy and the term $\sqrt{nJU}$ is the Josephson energy. When $T < T_0$, the damping rate is due to quantum phase slips. The nucleation rate of quantum phase slips increases exponentially as

$$\Gamma_Q \propto exp\left[-7.1\sqrt{\frac{nJ}{U}}\left(\frac{\pi}{2} - \frac{p\lambda_1}{2\hbar}\right)^{\frac{5}{2}}\right] \tag{1.33}$$

If $T > T_0$ the dissipation is due to thermally activated phase slips whose nucleation rate is

$$\Gamma_T \propto exp\left[-\frac{4nJ}{3k_B T}\left(\frac{\pi}{2} - \frac{p\lambda_1}{2\hbar}\right)^{3}\right] \tag{1.34}$$

In both the expressions it is clear that as p starts to increase from zero there is a slow increase in the phase-slip nucleation rate. But as $p \longrightarrow h/2\lambda_1$ the quantity $\left(\frac{\pi}{2} - \frac{p\lambda_1}{2\hbar}\right) \longrightarrow 0$ and, because of the high power over this factor, the increase in nucleation rate is abrupt leading to an instability.

The phase slip nucleation rate in both regimes depends on the density of the systems, n. For a one dimensional system having a low density, because of the prefactor in the exponent, the damping may be high enough to suppress the momentum increase before it could reach the value of instability. This effect was observed in a previous transport experiment in 1D at a density $n \sim 1$ [41], where unlike in three dimensional system [42] a very high damping was observed. In our 1D system the average density varies as $n \sim 2 - 4$ depending on the interaction energy, which is relatively higher. Moreover in each system the density distribution is non uniform. The central part which has larger density suffers less initial damping and allows the system to reach the instability. The tails have lower density components and suffer more damping leading to an asymmetry in the momentum distribution (figure 1.11).

From equation 1.32, the crossover temperature for our system for $p \sim 0$ is found to be of the order of Josephson energy which is in the range of $\sqrt{nJU} = (1 - 4)J$. The

temperature of our system ($k_BT = 3J$) is in the range of crossover temperature. From equations 1.33 and 1.34 it is clear that the quantum phase slips increase with the interaction energy. To find out which phase slip mechanism is dominant in our system we looked at transport dynamics under different interaction energies.

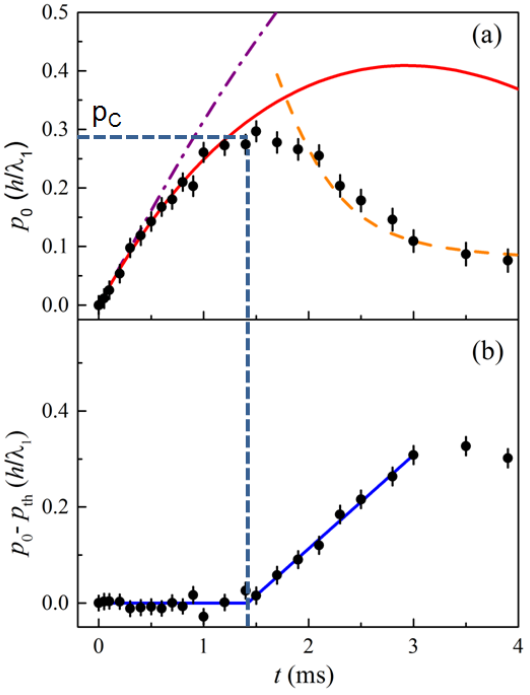

FIGURE 1.14: The evolution of the momentum (a) and the difference between experimental data and initial damping fit (b) to estimate the critical momentum p_c.

Critical momentum

In order to study the effect of interaction on the evolution of momentum, we find out the maximum momentum which can be given to the system before it enters the regime of instability. This critical momentum p_c separates the initial weakly dissipative regime from the strongly dissipative regime. We subtract the data points from the initial oscillation curve and make a peace wise linear fit to find out the momentum from which it starts to deviate from weak dissipation as shown in figure 1.14.

The effect of interaction on the transport dynamics is reflected on the critical momentum. Therefore we investigate the critical momentum under different interaction strengths.

1.4 Clean system

In our analysis with non-disordered lattices figure 1.15 shows the dependence of critical momentum on the interaction energy. The critical momentum decreases linearly with increasing interaction energy and after a critical value of interaction U_c it becomes constant close to zero. This critical value is found by piece wise linear fit as shown in figure. Since the system stops to move ($p_c \sim 0$) after this interaction we mark this as fluid to Mott insulator transition. A similar reasoning was used to mark the Mott insulator transition point for the transport in 3D systems [42].

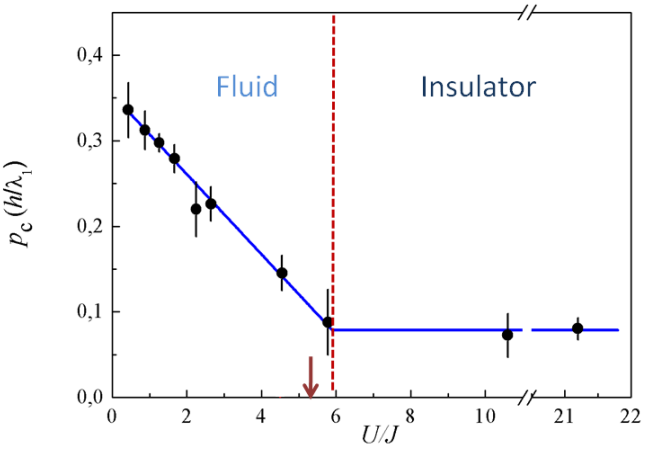

FIGURE 1.15: The dependence of critical momentum on the interaction energy U for a non-disordered lattice. The arrow marks the theoretically predicted critical interaction energy for the transition to Mott insulator for $n = 2$

The value of U_c/J obtained from fit is 5.9 and is comparable with the theoretically predicted critical interaction ($U_c/J = 5.34$) for an occupation $n = 2$ [39]. This observation confirms that the vanishing of critical momentum can be employed to obtain the fluid-insulator transition point. Thus in the next section we will use the same methodology to find the superfluid-Bose glass transition point. Even in the insulating regime we see a non-zero value of p_c. A possible interpretation for this is that the system does not completely stop due to the incommensurate fraction (inhomogeneous density), which does not localize.

For the dependence of p_c with U we compared our data with complete phase-slip nucleation rate expression. For quantum phase-slips the nucleation rate is [37]

$$\Gamma_Q = B_Q L(U)\sqrt{nJU}\sqrt{\frac{\pi}{2} - \frac{p\lambda_1}{2\hbar}}\sqrt{\frac{7.1(\pi/2 - p\lambda_1/2\hbar)^{5/2}}{2\pi\sqrt{U/nJ}}}exp\left[-7.1\sqrt{\frac{nJ}{U}}\left(\frac{\pi}{2} - \frac{p\lambda_1}{2\hbar}\right)^{\frac{5}{2}}\right] \tag{1.35}$$

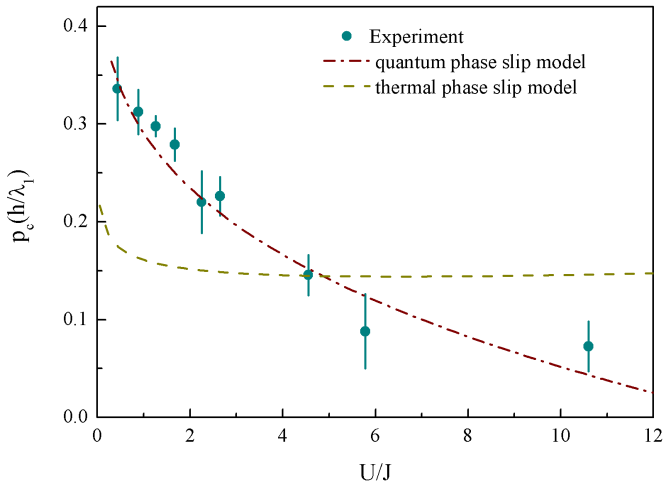

FIGURE 1.16: A plot showing critical momentum versus interaction energy. The dots are experimental data points, dashed-dotted curve is theoretical curve $p_c(U)$ for the quantum phase slip model and the dashed curve is for the thermal phase slip model.

and for thermal phase-slips the nucleation rate is [36]

$$\Gamma_T = B_T cos(p\lambda_1/2\hbar)\sqrt{nJU} exp\left[-\frac{4nJ}{3k_BT}\left(\frac{\pi}{2} - \frac{p\lambda_1}{2\hbar}\right)^3\right] \tag{1.36}$$

Here $L(U)$ is the average Thomas-Fermi length of the subsystems, which scales with the interaction energy as $U^{1/3}$; B_Q and B_T are phenomenological constants.

To obtain the $p_c(U)$ from the above expressions we set the value of $\gamma \simeq 1$kHz i.e. to the value at which we experimentally observe instability and obtain p_c. Then we adjust the constants B_Q and B_T in order to reproduce the p_c at $U/J = 4.5$.

Figure 1.16 shows the experimental data and theoretical $p_c(U)$ in the two regimes. It is clear that the curve for quantum phase slip follows along the data points, where as for thermal phase slip mode p_c shows a weak dependence on U. This indicates that in our case the damping is introduced predominantly by quantum phase slips,

For the approximate value of γ which is set to 1kHz to produce the theoretical $p_c(U)$, it was being confirmed that the choice of γ changes only the offset of the curve without changing the shape.

Although we observe the dependence of initial damping rate γ on U, as shown in figure 1.17, a similar theoretical treatment is not possible for $\gamma(U)$. The damping rate $\gamma(U)$ ($\sim \Gamma_Q/p$) has a strong dependence on the momentum due to the exponential term. Hence the choice of p to theoretically reproduce $\gamma(U)$ is very crucial and difficult to fix for a rapidly changing momentum.

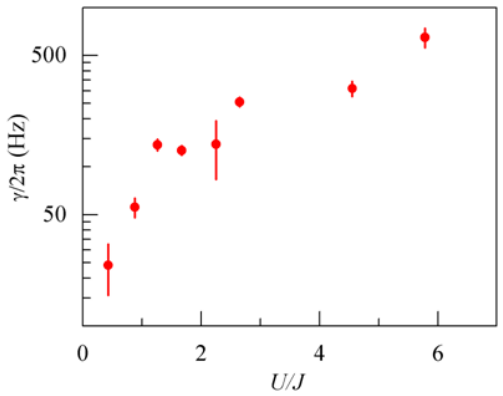

FIGURE 1.17: The dependence of initial damping rate on the interaction energy.

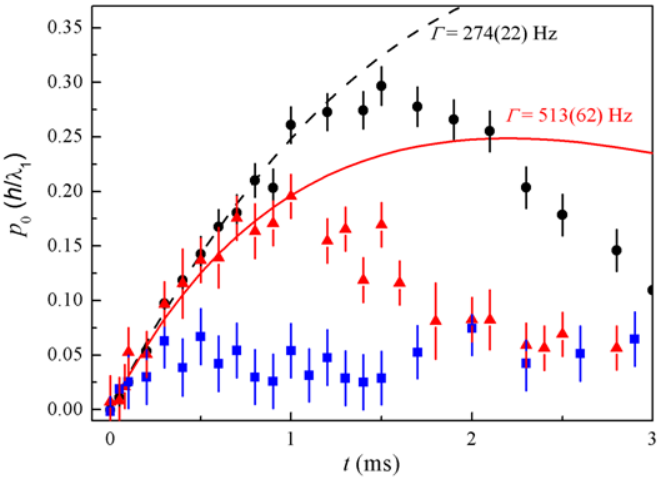

FIGURE 1.18: Time evolution of momentum at different disorder strengths $\Delta/J = 0$(dots), $\Delta/J = 3.6$ (triangles), $\Delta/J = 10$ (squares) and a fixed interaction energy $U/J = 1.26$.

1.5 Disordered system

In order to investigate the effect of disorder we fix the interaction energy to particular value. We then vary the strength of disorder and see the effect on the critical momentum. Figure 1.18 shows the evolution of momentum under different disorder strengths Δ for an interaction energy set to $U = 1.26J$. The disorder increases the initial damping rate and anticipates the instability. This is due to fact that the disorder tends to decrease the effecting tunneling energy and hence increases the phase slip nucleation rate.

As in the case of interaction energy also here we extract the critical moment and plot it against the disorder strength. We see that p_c decreases linearly and then after a critical value of disorder strength Δ_c it becomes constant to a small value similar to that observed in the Mott insulator regime (figure 1.19). From the piece wise linear fit we find that the Δ_c is of the same order of the total interaction energy per particle nU.

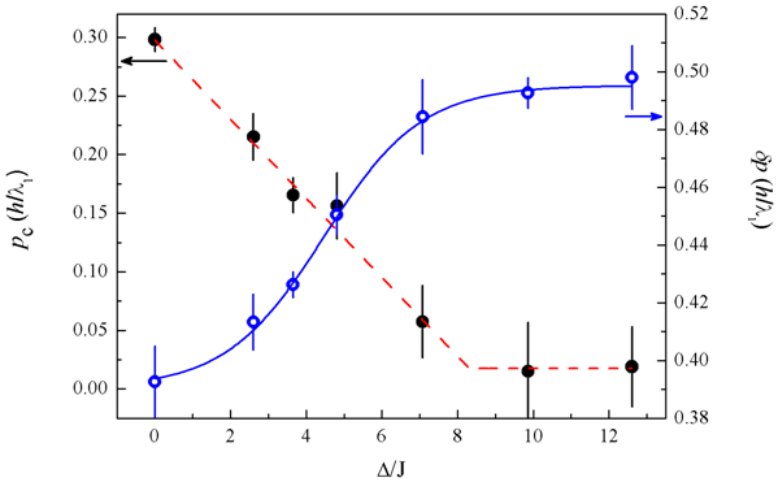

FIGURE 1.19: The critical momentum p_c (dots) and rms width of momentum distribution at equilibrium δp (open circles) versus disorder strength Δ/J at an interaction energy $U/J = 1.26$. The piece wise linear fit (dashed) is to find Δ_c and solid line is a sigmoidal fit of δp

Therefore this is expected to be the regime where weakly interacting Bose glass should appear where disorder has overcome the delocalization effects due to interaction[43, 44].

Figure 1.19 also shows the rms width δp of the momentum peak δp at the equilibrium i.e at $t^* = 0$, versus the disorder. This width is inversely proportional to the correlation length ξ and start to increase before the critical momentum reaches its minimum. This implies that decrease of p_c indicates the onset of a strongly insulating phase which has a correlation length $\xi \simeq d$.

In order to find the crossover separating the fluid regime from the insulating regime in the phase diagram we repeated the measurements with different interaction strengths. Then we collected the critical disorder strengths Δ_c to enter the insulator for different U. Figure 1.20 shows the evolution of Δ_c with U. As expected, at higher interaction energy the disorder is relatively less important and we need stronger disorder to localize the system.

Theoretical models for 1D interacting bosons in disorder should show the transition to an insulator when the disorder strength overcomes the total interaction energy per particle. The critical disorder to enter the insulating phase should scale as [44]

$$\frac{\Delta_c}{J} = A\left(\frac{E_{int}}{J}\right)^{\alpha} \tag{1.37}$$

where $E_{int} \simeq nU$ is the total interaction energy per particle and the constants A and α are close to unity. This model has been derived for weakly interacting systems and for a true disorder.

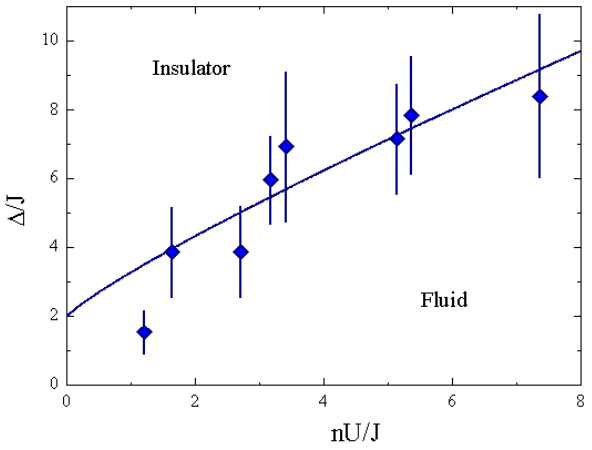

FIGURE 1.20: Critical disorder Δ_c/U to enter the insulating phase versus total interaction energy nU/J. The experimental data(dots) are fitted with the curve 1.38. Large error bars are due to error on calibration of disorder (20%).

In the absence of an exact analytical model for a quasi-periodic disorder we tried to make a comparison of our data with this model. Therefore we fitted a modified law

$$\frac{\Delta_c - 2J}{J} = A\left(\frac{E_{int}}{J}\right)^{\alpha} \tag{1.38}$$

which takes into account the fact that a system of non-interacting particles in a quasi-periodic lattice shows a metal-insulator transition at $\Delta/J \simeq 2$. By fitting this curve to the data we obtained the coefficients $A = 1.3 \pm 0.04$ and $\alpha = 0.86 \pm 0.0022$. The exponent is in good agreement with the theory [44] where as larger coefficient A could be become of quasi-periodic disorder which is less effecting that true disorder.

1.6 Conclusions

In the work reported in this chapter, we shed light on the long-standing problem of the interplay of disorder and interaction on the phases of a quantum gas. Particularly in 1D, there has been a large theoretical work done in the last decades. The corresponding experimental realization of the predicted phases and their crossover lines have been an open problem.

In our experiment, this problem was addressed by analyzing the transport dynamics of a gas in disorder. The strength of disorder and interaction were tuned, and their combined effect on the superfluidity of a 1D Bose gas of ^{39}K was studied. We started our investigation with the analysis of dynamics of a 1D gas in a clean lattice. The mechanism of phase slip nucleation, which leads to dissipation in superconducting nanowires and superfluid He, is held responsible for the damping in the 1D transport reported

here. Because of relatively larger density in our experiment as compared to previous experiments in 1D [41], our system suffered less damping and we could demonstrate the first observation of dynamic instability in a one dimensional system which was observed only in 3D [42]. This observation emphasizes the importance of density in the transport in 1D systems.

To study the effect of disorder and interaction on the transport, the maximum momentum attainable before the instability, called critical momentum, was used as an observable to distinguish between a fluid and an insulating phase. The disorder tends to increase the phase slip nucleation leading to the onset of Bose glass phase. As predicted theoretically the interaction decreases the effect of disorder. From the vanishing of the critical momentum, we obtained a crossover line in disorder versus interaction plane, which separates the superfluid phase from the Bose glass phase. This result is found to be consistent with relevant theoretical models.

In this method, since we used the shift in momentum peak as a measure of momentum gained by the system, due to the broadening of the momentum peak at higher interactions, the accuracy of the measurements reduces, and hence this work was done in the regime of weak interactions. However, it will be interesting to explore similar crossovers in the strongly interacting systems with other methods. In the near future we will like to see the effect of temperature on the crossover, and attribute the results to finite temperature phase transitions [46].

Bibliography

[1] M. Girardeau, *Relationship between Systems of Impenetrable Bosons and Fermions in One Dimension*, J. Math. Phys. 1, 516 (1960).

[2] E. H. Lieb, W. Liniger, *Exact Analysis of an Interacting Bose Gas. The General Solution and the Ground State*, Phys. Rev. 130, 1605 (1963).

[3] B. Paredes, A. Widera, V. Murg, O. Mandel, S. Fölling, I. Cirac, G. V. Shlyapnikov, T. W. Hänsch and I. Bloch, *TonksGirardeau gas of ultracold atoms in an optical lattice*, Nature 429, 277 (2004).

[4] C. J. Pethick, H. Smith, *Bose-Einstein condensation in Dilute Gases*, Cambridge University Press (2001).

[5] V. S. Letokhov, *Narrowing of the Doppler Width in a Standing Wave*, JETP Letters 7, 272 (1968).

[6] C. Salomon, J. Dalibard, A. Aspect, H. Metcalf, and C. Cohen-Tannoudji, *Channeling atoms in a laser standing wave*, Phys. Rev. Lett. 59, 1659 (1987).

[7] D. Jaksch, C. Bruder, J. I. Cirac, C. W. Gardiner, and P. Zoller, *Cold Bosonic Atoms in Optical Lattices*, Phys. Rev. Lett. 81, 3108-3111 (1998).

[8] O. Morsch and M. Oberthaler, *Dynamics of Bose-Einstein condensates in optical lattices*, Rev. Mod. Phys. 78, 179–215 (2006).

[9] P. W. Anderson, *Absence of Diffusion in Certain Random Lattices*, Phys. Rev. 109, 1492–1505 (1958).

[10] J. Billy, V. Josse, Z. Zuo, A. Bernard, B. Hambrecht, P. Lugan, D. Clément, L. Sanchez-Palencia, P. Bouyer and A. Aspect, *Direct observation of Anderson localization of matter waves in a controlled disorder*, Nature 453, 891-894 (2008).

[11] G. Roati, C. D'Errico, L. Fallani, M. Fattori, C. Fort, M. Zaccanti, G. Modugno, M. Modugno and M. Inguscio, *Anderson localization of a non-interacting Bose–Einstein condensate*, Nature 453, 895-898 (2008).

[12] Giamarchi T. and Schulz H. J., *Anderson localization and interactions in one-dimensional metals*, Phys. Rev. B 37, 325-340 (1988).

[13] S. Rapsch, U. Schollwöck and W. Zwerger, *Density matrix renormalization group for disordered bosons in one dimension*, Europhys. Lett. 46, 559 (1999).

[14] Fisher D. S. and Fisher M. P. A., *Onset of superfluidity in random media*, Phys. Rev. Lett. 61, 1847-1850 (1988).

[15] Scalettar R. T., Batrouni G. G. and Zimanyi G. T., *Localization in interacting, disordered, Bose systems*, Phys. Rev. Lett. 66, 3144-3147 (1991).

[16] B. Deissler, M. Zaccanti, G. Roati, C. D'Errico, M. Fattori, M. Modugno, G. Modugno and M. Inguscio, *Deolcalization of a disordered bosonic system by repulsive interaction*, Nature Physics 6, 354 - 358 (2010).

[17] Steven R. White *Density matrix formulation for quantum renormalization groups* Phys. Rev. Lett. 69, 2863-2866 (1992).

[18] Karen Hallberg *New Trends in Density Matrix Renormalization* Adv.Phys.55:477-526 (2006).

[19] J. W. Goodman, *Speckle Phenomena in Optics: Theory and Applications*, Roberts and Company Publishers, (2007).

[20] Aubry S and André G, Ann. Isr. Phys. Soc. 3, 33 (1980)

[21] M. Modugno, *Exponential localization in one-dimensional quasi-periodic optical lattice*, New J. Phys. 11, 033023 (2009)

[22] C. Chin, R. Grimm, P. Julienne, E. Tiesinga, *Feshbach resonances in ultracold gases*, Rev. Mod. Phys. 82, 1225-1286 (2010)

[23] C. D'Errico, M. Zaccanti, M. Fattori, G. Roati, M. Inguscio, G. Modugno and A. Simoni, *Feshbach resonances in ultracold* ^{39}K, New J. Phys. 9, 223 (2007).

[24] V. Dunjko, V. Lorent, and M. Olshanii, *Bosons in Cigar-Shaped Traps: Thomas-Fermi Regime, Tonks-Girardeau Regime, and In Between*, Phys. Rev. Lett. 86, 5413 (2001).

[25] R. Toda, M. Hieda, T. Matsushita, N. Wada, J. Taniguchi, H. Ikegami, S. Inagaki and Y. Fukushima, *Superfluidity of* ^{4}*He in One and Three Dimensions Realized in Nanopores*, Phys. Rev. Lett. 99, 255301 (2007).

[26] J. Taniguchi, R. Fujii and M. Suzuki, *Superfluidity and BEC of liquid* ^{4}*He confined in a nanometer-size channel*, Phys. Rev. B 84, 134511 (2011).

[27] T. Eggel, M. A. Cazalilla and M. Oshikawa, *Dynamical Theory of Superfluidity in One Dimension* Phys. Rev. Lett. 107, 275302 (2011).

[28] A. Bezryadin, C. N. Lau and M. Tinkham, *Quantum suppression of superconductivity in ultrathin nanowires*, Nature 404, 971-974 (2000).

[29] K.Yu. Arutyunov, D.S. Golubev and A.D. Zaikin, *Superconductivity in one dimension*, Phys. Rep. 464, 1 (2008).

[30] S. Khlebnikov and L. P. Pryadko, *Quantum Phase Slips in the Presence of Finite-Range Disorder*, Phys. Rev. Lett. 95, 107007 (2005).

[31] A. T. Bollinger, R. C. Dinsmore, III, A. Rogachev and A. Bezryadin, *Determination of the Superconductor-Insulator Phase Diagram for One-Dimensional Wires*, Phys. Rev. Lett. 101, 227003 (2008).

[32] O. V. Astafiev, L. B. Ioffe, S. Kafanov, Yu. A. Pashkin, K. Yu. Arutyunov, D. Shahar, O. Cohen and J. S. Tsai, *Coherent quantum phase slip*, Nature 484, 355–358 (2012).

[33] A. Smerzi, A. Trombettoni, P. G. Kevrekidis, and A. R. Bishop, *Dynamical Superfluid-Insulator Transition in a Chain of Weakly Coupled Bose-Einstein Condensates*, Phys. Rev. Lett. 89, 170402 (2002).

[34] L. Fallani, L. De Sarlo, J. E. Lye, M. Modugno, R. Saers, C. Fort, and M. Inguscio, *Observation of Dynamical Instability for a Bose-Einstein Condensate in a Moving 1D Optical Lattice*, Phys. Rev. Lett. 93, 140406 (2004).

[35] E. Altman, A. Polkovnikov, E. Demler, B. I. Halperin, and M. D. Lukin, *Superfluid-Insulator Transition in a moving System of Interacting Bosons*, Phys. Rev. Lett. 95, 020402 (2005).

[36] A. Polkovnikov, E. Altman, E. Demler, B. Halperin, and M. D. Lukin, *Decay of superfluid currents in a moving system of strongly interacting bosons*, Phys. Rev. A 71, 063613 (2005).

[37] I. Danshita and A. Polkovnikov, *Quantum phase slips in one-dimensional superfluids in a periodic potential*, Phys. Rev. A 85, 023638 (2012).

[38] I. Danshita, *Universal Damping Behavior of Dipole Oscillations of One-Dimensional Ultracold Gases Induced by Quantum Phase Slips*, Phys. Rev. Lett. 111, 025303 (2013).

[39] I. Danshita and A. Polkovnikov, *Superfluid-to-Mott-insulator transition in the one-dimensional Bose-Hubbard model for arbitrary integer filling factors*, Phys. Rev. A 84, 063637 (2011).

[40] J Schachenmayer, G Pupillo and A J Daley, *Time-dependent currents of one-dimensional bosons in an optical lattice*, New J. Phys. 12, 025014 (2010).

[41] C. D. Fertig, K. M. O′Hara, J. H. Huckans, S. L. Rolston, W. D. Phillips, and J. V. Porto, *Strongly Inhibited Transport of a Degenerate 1D Bose Gas in a Lattice*, Phys. Rev. Lett. 94, 120403 (2005).

[42] Jongchul Mun, Patrick Medley, Gretchen K. Campbell, Luis G. Marcassa, David E. Pritchard, and Wolfgang Ketterle, *Phase Diagram for a Bose-Einstein Condensate Moving in an Optical Lattice*, Phys. Rev. Lett. 99, 150604 (2007).

[43] P. Lugan, D. Clément, P. Bouyer, A. Aspect, M. Lewenstein, and L. Sanchez-Palencia, *Ultracold Bose Gases in 1D Disorder: From Lifshits Glass to Bose-Einstein Condensate*, Phys. Rev. Lett. 98, 170403 (2007).

[44] Luca Fontanesi, Michiel Wouters, and Vincenzo Savona, *Superfluid to Bose-Glass Transition in a 1D Weakly Interacting Bose Gas*, Phys. Rev. Lett. 103, 030403 (2009).

[45] M. Pasienski, D. McKay, M. White and B. DeMarco, *A disordered insulator in an optical lattice*, Nature Physics 6, 677-680 (2010).

[46] I. L. Aleiner, B. L. Altshuler and G. V. Shlyapnikov, *A finite-temperature phase transition for disordered weakly interacting bosons in one dimension*, Nature Physics 6, 900–904 (2010).

Chapter 2

Towards ultracold mixture and molecules

Interaction among particle plays a critical role in determining the physics of a many body quantum system. In the previous chapter we saw how interaction among bosons screens the effect of disorder. Nevertheless interaction can be of different kinds. In the case of neutral atoms the interaction present is a contact (hard sphere) type. A major step forward in the physics of ultracold gases could be to have long range interactions. In this direction the heteronuclear diatomic molecules realized recently [6, 7] are promising. These molecules possess dipolar interactions which are long range, anisotropic and tunable using external electric fields. The ability to control these interactions not only enhances the condensed matter simulations but it can allow us to engineer quantum information processing by using dipolar molecules as qubits. The production of molecules from binding ultracold atoms requires a double Mott insulator as a prerequisite. As will be discussed in this chapter, a double Mott insulator can be achieved through various approaches and a most optimum strategy will need to be followed. This task, because of the complexity in manipulating a two species mixture in lattices, requires a detailed analysis of the mixture's response towards the manipulation of trapping geometries present in the laboratory setup.

2.1 Long range dipolar interaction

A long range dipolar interaction outperforms the contact interaction due to that fact that it can act from a distance larger than the scattering length of the particles. Since this is anisotropic it can be tuned by aligning the dipoles using external electric or magnetic fields.

2.1.1 Dipolar systems

In the context of ultracold gases the dipolar systems employed are *magnetic dipoles* or *or electric dipoles*. The dipolar interaction strength of a system of dipoles depends on the dipole moment. In magnetic dipolar systems realized till now[1–5], the dipole moment ranges in the interval $d \sim 1 - 10\mu_B$, where μ_B is the Bohr magneton. However this dipolar strength is weak at a typical distance between the sites of the optical lattice, which limits the usability or magnetic dipoles to study lattice physics.

The electric dipolar gases are realized by binding two different alkali atoms, which creates inhomogeneous charge distribution over the axis leading to a permanent electric dipole on the molecule. The ultracold diatomic gases realized recently[6, 7] possess a dipole moment $d \sim 1Debye$ which provides an interaction strength four orders of magnitude larger than magnetic dipoles. Therefore electric dipoles are far more advantageous.

For two dipolar molecules with electric dipole strength d in their ground state $J = 0$, the interaction potential is given by

$$U(r) = -\frac{d}{6Br^6} \tag{2.1}$$

This interaction is isotropic in nature. To introduce anisotropic interaction we have to apply an external electric field ε. The interaction potential modifies to

$$U(r) = \frac{d(\varepsilon)^2}{r^3}\left(1 - 3cos^2\theta\right) - \frac{d}{6Br^6} \tag{2.2}$$

here $d(\varepsilon)$ is the dipole moment induced by external electric field and θ is the angle between the electric field and intermolecular distance. From the above equation it is clear that using the orientation of electric field the interaction can be tuned from repulsive to attractive.

(A) Two polar molecules in their ground state.

(B) Two polar molecules aligned along the external electric field.

FIGURE 2.1: Interaction among polar molecules.

2.1.2 1D Bose gas of polar molecules

If we have a one-dimensional system of polar molecules in a lattice, then, because of long range interactions not only on site interaction, but nearest neighbor or next to nearest neighbor interaction also becomes significant.

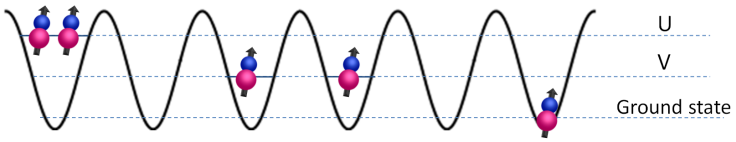

FIGURE 2.2: Interaction energies of polar molecules inside a one dimensional lattice. U is the on site interaction energy and V is the inter site interaction energy.

Taking into consideration the nearest neighbor interaction the Bose Hubbard Hamiltonian of polar molecules in a lattice is written as

$$\hat{H}_{BH} = -J \sum_{<i,j>} \hat{a}_i^\dagger \hat{a}_j + U \sum_i \frac{\hat{n}_i \left(\hat{n}_i - 1\right)}{2} + V \sum_i n_i n_{i+1} \tag{2.3}$$

here J is the tunnelling energy, $\hat{a}_i^\dagger$ and $\hat{a}_i$ are boson annihilation and creation operators, U is the on site interaction energy and V is the intersite interaction energy.

The intersite interaction energy can be tuned by changing the alignment of molecular dipoles using an external electric field. This feature gives rise to a variety of insulating phases even in a non-disordered lattice.

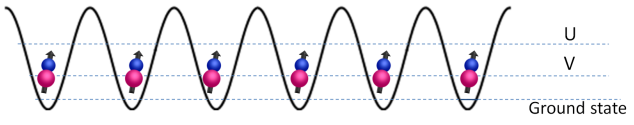

FIGURE 2.3: Mott insulator phase of polar molecules in a lattice with an occupancy $n = 1$ when $V < U$.

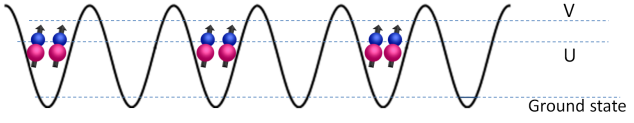

FIGURE 2.4: Density wave phase of polar molecules in a lattice with an occupancy $n = 1$ when $V > U$.

Consider the case of polar molecule in a lattice with an occupancy of one particle per site. For a significant on site interaction energy U and small inter site interaction energy V we see a Mott insulator (2.3). As the inter site interaction is increased, when their inter site repulsion overcomes the on site interaction energy, molecules occupy the sites in pairs leaving an adjacent site empty (2.4). This phase is called density wave (DW) phase. In between the MI and DW, another phase called Haldane insulator (HI) [9] appears, which has same occupancy as Mott insulator be different excitation properties.

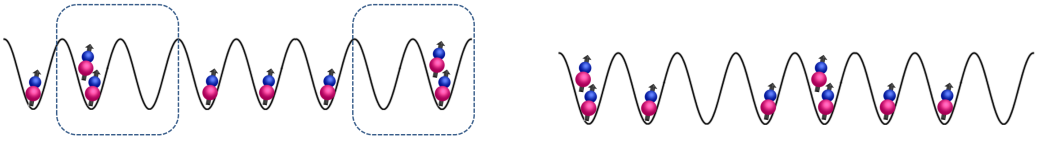

(A) In a Mott insulator during the excitation the particle-hole parity is maintained.

(B) In a Haldane insulator during the excitation the particle-hole parity is lost.

FIGURE 2.5: Excitation properties of a Mott insulator and a Haldane insulator.

During the excitation, in a Mott insulator when a particle and a hole is created, their parity is maintained i.e. a particle is excited to the next neighbour sites only. But in the case of HI, where due to the inter site interactions the coupling extends ideally to any two sites, the particle hole parity is lost i.e. a particle can be excited to any other site (2.5).

Figure 2.6 shows the predicted phases in a clean lattice [8]. Here, besides a superfluid (SF) and Mott insulator (MI), because of internuclear interaction, also Haldane insulator and density wave appears.

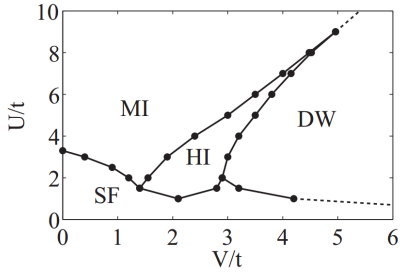

FIGURE 2.6: The phases of 1D gas of polar molecules in a lattice under different on-site and itersite interaction strengths as predicted in [8].

In the presence of disorder the physics becomes more complex. In a case where the onsite interaction energy is $U/J = 5$, on a $\Delta - V$ plane, the random disorder induces a Bose glass phase which beats out the other phases (figure 2.7a). For the same interaction

energy when the disorder is quasi-periodic, with increasing disorder strength system goes through incommensurate density wave (localized and gapped) [10, 11] followed by a Bose glass phase (localized and gapless) (figure 2.7b).

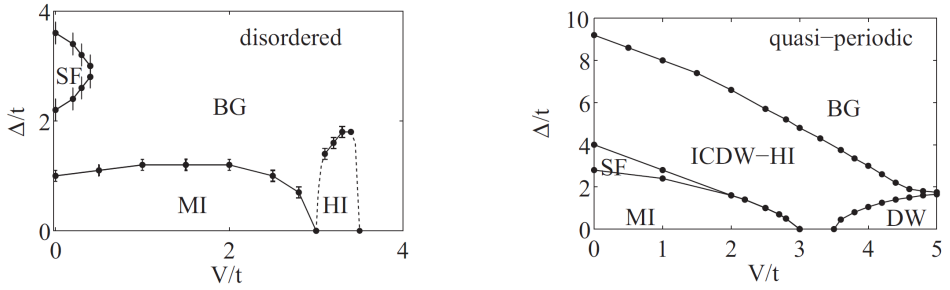

(A) The predicted phases of polar molecules in a random disorder.

(B) The predicted phases of polar molecules in a quasi-periodic disorder.

FIGURE 2.7: The $\Delta - V$ phase diagram for polar molecules for two kinds of disorder at a fixed interaction energy $U/t = 5$ [8].

2.1.3 $^{39}K^{87}Rb$ system

In our BEC setup we start the cooling cycle from a mixture of ^{39}K and ^{87}Rb. The whole cooling process is explained in section 2.3.1. Therefore we have been progressing towards binding a degenerate mixture of K and Rb to achieve a gas of *bosonic polar molecules*. These molecules have a permanent electric dipole moment 1.44 Debye ($0.30ea_0$) [12]. $^{39}K^{87}Rb$ is chemically reactive and being bosonic in nature their collisions and hence decay is unavoidable. However by confining them in a 1D lattice and aligning their polarity perpendicular to the lattice it is possible to avoid collisions study physics of highly correlated bosonic molecules.

2.2 Production scheme

The production of molecules will follow two steps. In the first step K and Rb atoms will be loosely bound using a interspecies magnetic Feshbach resonance. In the second step these Feshbach molecules will be transferred to the deeply bound ground state molecules using spectroscopy.

However Feshbach molecules which we will make being bosonic will suffer collisions from single atoms and will decay. To avoid this, before making Feshbach molecules we will prepare our system to a *double Mott insulator* with a pair of K and Rb per site as will be explained in detail in section 2.3.

2.2.1 $^{39}K^{87}Rb$ Feshbach resonance

The ground state K and Rb atoms offer many interspecies Feshbach resonances[13]. Out of them we will us a resonance at 318G which has a width of 7.6G and a background scattering length of $34a_0$ (figure 2.8).

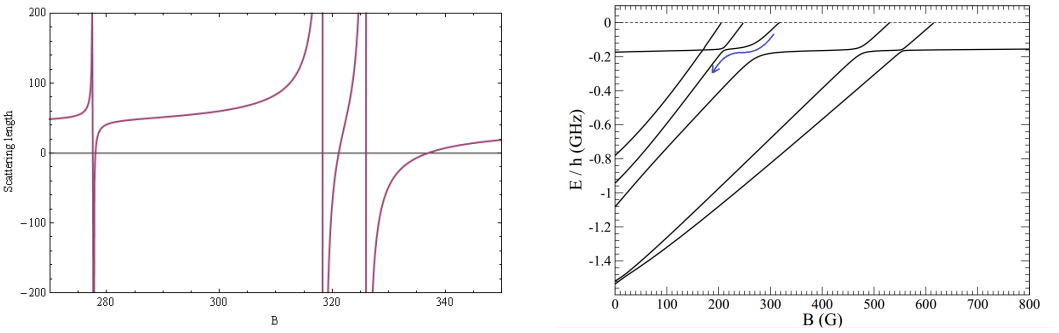

(A) (B)

FIGURE 2.8: The interspecies Feshbach resonances (left) and $^{39}K^{87}Rb$ molecular levels coupled to atoms (right) setting the energy of free particles at zero.

In order to enter a bound state we will adiabatically sweep the magnetic field from 300G as shown in figure 2.8b.

2.2.2 Ground state transfer

Figure 2.9 show the KRb molecular potential structure[5]. After the Feshbach association, molecules are predominantly triplet ($a^3\Sigma^+$). They are weakly bound with a larger internuclear distance and hence do not possess strong enough dipole moment. Therefore we will spectroscopically transfer them to singlet ($X^1\Sigma^+$) deeply bound ground state. For this we will electronically excite the molecules to an excited state and then dump them to the ground state using two coherent laser pulses.

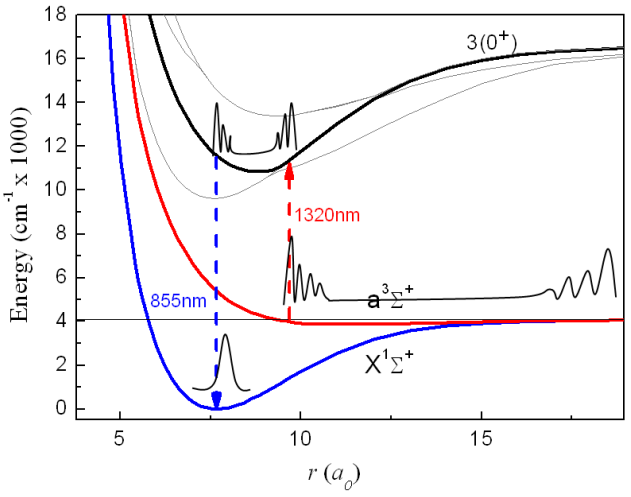

FIGURE 2.9: KRb molecular potentials.

The excited state has a radiative life time of the order of 15 nanoseconds. This implies that we cannot populate the excited state as it is usually done in the standard Raman technique. We will indeed carry out a *Stimulated Raman Adiabatic Passage*, which exploits the fact that the three level system is kept in a dark state, i.e. a superposition of the initial and final state with no contribution from the intermediate state[15]. Initially, when all the molecules are in the triplet state, in order to keep the system in a dark state while transferring the molecules to ground state we first switch on the second laser (850nm). At the end of the process when the molecules are in the ground state the first laser should be on and the second laser should be off. While transferring we increase the intensity of the first laser (1320nm) while decreasing the intensity of the second laser. During this the population gets directly transferred to the deepest ground state without populating the excited state as shown in figure 2.10b.

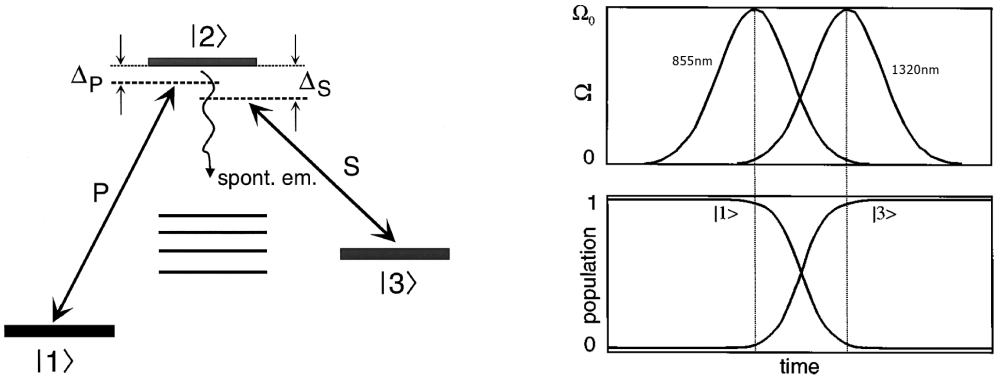

(A) (B)

FIGURE 2.10: A typical three level system(left) and a pulse sequence for the STIRAP transfer.

The excited state is chosen so that the two transitions have a good Frank-Condon (FC) overlap. The potential suitable for this process is a mixed $3\Pi^1\Sigma^+$ which has its inner turning point matching with the equilibrium separation of the $X^1\Sigma^+$ and outer turning point with the inner turning point of $a^3\Sigma^+$. These transitions are expected to have a good FC factors. The transition dipole moments for these transitions are $3 \times 10^{-3} ea_0$ for the pump and $1ea_0$ for the dump.

2.3 Simulation of optimal trapping geometaries for a binary Mott insulator of K and Rb atoms

The production of the ultracold bosonic polar molecules using spectroscopy requires the loosely bound Feshbach molecules created using the Feshbach resonances. But since we have bosonic Feshbach molecules, that are highly excited, can decay via molecule-molecule or molecule-atom inelastic collisions. So it becomes important to prevent their collisions among themselves and with single atoms. These collisions can be suppressed by putting the pairs of K and Rb in a three dimensional optical lattice. Such arrays of the pairs of atoms in a tight optical lattice is called a *Binary Mott Insulator*, where they are described by the localized Wannier waves in the lattice sites. In order to achieve this phase we have to first make a mixture of the condensates of K and Rb with appropriate densities and good overlap.

Rb has a constant scattering length over the range of magnetic fields we work with. Therefore the size of the Rb BEC can only be adjusted by manipulating the trapping geometries. The scattering length of the K atoms can be tuned using the magnetic field to get its condensate volume equal to the Rb condensate. Later we can ramp up the 3D optical lattice over it. This will make the atoms cloud fragmented to lattice sites with required occupancy. Getting control over the occupancy in the experiment is a complex task and depends on many variables. I have built an integrated program which can simulate the zero temperature behaviour of the system. Using this program we can find an optimal approach for the realization of an efficient binary Mott insulator by simulating the KRb mixture in our trapping geometries.

Binary Mott insulator

In the physics of mixtures the influence of interactions becomes complex owing to the fact that interspecies and intra-species scattering length can be different. For an n component mixture the number of interaction terms goes as $n(n+1)/2$. For a binary mixture of A and B there are three types of interactions: $A-A$, $B-B$ and $A-B$.

Depending on these interactions the mixture can mix or separate out to make two BECs of individual species. The condition of miscibility of a two component mixture is given by [16]

$$a_{AA}a_{BB} > a_{AB}^2 \tag{2.4}$$

where a_{AB} is the interspecies scattering length between A and B and a_{AA}, a_{BB} are the intra-species scattering lengths of the components.

For a two component mixture in an optical lattice (1.1.2) the Bose Hubbard Hamiltonian is written as

$$\hat{H}_{AB} = \hat{H}_A + \hat{H}_B + U_{AB}\sum_i \hat{n}_{A,i}\hat{n}_{B,i} \tag{2.5}$$

which is the sum of Bose Hubbard Hamiltonians of individual species (equation 1.16) in the lattice and an interspecies interaction energy term U_{AB}.

The filling pattern of the atoms in the lattice sites depends on the interaction energies U_{AA},U_{BB} and U_{AB} [17]. In order to enhance the paired filling of the two species

$$U_{AB} < U_{AA}, U_{BB} \tag{2.6}$$

In the case of KRb this condition can be achieved easily in the vicinity of the K-K Feshbach resonance at $400G$, where the K-K scattering length can be tuned to large positive values, the interspecies scattering length is $\sim 40a_0$ and the Rb-Rb scattering length is $100a_0$.

2.3.1 Present Experimental Setup

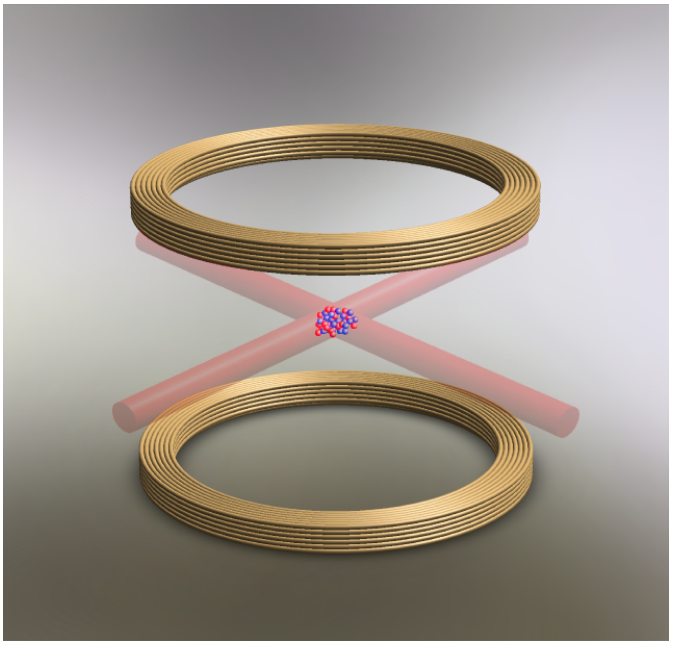

FIGURE 2.11: The setup of magneto-optic trap.

The experimental set-up which we have is designed to get a condensate of ^{39}K with a total number of 3×10^5 atoms at 50nK. The initial mixture of K and Rb is made to go through three stages of cooling before it forms the condensate.

Laser Cooling: In the first stage the mixture is trapped in a magneto-optic trap (MOT) and is cooled using the laser cooling. The sample is cooled down to 100μK with a density around 10^{10}cm^{-3}.

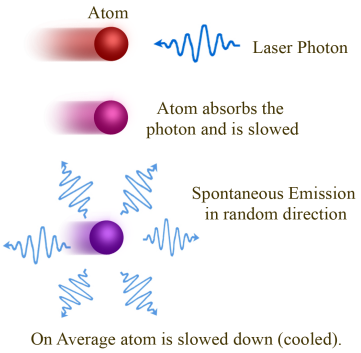

(A) Interaction of photons with atoms during laser cooling

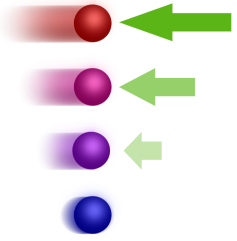

(B) On a statistical average larger retardation seen by atoms moving at larger speeds.

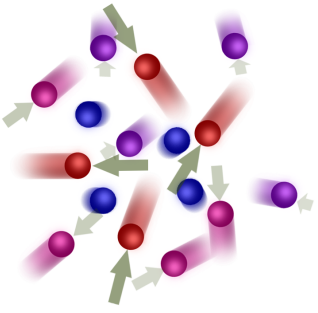

(C) Cooling in bulk.

FIGURE 2.12: The MOT has both trapping as well as cooling effect. The atoms moving away from the center of the MOT absorbs photons of red detuned MOT beams and are on average pulled back to the center as well as slowed.

Selective evaporative cooling in the Magnetic trap: In the second stage, the mixture is first transferred to a the low field seeking state and is cooled by selectively evaporating Rb atoms in a Quic trap to achieve a temperature of 1.5μK.

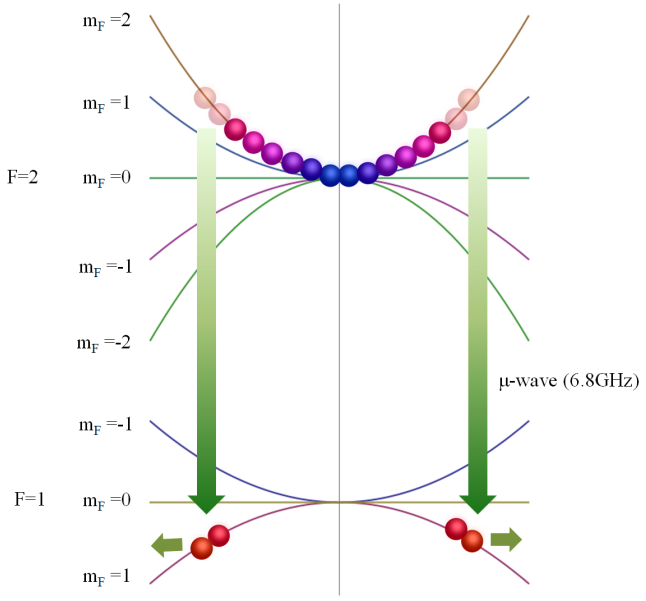

FIGURE 2.13: The selective evaporative cooling by transferring the high energy Rb atoms at the periphery of the Quic trap from $|F = 2, m_F = -2\rangle$ to $|F = 1, m_F = 1\rangle$, which is no longer trappable and hence lost.

In the trapping potential of Quic trap, the atoms which are far from the center possess high energy. In selective evaporative cooling these atoms are transferred using a microwave from low field seeking state $|F = 2, m_F = -2\rangle$ to $|F = 1, m_F = 1\rangle$ state, which is repelled by the Quic trap and hence lost as shown in figure 2.13. By this process Rb atoms are cooled and K atoms are cooled by sympathetic cooling.

Evaporative cooling in the dipole trap: In the third stage of cooling the mixture is cooled by evaporation in two steps and also the scattering length of the mixture is tuned by means of Feshbach resonances. To do so the mixture is first transferred into an optical dipole trap. This trap is created by the intersection of two horizontal red detuned laser beams of waist 80μm. The intensity of these lasers is ramped down exponentially. In the first part the internuclear scattering length is increased and the Rb is evaporated because it has larger mass and shallower trap in the vertical direction. Because of large internuclear scattering length the K is cooled sympathetically. In the second part the intra-nuclear scattering length for K atoms is increased and K is evaporated to a temperature of around 50nk. Rb atoms being heavier are completely lost at this stage.

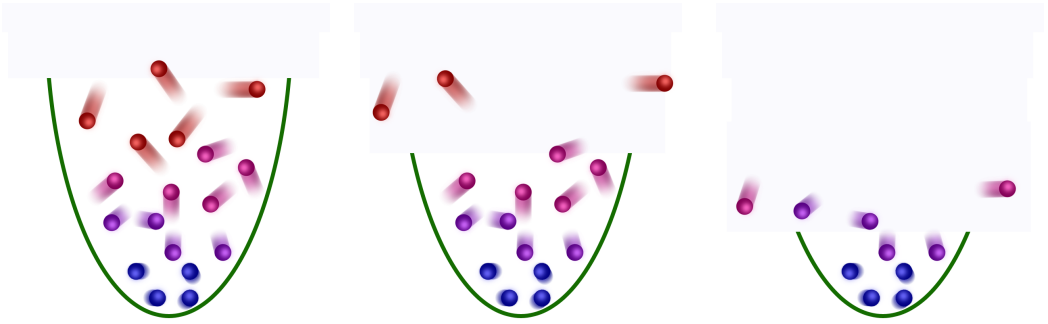

(A) 1 (B) 2 (C) 3

FIGURE 2.14: A schematic showing three stages of evaporative cooling. The strength of the trap potential is ramped down to allow the faster atoms to escape, while the slow ones stay trapped.

Required Goal

Before association the atoms of K and Rb using the Feshback resonances we need the pairs of K and Rb at each lattice site of the optical lattice as shown in the Figure 2.15. For this geometry we first need the density of each of the species to be nearly $1/d^3$ where d is the lattice constant. Secondly we need the two atomic distribution to be overlapping.

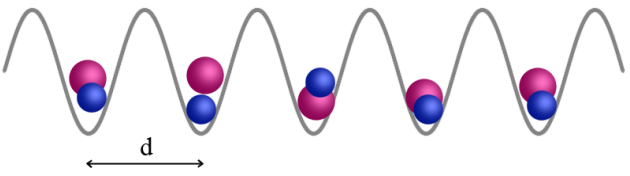

FIGURE 2.15: The required distribution of atoms before they are bound together using a Feshbach resonance.

However in the actual experiment this kind of distribution is challenging to achieve because of the complexity of the trap potential and how differently the two species behave in that potential. The first problem is that the density distribution of the atoms in the trap after condensation is parabolic (Figure 2.16). As per our requirement, we will like to have a flat distribution of one atom per site. Since we cannot change the nature of the trapping geometries, the best we can do is to make the mean density of the atoms to be $1/d^3$ which will maximize the number of atoms to the right density. We can do this by changing the scattering length of the atoms using the magnetic fields as explained in the next section.

The second problem is the separation of the clouds of the two species. The Rb atoms are twice as heavy as K atoms. When both K and Rb are in the same optical trap potential

the heavier Rb atoms get separated from the K atoms along the vertical direction as shown in the figure 2.17. In order to obtain the pairs we need the two clouds overlapping. Two possible solutions to this problem are a modification of the optical trap or the use of magnetic field gradients.

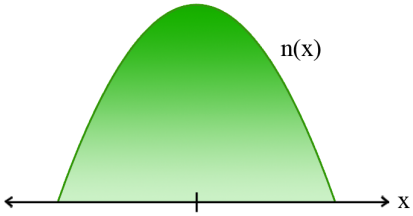

FIGURE 2.16: The distribution of the condensate in the optical trap

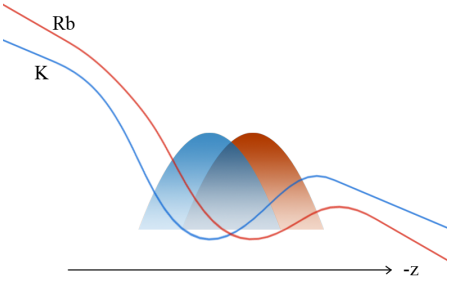

FIGURE 2.17: The potential and the distribution for the two species in the vertical direction.

In our simulation we tried to optimize the choice on the configuration space. In the following sections I explain in detail the various phenomena and strategies.

Tunable experimental parameters

The tunable experimental parameters are the physical parameters in the experimental setup which we can change to achieve different results. These parameters are the following

(a) Power of the dipole trap lasers: The power of the lasers of the trap in which atoms are transferred after the evaporative cooling in the quick trap can have maximum value of 0.8W and it can be ramped down to the desired value during the evaporative cooling in the dipole trap.

(b) Magnetic Field: The spatially constant magnetic field used for to tune the affective scattering length of atoms can be changed from 0 to 410G.

(c) Magnetic Field Gradient: The magnetic field gradient in the upward direction can be used to produce the additional lift against the gravity on the atoms and it can be tuned up to 1000G/m.

(d) Optical Lattice Strength: The strength of the optical lattice is measured in term of the ratio of the lattice depth and the recoil energy. This ratio can be tuned from 1 to 30 by varying the intensity of the lasers forming the lattice.

(e) Zeeman states: We can switch between Zeeman states of K by sweeping appropriate frequency.

2.3.2 Strategies to produce an efficient overlap of K and Rb

With the present laboratory settings if we simulate the condensation of K and Rb, the final Thomas-Fermi distributions along the vertical direction are shown in the Figure 2.18. Clearly, because of gravitational sag, the overlap of the K and Rb is very poor. In order to get a good overlap the first thing to do is to prevent the gravitational sag i.e. we need to lift the Rb atoms against gravity more than K atoms. This can be done in the following ways and can be implemented to the actual experimental setup depending upon their ease.

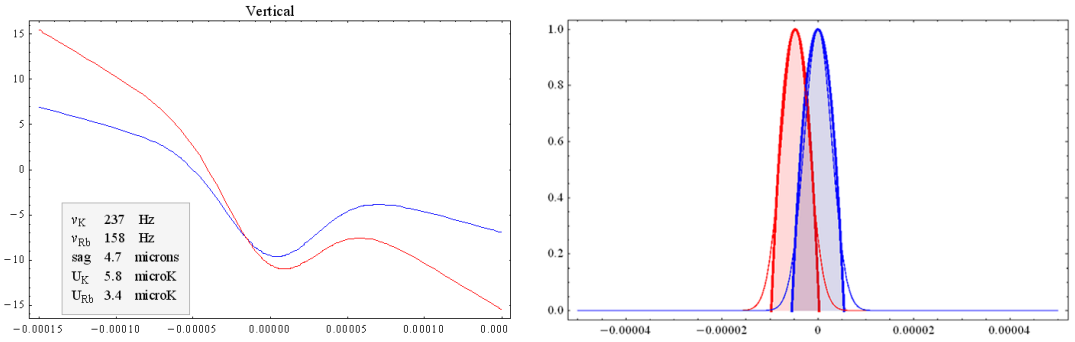

FIGURE 2.18: Left: Potential depths in vertical direction of K (blue) and Rb (Red) after they condense. Rb is shallower because of its heavy weight. Right: The Thomas Fermi distribution of condensates separated due to the gravitational sag.

1. Using Magnetic Field Gradient

When an atom is placed in the magnetic field, because of the coupling between the total electron angular momentum (J) and the nuclear angular momentum (I) the energy of magnetic sub levels vary non-linearly with the magnetic field. This energy for the case of the total electron angular momentum quantum number $J = 1/2$ is given by the Breit-Rabi formula.

$$E_{|J=1/2 m_J I m_I>} = -\frac{\Delta E_{hfs}}{2(2I+1)} + g_I \mu_B m B \pm \frac{\Delta E_{hfs}}{2}\left(1 + \frac{4mx}{2I+1} + x^2\right)^{1/2} \tag{2.7}$$

In this formula g_I is the nuclear g-factor, μ_B is the Bohr magneton, $m = m_I \pm m_J$, hyperfine splitting $\Delta E_{hfs} = A_{hfs}(I + 1/2)$ and

$$x = \frac{(g_J - g_I)\mu_B B}{\Delta E_{hfs}} \tag{2.8}$$

From the Breit-Rabi formula it is clear that if we have a gradient $\delta B/\delta z$ of magnetic field then this will induce a force on atoms and the corresponding potential will be

$$U = \frac{\delta E_{|J=1/2 m_J I m_I>}}{\delta B} \frac{\delta B}{\delta z} z \tag{2.9}$$

We can make use of this force by applying a magnetic field gradient in vertical direction to compensate for the different gravitational pull. In this approach we can apply a magnetic field within the range 80-250G, transfer both K and Rb in their $|F = 1, m_F = -1 >$ state as shown in figure 2.19. In this state a gradient in magnetic field along vertical direction will lift the Rb atoms and pull the K atoms.

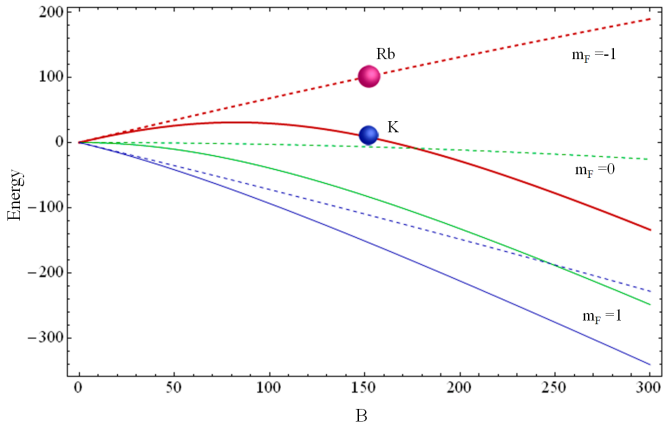

FIGURE 2.19: Energies of K (solid lines) and Rb (dashed lines) versus the magnetic field in their $F = 1$ and different m_F states.

Therefore we can end up with nearly equal depth for both the K and the Rb with the magnetic field gradient range of ∼500-700G/m. In this way we can evaporate the K and the Rb equally and achieve the significant overlap of the two condensates (see figure 2.20).

2. Using different wavelengths for the dipole traps

The general expression for the dipole potential of a laser beam in its cross section resulting from the dipole force is given by

$$U_{dip}(r) = \frac{3\pi c^2}{2\omega_0^3} \frac{\Gamma}{\Delta} I(r) \tag{2.10}$$

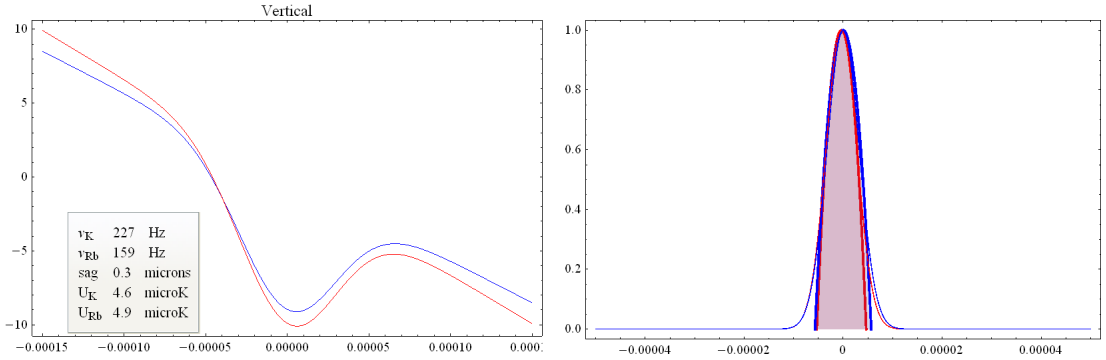

FIGURE 2.20: Left: Potential depths in vertical direction of K (blue) and Rb (Red) after they are condensed in magnetic field gradient of 550 G/m. Right: The condensates of K and Rb significantly overlapping after evaporation.

here ω is the resonant frequency of the two level atomic system, Δ is the detuning of the trap laser ($\Delta = \omega - \omega_0$), Γ is the damping rate due to radiative energy loss and $I(r)$ is the intensity distribution of the laser beam. In case of Alkali atoms (eg. K and Rb) this expression modifies because of the fine structure splitting of the excited state. If the detuning of the laser beam is small compared to this fine splitting as in our case the expression for the dipole potential due to a plane polarized beam is given by

$$U_{dip}(r) = \frac{3\pi c^2 \Gamma}{2\omega_0^3} \left(\frac{2}{\Delta_{2,F}} + \frac{1}{\Delta_{1,F}} \right) I(r) \tag{2.11}$$

where $\Delta_{1,F}$ and $\Delta_{2,F}$ are the detunings of the laser frequency from the centers of the hyperfine splits $^2P_{3/2}$ and $^2P_{1/2}$ excited states as shown in the figure 2.21. The potential depth is dependent on these two detuning values.

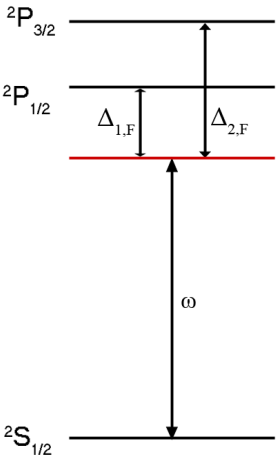

FIGURE 2.21: Fine level scheme of an Alkali atom and the detuning of a frequency ω from the excited state splitting.

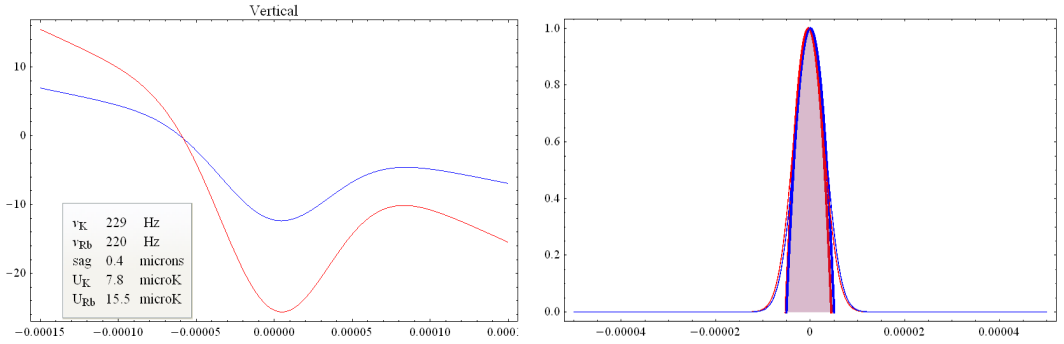

FIGURE 2.22: Left: Potential depths in vertical direction of K (blue) and Rb (Red) after when both the dipole trap lasers have wavelength 808nm. Right: The overlapping Thomas Fermi distribution of condensates of K and Rb after evaporation.

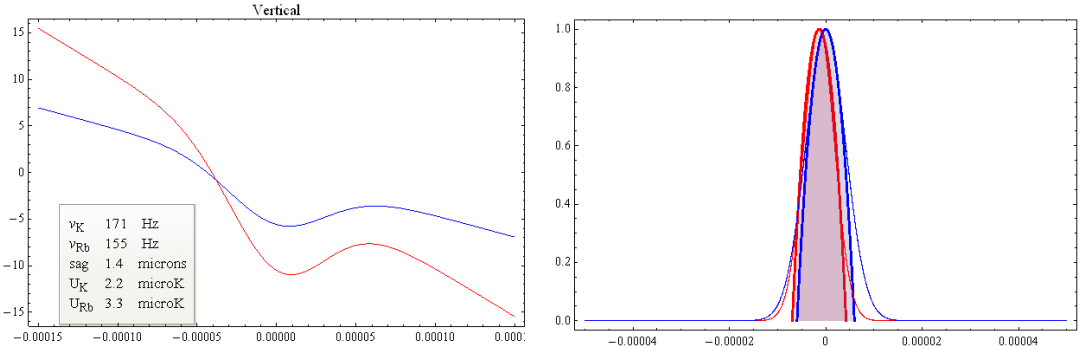

FIGURE 2.23: Left: Potential depths in vertical direction of K (blue) and Rb (Red) after when one of the dipole trap lasers have wavelength 808nm. Right: The overlapping Thomas Fermi distribution of condensates of K and Rb after evaporation.

At present the wavelength for dipole trap lasers is 1064nm. At this wavelength the depth of the potential generated by the lasers is equal for both K and Rb. But we can change this wavelength to the value so that the potential is more deeper for Rb as compared to K. If we replace this by 808 nm the confining force for the Rb becomes double as compared to for the K. So the effect of gravitational pull which is double for Rb can be canceled using this. In this situation as we evaporate, the K condenses before Rb and we have perfect overlap of the two species before and after condensation as shown in figure 2.22.

Changing the wavelength of the both dipole trap lasers can give good results but is experimentally more challenging. To make experimental work easy, an optimum approach is to change the wavelength of the one of the lasers. After changing the wavelength of the one of the lasers the potential in the vertical direction is shown in the figure 2.23. This scheme looks quite promising in the simulation and is experimentally achievable.

2.3.3 Calculation of Densities

Harmonic Trap

The ground state density distribution (Thomas Fermi distribution) of the condensate in a harmonic trap is given by

$$n_{TF} = 1 - \frac{(r - r_0)^2}{R_{TF}^2},\ |r - r_0| \leq R_{TF} \tag{2.12}$$

here r_0 is the displacement of the condensate from the minima of the trap because of the gravitation or the magnetic fields. R_{TF} is the Thomas Fermi radius of the condensate which is given by

$$R_{TFi} = 15^{\frac{1}{5}} \left(\frac{Na}{\bar{a}_{ho}}\right)^{\frac{1}{5}} \bar{a}_{ho} \frac{\bar{\omega}}{\omega_i} \tag{2.13}$$

where N is the total number of atoms, a is the Bohr radius, a_{ho} is the harmonic oscillator length, w is the oscillator frequency, the index i stands for the x,y or z directions and the bar signifies the average of physical quantity over the three directions.

Optical Lattice

When an optical lattice is superimposed over the Harmonic Trap the density distribution modifies because of periodic potential of the optical lattice. The modified Thomas Fermi radius is given by

$$R_{TFi} = 15^{\frac{1}{5}} \left(\frac{Na}{\bar{a}_{ho}}\right)^{\frac{1}{5}} \bar{a}_{ho} \frac{\bar{\omega}}{\omega_i} \left(\frac{d}{\sqrt{2\pi} a_{hol}}\right)^{\frac{3}{5}} \tag{2.14}$$

By approximating the lattice site potential to parabolic potential near the center of the site, the modification factor is found to be

$$\frac{d}{\sqrt{2\pi} a_{hol}} = \sqrt{\frac{\pi}{2}} s^{\frac{1}{4}} \tag{2.15}$$

where s is ratio of the lattice depth and the recoil energy.

The normalized ground state density distribution in three dimensions is given by

$$n_{TF} = \frac{15N}{8\pi R_x R_y R_z} \left\{1 - \frac{(x - x_0)^2}{R_x^2} - \frac{(y - y_0)^2}{R_y^2} - \frac{(z - z_0)^2}{R_z^2}\right\} \tag{2.16}$$

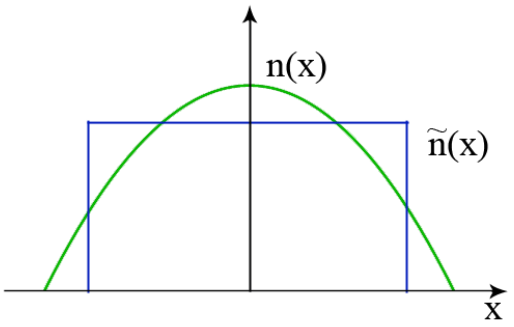

FIGURE 2.24: An approximation of Thomas Fermi distribution $n(x)$ of atoms along one dimension by taking its weighted mean over itself. The approximated distribution $\tilde{n}(x)$ is flat and have less volume to conserve the total number of atoms.

where N is the total number of atoms, R_x, R_y, R_z are the Thomas Fermi radii in the x, y and z directions.

In order to take an average of this distribution it is weighted averaged over itself using the formula

$$\tilde{n} = \frac{\int n^2 dV}{\int n dV} \tag{2.17}$$

This average density is constant over the space and have a smaller radius as shown in Figure 2.24. After evaluation the average of the ground state density distribution is

$$\tilde{n} = \frac{15N}{14\pi R_x R_y R_z} \tag{2.18}$$

Considering the average distribution the number of atoms per lattice site (average occupancy) becomes

$$Occ = \tilde{n}V \tag{2.19}$$

where V is the volume of one lattice site.

Density and number of the pairs in a mixture

We have a mixture of the K and the Rb atoms in an optical lattice. Their densities follow the Thomas Fermi distribution throughout the lattice and they have different Thomas Fermi radii. The centers of the clouds may be separated by some distance. We have to find the average density of pairs of K and Rb in their overlapped region. Suppose that n_K and n_{Rb} are the normalized distributions of K and Rb.

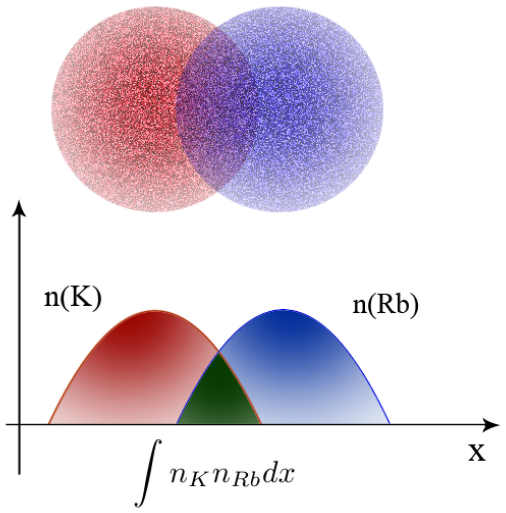

FIGURE 2.25: The overlap of the two normalized density distributions.

The density of pairs depends on the density of species with less number of atoms in the overlapping region. The overlap integral for the two normalized density distributions is

$$n_{Overlap} = \int n_K n_{Rb} dV \tag{2.20}$$

Since the density distributions are normalized, the multiplication of this overlap integral with the total number of atoms of species with less number of atoms will give us the density of the pairs.

$$n_{pairs} = Min\left[N_K \int n_K n_{Rb} dV, N_{Rb} \int n_K n_{Rb} dV\right] \tag{2.21}$$

where N_K and N_{Rb} are the total number of atoms and we choose the smallest density. The density of pairs goes to zero as one of the species density goes to zero. In the case when the total number of atoms is the same for both the species, the density of pairs is only dependent on the distributions and the overlap integral and therefore both the densities in the equation above are the same.

In conclusion the mean density of K weighted over itself is .

$$\tilde{n}_K = \int n_K^2 dV \tag{2.22}$$

Since the total number of atoms are conserved. The effective volume $\tilde{V}_K$ of the mean distribution which is also normalized should satisfy the equation

$$\tilde{n}_K \tilde{V}_K = 1 \tag{2.23}$$

2.3.4 Numerical Simulation

I have built a full numerical simulations of the various strategies described above using *Mathematica*. I tried to design a compact program based on the "Manipulate" command, where all the relevant parameters can be changed by the user and the resulting distributions, energies and occupancies are immediately shown in a set of graphs and tables.

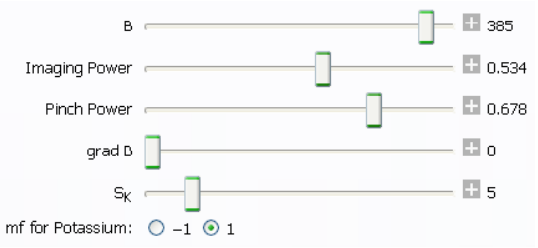

FIGURE 2.26: Tunable input parameters for the simulation.

The simulation starts from the stage when the sample is in the dipole trap, after it has gone through the cooling in the Quic trap. As an input, except the fixed universal and laboratory constants, the tunable experimental parameters are adjusted by the input sliders (Figure 2.26). The first input slider is the Feshbach magnetic field in Gauss. The later two are the laser powers along the imaging and the pinch directions in Watt. The fourth slider tunes the magnetic field gradient in the vertical direction in units of Gauss per meters. The fifth slider changes the strength of the optical lattice. The last radio button is to switch between two m_f states of K.

ν_K	269	Hz
ν_{Rb}	189	Hz
U_K	10.1	microK
U_{Rb}	11.2	microK
a_K	53.7	Bohr
Occupancy_K	6.4	atoms
Occupancy_{Rb}	5.	atoms
U/J_K	1.38	
U/J_{Rb}	28.73	

FIGURE 2.27: The output table showing calculation results of averaged trap frequencies, the trap depth, scattering length for K, occupancy in the optical lattice and the ratio of the interaction energy and the scattering energy.

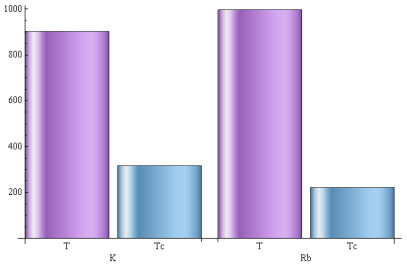

FIGURE 2.28: The temperature and the Critical temperature of K and Rb in nK.

In the output we show potential plots (Figure 2.29) along the three different directions in one column and in another parallel column we show the thermal or the Thomas

Fermi distributions (Figure 2.30) along the three directions. Before the condensation the thermal distribution plot line is thicker and after the condensation the Thomas Fermi distribution plot line is thicker to indicate which distribution is dominant. In each potential or distribution plot diagram since both K and Rb plots are shown so we choose the colour Blue for the K and Red for the Rb. Within the potential plots a box displays the trap frequencies, potential depth and separation between centres of clouds of two species along that direction. Apart from this the temperatures for K and Rb and their critical temperatures are shown in a bar diagram (Figure 2.28).

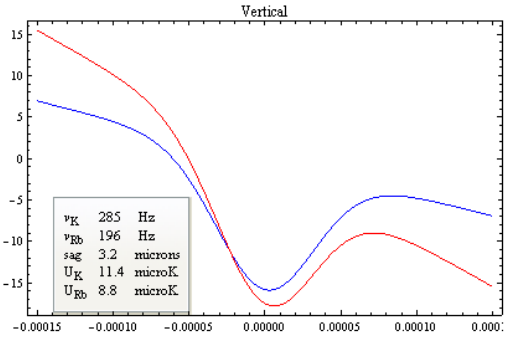

FIGURE 2.29: The potentials for K (blue) and Rb (red) along the vertical direction.

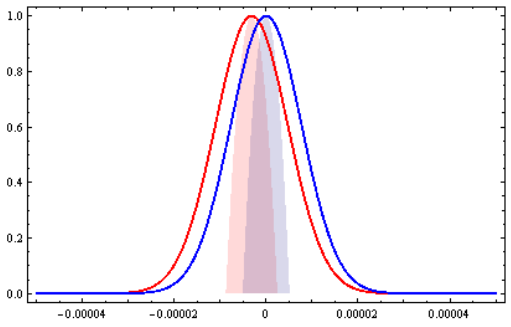

FIGURE 2.30: The distribution of K and Rb along the vertical direction

In a separate box (Figure 2.27) the trap frequencies averaged along three directions, the minimum of the trap depth along three directions, scattering length for K, occupancy in the optical lattice and the ratio of the interaction energy and the scattering energy are shown. These outputs change dynamically as the input parameters (slider positions) are changed.

In the last part, using the methods explained in 2.3.3, the occupancy of the pairs of K and Rb in the dual Mott insulator phase and the total number of pairs obtained is calculated and displayed.

2.4 Conclusions

In the spirit of studying the physics of one dimensional bosons with long range interactions, we want to produce ultracold KRb molecules, which show long range anisotropic interactions. As a first step towards the production of molecules we have to prepare an overlapping two component mixture followed by a binary Mott insulator. The two species can behave differently to the trapping potentials, and their inter and intra species scattering lengths can be different. These features add complexity to this task and one requires a well planned procedure.

There can be many approaches to achieve a double Mott insulator. Among these we would like to follow the most efficient approach with a minimal change in the current laboratory apparatus. Trying all approaches discussed in this chapter directly in the laboratory to find a most efficient one can be extremely timely and tedious task. Therefore we needed a faster and a safer way to plan our approach before making actual changes to the apparatus.

In this chapter after introduction to the 1D physics with molecules and their production scheme, I discussed the working status of the present laboratory setup with introduction to all cooling techniques and trapping potentials used. After that I report all the strategies which can be implemented to form a sufficiently overlapping mixture of K and Rb condensates with right densities. To find the most appropriate strategy among these, I wrote a program which can simulate these approaches computationally.

This simulation program is written by taking into account all known trapping parameters and Zeeman states of atoms which are used in the laboratory. It takes the tunable laboratory parameters as input and generates the real time evolution of the condensate in the trap and finally in the Mott insulator phase. These parameters are given a maximum bounds to their values, which are same as limited in the laboratory. The output changes dynamically as the input parameters are changed using the sliders.

This program is useful in two modes. Through simulation results it can be used to find out whether a particular approach is valid or not to achieve a binary Mott insulator. Secondly for a valid approach it can be used to find the required parameters we will need to set in the laboratory to achieve the binary Mott insulator. For this a desirable output can be simulated easily just by tuning the parameters and those set parameters can be read out. Therefore this is a very useful tool to predict the behaviour of the laboratory setup and to plan the right approach before implementing the actual change in the laboratory apparatus. Using this program, simulations were done for all the strategies and the output of the program is reported at the end of each strategy discussed.

Bibliography

[1] A. Griesmaier, J. Werner, S. Hensler, J. Stuhler, and T. Pfau *Bose-Einstein Condensation of Chromium*, Phys. Rev. Lett. 94, 160401 (2005).

[2] M. Vengalattore, S. R. Leslie, J. Guzman, and D. M. Stamper-Kurn *Spontaneously Modulated Spin Textures in a Dipolar Spinor Bose-Einstein Condensate*, Phys. Rev. Lett. 100, 170403 (2008).

[3] R. Chicireanu, A. Pouderous, R. Barbé, B. Laburthe-Tolra, E. Maréchal, L. Vernac, J.-C. Keller, and O. Gorceix, *Simultaneous magneto-optical trapping of bosonic and fermionic chromium atoms*, Phys. Rev. A 73, 053406 (2006).

[4] M. Lu, S. H. Youn, and B. L. Lev, *Trapping Ultracold Dysprosium: A Highly Magnetic Gas for Dipolar Physics*, Phys. Rev. Lett. 104, 063001 (2010).

[5] K. Aikawa, A. Frisch, M. Mark, S. Baier, A. Rietzler, R. Grimm, and F. Ferlaino, *Bose-Einstein Condensation of Erbium*, Phys. Rev. Lett. 108, 210401 (2012).

[6] K.-K. Ni, S. Ospelkaus, M. H. G. de Miranda, A. Péer, B. Neyenhuis, J. J. Zirbel, S. Kotochigova, P. S. Julienne, D. S. Jin, and J. Ye, *A high phase-space-density gas of polar molecules*, Science 322, 231 (2008).

[7] K. Aikawa, D. Akamatsu, J. Kobayashi, M. Ueda, T. Kishimoto and S. Inouye, *Toward the production of quantum degenerate bosonic polar molecules,* $^{41}K^{87}Rb$, New J. Phys. 11, 055035 (2009).

[8] Xiaolong Deng, Roberta Citro, Edmond Orignac, Anna Minguzzi and Luis Santos *Bosonization and entanglement spectrum for one-dimensional polar bosons on disordered lattices*, New Journal of Physics, 15 (2013).

[9] Emanuele G. Dalla Torre, Erez Berg, and Ehud Altman, *Hidden Order in 1D Bose Insulators*, Phys. Rev. Lett., 97, 260401 (2006).

[10] T. Roscilde, *Bosons in one-dimensional incommensurate superlattices*, Phys. Rev. A 77, 063605 (2008).

[11] G. Roux, T. Barthel, I. P. McCulloch, C. Kollath, U. Schollwöck, and T. Giamarchi, *Quasiperiodic Bose-Hubbard model and localization in one-dimensional cold atomic gases*, Phys. Rev. A 78, 023628 (2008).

[12] B. Londoño, D. Borsalino, O. Dulieu, N. Bouloufa and E. Luc, *Prevision of a STIRAP transfer to rovibronic ground state of ultracold KRb molecules using the 0^+(4s + 5p) electronic states*, unpublished.

[13] A. Simoni, M. Zaccanti, C. D'Errico, M. Fattori, G. Roati, M. Inguscio, and G. Modugno, *Near-threshold model for ultracold KRb dimers from interisotope Feshbach spectroscopy*, Phys. Rev. A 77, 052705 (2008).

[14] W. C. Stwalley *Efficient conversion of ultracold Feshbach-resonance-related polar molecules into ultracold ground state ($X^1\Sigma^+$ v = 0, J = 0) molecules*, EPJD, 31, 221 (2004).

[15] K. Bergmann, H. Theuer, and B. W. Shore , *Coherent population transfer among quantum states of atoms and molecules*, Rev. Mod. Phys. 70, 1003-1025 (1998).

[16] S. B. Papp, J. M. Pino, C. E. Wieman, *Studying a dual-species BEC with tunable interactions*, arXiv:0802.2591 (2008).

[17] S. Sugawa, K. Inaba, S. Taie, R. Yamazaki, M. Yamashita and Y. Takahashi, *Interaction and filling-induced quantum phases of dual Mott insulators of bosons and fermions*, Nature Physics 7, 642–648 (2011).

Chapter 3

Realization of an ultrastable laser setup for molecular transfer

For the production of the molecules we will loosely bind the pairs of K and Rb atoms from the double Mott insulator using a Feshbach resonance and then transfer these molecules to deeply bound rovibronic ground state using Stimulated Raman Adiabatic Passage (STIRAP). For this we will use two diode lasers at wavelength 1320nm for the pump and 855nm for the dump. This spectroscopic technique needs a very stable laser system. This chapter reports on results and the technique of stabilization of the laser setup which will be used for the STIRAP transfer.

3.1 Ultracold molecules

Realizing the molecules at quantum degeneracy is a much difficult task as compared to atoms. Due to the complex structure of molecules, they exhibit various internal degrees of freedom like electronic, vibrational and rotational energy levels. This makes the traditional two level laser cooling difficult in the case of molecules. The temperate attained by other cooling techniques like buffer gas cooling [1], Stark deceleration [2] are in the range of 10-100mK. An alternative is to start from a ultracold mixture of atoms, where quantum degeneracy is achievable and associate them to form molecules. This association needed to be done without heating the gas. The energy difference between two free atoms and deepest bound state of a diatomic molecule can be thousands of Kelvin. This binding energy should be avoided to be released in the form of Kinetic Energy. A possible way to avoid this is using *photoassociation* [3].

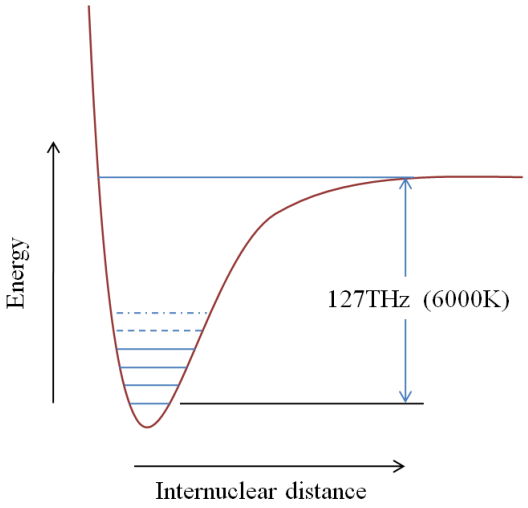

FIGURE 3.1: The difference between the energy of two free K and Rb atoms and the rovibrational ground state.

In a photoassociation technique a scattering state of two atoms is excited to an electronic molecular state from where it radiatively decays to a molecular bound state through spontaneous emission. In this is process the binding energy is released in the form of photons instead of kinetic energy. The temperature achieved by this technique is 100μK. However in spontaneous emission, the linewidth of the excited state leads to a distribution in the final states and the process ends by populating many hyperfine rotational and vibrational states of the molecule.

3.1.1 Coherent transfer scheme

To avoid the spontaneous emission, we can use two different frequencies in Raman scheme, in order to have stimulated emission towards the target state. This implementation solves the problem of heating, since the spontaneous emission is completely canceled. A very efficient scheme for such transfer is Stimulated Raman Adiabatic Passage (STIRAP).

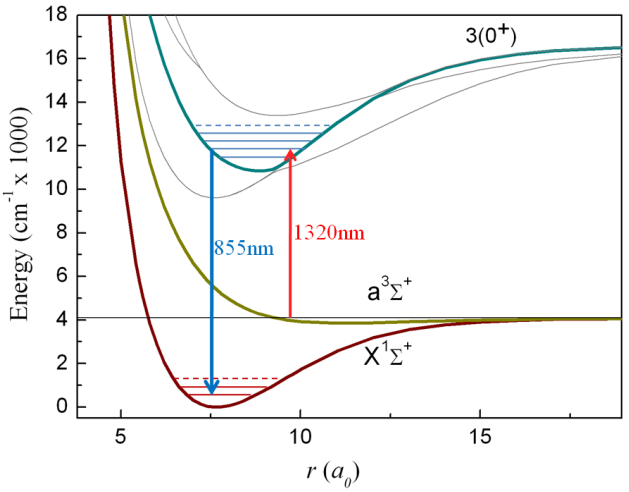

FIGURE 3.2: The transfer scheme from the KRb Feshbach molecules to the rovibrational ground state.

As briefly discussed in section 2.2, in the case of KRb, our production scheme for molecules will start with the Feshbach association of molecules with a vanishing binding energy. These molecules being predominantly triplet will be transfered to singlet ground state molecules using two photon Raman transfer. The intermediate excited state we have chosen is $3(0^+)$ (which is a mixed 3Π–$^1\Sigma^+$). This intermediate level is exptected to have high Frank-Condon overlap and the laser frequencies needed for these transitions are: 1320nm for the pump (primary) laser and 855nm for the dump (secondary) laser.

During the transfer we will excite to one of the hyperfine states of this potential. To find an appropriate level with strong coupling, in the first step we will carry *association spectroscopy*. In which we will scan the pump laser over various rotational and vibrational energy states of the excited state potential. After finding this state we will fix the wavelength of the primary laser to this value and scan the secondary laser to observe the *dark resonance* (resonance with the absolute ground state).

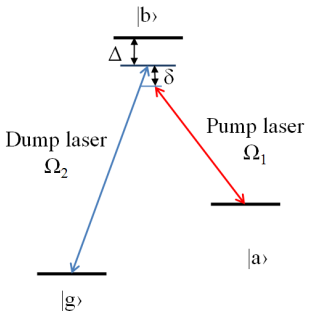

FIGURE 3.3: Three level system involved in the STIRAP process. $|a\rangle$ is the weakly-bound Feshbach state, $|b\rangle$ is the excited electronic state and $|g\rangle$ is the absolute ground state of the dimer.

As the excited state has very small radiative life time (15ns), we will use STIRAP scheme and exploit the eigenstate of the three level system in which contribution of the excited state is null.

For a three level system shown in figure 3.3 the dark eigenstate obtained from the time dependent Schrödinger equation is written as

$$|\Psi_{DS}\rangle = \frac{1}{\sqrt{\Omega_1^2 + \Omega_2^2}} \left(\Omega_2 |a\rangle - \Omega_1 |b\rangle\right) \tag{3.1}$$

where Ω_1 and Ω_2 are the Rabi frequencies for the pump and the dump lasers. Actually, if initially the whole population is in state $|a\rangle$, to transfer it to the ground state while keeping the system in the dark state one has to first switch on secondary laser alone (Ω_1=0), in order to have $\langle\Psi_{DS}|a\rangle$=1. Conversely, at the end of the transfer process only primary laser must be on in order to have $\langle\Psi_{DS}|g\rangle$=1. During the transfer the secondary laser is switched off and primary laser is switched on and the population transfers directly from the initial state to the ground state. The efficiency of the transfer depends on the stability of the lasers and transition dipole strengths. The intermediate state which we have decided have the transition dipole moments: $3 \times 10^{-3} e a_0$ for the pump and $1 e a_0$ for the dump.

Requirements

For the ground state transfer of molecules apart from the transition dipole moments, the line width of the Raman lasers and their relative frequency stability are crucial. Since any frequency noise on the lasers will be converted into the temperature (10kHz$\simeq$500nK), to stay within quantum degeneracy, the individual lasers are needed to be line narrowed up to $<$ 10kHz.

After the two Raman lasers are line narrowed to a desired value using an external cavity, for the STIRAP tranfer, lasers should have a stable frequency difference. The external cavities to which the lasers are locked can independently undergo slow drifts, leading to a phase unstability among the lasers. An easy way of looking at their relative stability is to observe the beating between two lasers. However for a range of 1320nm and 855nm the frequency differece is 127THz which cannot be detected by usual photodiode. Another method is to lock lasers to the same cavity. But this technique is unsuitable when we have also to scan the lasers over different hyperfine states in order to find efficient transitions. The best approach for this problem is to lock the lasers to two teeth of a stable optical frequency comb as shown in figure 3.4. This technique have been used before for the phase locking of the lasers to produce ultracold molecules [4].

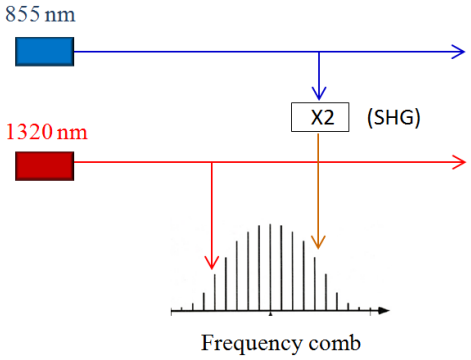

FIGURE 3.4: Scheme to phase lock two lasers using a frequency comb reference. The frequency comb used is an Infra red fiber-based comb locked to a radio-frequency reference.

For the association spectroscopy we have to tune the primary laser up to a wide range (hundreds of GHz) to find a relevant and most efficient excited state. Hence we characterized this laser by tuning it by various ways going from the fine to coarse tuning (3.2.1).

In order to mark the association spectral lines we require a wavemeter to measure the absolute wavelength of the lasers. Since we will use a combination of frequency comb and wavemeter the required accuracy of the wavemeter should be <125MHz.

3.2 Diode lasers

We had purchased two commercial diode lasers at wavelengths 855nm and 1320nm. The laser at 1320nm is the primary laser (for the up going transition) for the STIRAP transfer and the one at 855nm is the secondary laser (for the transfer to the ground state). They have a free running line width of the order of 300kHz. Their output powers are 170mW and 50mW respectively. Their tuning ranges are 1307-1363nm and 842-860nm respectively.

3.2.1 Tuning of primary laser

Typically a grating stabilized diode laser works by resonating the light in the laser cavity formed with a laser diode on one end and a grating at some angle on the other end. The part of radiation which is reflected back in the direction of incident light gets locked in the cavity and leads to resonant modes which are emitted from the grating side as shown in figure 3.5. The laser diode is coated with an anti-reflection coating on the front

end and a reflecting coating at the back end. The mount of the grating is movable by a piezoelectric ceramic which can be adjusted by applying a voltage across the piezoelectric ceramic. The coarse angle of the grating can be adjusted by a screw which pushes the grating. The whole diode and grating assembly is temperature stabilized by means of a Peltier cell and a temperature sensor.

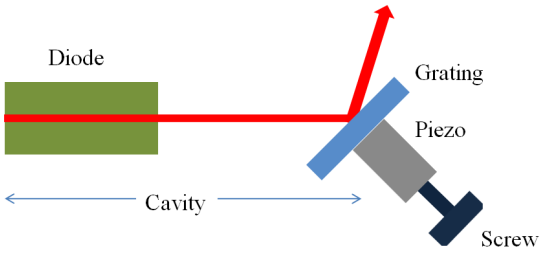

FIGURE 3.5: Schematic of an assembly of a diode laser. The light emitted from the diode is get partially reflected back from the grating. The grating and the back end of the diode forms a resonator. The grating angle can be changed coarsely by a screw and precisely by applying voltage across the piezo which is pushing it.

The cavity formed by the grating and the diode selects its modes within the gain curve (figure 3.6). In the output of the laser we see the most dominant mode among these modes. Since the anti reflection coating on the front end of diode is not perfect, there is an additional cavity formed by the diode itself, with its own modes which are relatively much weaker. When the tuning parameters are changed these modes drift relative to each other. We see sometimes multimodes when two modes of the cavity are competing and a mode jump when the next neighbour mode becomes more stronger due to the relative drift of gain curve and diode modes. The tuning can be done in the following ways.

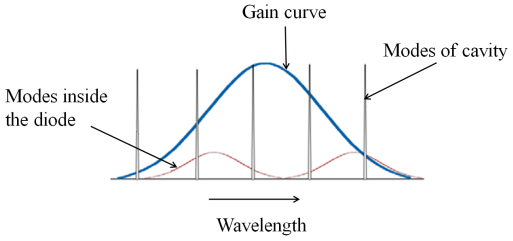

FIGURE 3.6: Gain curve, modes of cavity and modes inside the diode.

Changing the laser current

Changing current in the diode is the finest way of tuning. When we increase the current the wavelength increases. There is a mode jump at 100mA and a region of multimode operation (178mA to 214mA) as shown in figure 3.7. In the mode hope free regions the slope from the plot is $2.984 \text{x} 10^{-4}$ nm/mA. When the current is changed the parameters which change are the band gap of semiconductor, refractive index, temperature and hence the length. The effect of decreasing the band gap of semiconductor is that the gain curve shift towards longer wavelength. The effect of change in refractive index and temperature changes the optical length of the cavity. In a combined effect of these changes we see that overall increase in the wavelength with current.

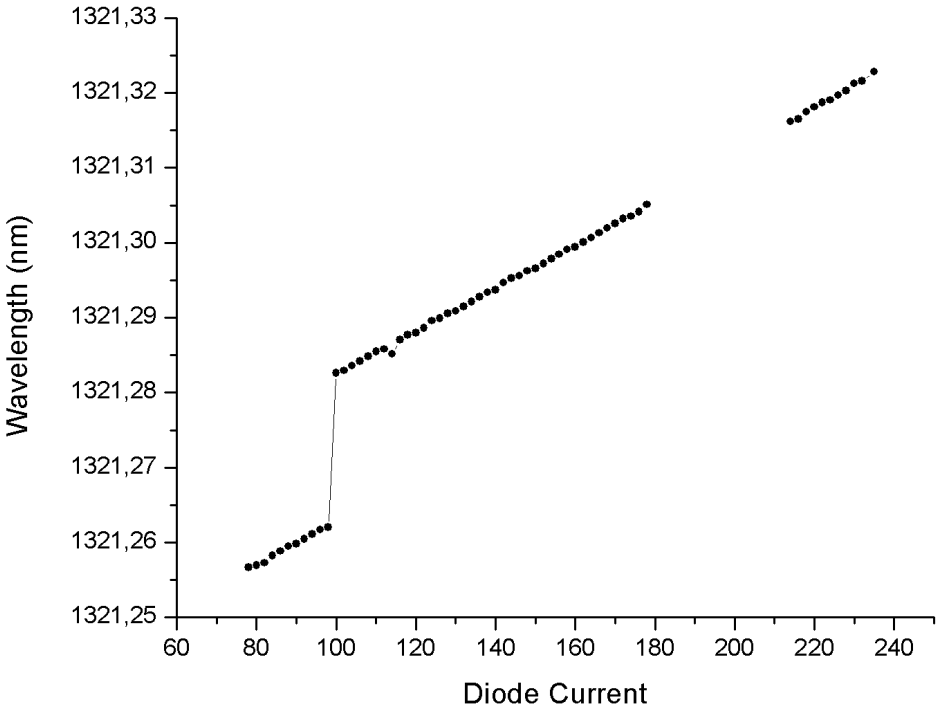

FIGURE 3.7: The wavelength versus the diode current of the laser, keeping all other tuning parameters fixed (T=20 °C). The plot shows one mode jump and a multimode region(missing points).

Changing the temperature

Changing the temperature is the second most accurate way of tuning the laser. The behaviour of the laser is similar to that observed while tuning by current. The only

difference is that since this a relatively coarse tuning, the change is larger and hence there are more mode jumps over the full tuning range as shown in figure 3.8.

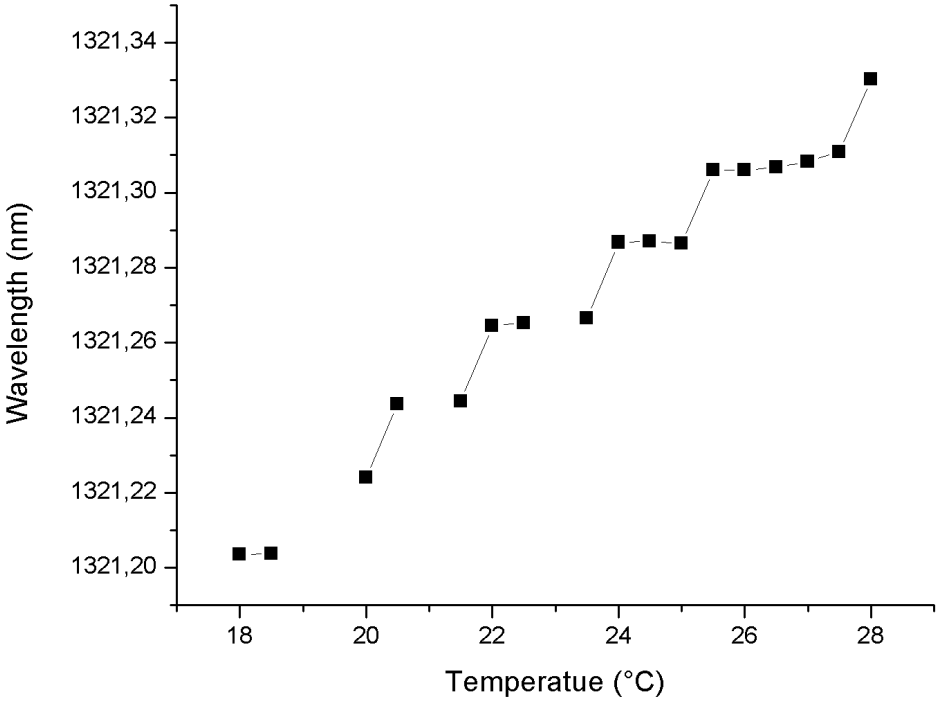

FIGURE 3.8: The wavelength versus the temperature of the laser keeping all other tuning parameters same (Current=113mA). The plot shows many mode jump and multimode region.

Changing the voltage across the piezoelectric ceramic

When the voltage across the piezo is increased we observe a decrease in the wavelength. When the piezo voltage is increased then it pushes the grating towards the diode to make the cavity shorter and it also changes the orientation of the grating. The change in the orientation of the grating changes the wavelength of that part of radiation which is reflected back and gets locked in the short cavity. In this case the combined effect of this change and the cavity length is a shift towards the shorter wavelength. This voltage controlled tuning is used to make ramps to lock the lasers to the external cavity.

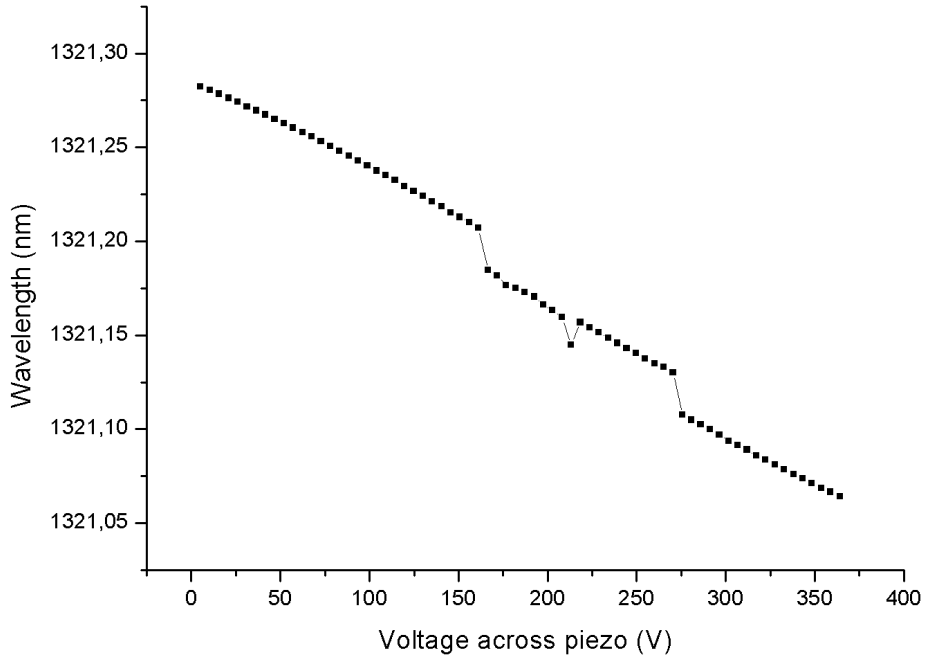

FIGURE 3.9: The wavelength versus the voltage across the piezo of the laser keeping all other tuning parameters same (T=25 °C, Current=113mA). The plot shows few mode jumps.

Manual tuning

While changing the orientation of the grating manually it is difficult to move it in equal steps of known amount. This method covers the wavelength range roughly from 1307nm to 1363nm.

Mode-hop free tuning

While locking the laser to an external cavity, when we scan the laser by applying the voltage ramps across the piezo, we want the scanning to be without mode jumps. For a moderate scan (<20V) we can most likely find a mode hop free scan for a large range of the voltage offsets as seen in the plot in figure 3.9. However it is possible that at a particular value of the current and the temperature while making the required scan the laser mode shifts and a mode jump appears in the ramp. These mode jumps are caused by the relative motion of the internal diode modes and the external grating modes in the frequency. When we change the voltage across the piezo the external grating modes moves with respect to the internal diode modes. This can be prevented if we also move

the laser diodes internal modes to reduce their relative motion during the scan. Therefore we can apply a current ramp to the laser diode proportional to the voltage ramp which changes the refractive index of the semiconductor material and consequently the length of the internal resonator leading to the movement of its internal modes. This additional ramp to the current is called the Feed Forward and can be activated when needed.

3.3 Scanning the Fabry Perot cavity

Because the laser has a short cavity, it is inherently not very stable in frequency. The sources of frequency noise can be the mechanical noise in laser, temperature drifts, laser driver current and voltage fluctuations, atomic transition widths etc. It has a free running line width of 200kHz. We need to narrow down its line width to the order of 10kHz. Thus in order to increase its stability we will lock it to an external high finesse Fabry Perot cavity.

Fabry Perot cavity

When light is injected in a cavity (resonator) the light confined will reflect multiple times from the mirrors of the cavity. Due to the effects of interference, only certain patterns and frequencies of the radiation will be sustained by the resonator, with the others being suppressed by destructive interference. In general, radiation patterns which are reproduced on each round-trip of the light through the resonator are the most stable, and they are known as eigenmodes (or modes) of the resonator. The most common types of optical cavities consist of two facing plane or spherical mirrors. The spherical mirrors are preferred because of their ease towards the alignment. The radiation which is resonating inside a cavity can be stable or unstable depending on the separation and radii of curvature of the mirrors. The stability condition is given by

$$0 < \left(1 - \frac{d}{R_1}\right)\left(1 - \frac{d}{R_2}\right) < 1 \tag{3.2}$$

where d is the spacing between the mirrors and R_1, R_2 are the radii of curvatures of the mirrors. If the cavity is outside the stability condition the light beam will go on diverging after multiple reflections and finally will go beyond the apertures of the mirrors.

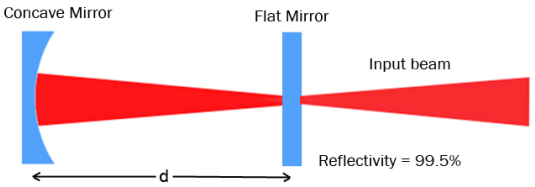

FIGURE 3.10: A cartoon showing a Fabry Perot Cavity with one plane mirror and the other concave mirror, separated by a distance to have the focus of concave mirror at the plane mirror.

Beam propagation inside the cavity

In a stable optical resonator, there are specific transverse field configurations which maintain their field distribution after successive round trips. These field configurations are referred to as the transverse modes of the resonator. Since oscillations of the laser would occur in modes which do not have excessive loss on successive reflections, it is clear that the modes that would oscillate would be the ones which propagate more or less along the axis of the resonator and which do not diffract appreciably as they propagate between the mirrors. The fundamental transverse mode has approximately a Gaussian field distribution, i.e the mode is described by

$$\psi(x,y) = \psi_0 exp\left[-\frac{x^2+y^2}{w_0^2}\right] \tag{3.3}$$

where w_0 represents the spot size of the beam. Figure 3.10 shows a simple resonator configuration consisting of a plane mirror and a spherical mirror separated by a distance d. This is the configuration we used in our cavity setup. We consider a Gaussian beam such that its wavefront coincides with the radii of the mirrors. Thus the phase front is assumed to be plane at $z = 0$. If the spot size of the beam at flat mirror is w_0, then after propagating through a distance z, the radius of curvature of the phase front will be

$$R \approx z\left[1+\frac{\pi^2\omega_0^4}{\lambda^2 z^2}\right] \tag{3.4}$$

If we have a fixed radius of curvature and separation between the mirrors fixed then we can find the required spot size at flat mirror by rearranging the equation 3.4.

$$\omega_0 = \sqrt{\frac{\lambda d}{\pi}}\left(\frac{R_2}{d}-1\right)^{\frac{1}{4}} \tag{3.5}$$

Resonant modes

After the injection inside a cavity the part of the radiation which is exactly along the axis interferes after two reflections and makes the fundamental modes with the condition that 2d is equal to the integral multiples of wavelengths. The other part of the beam suffers multiple (more than two) reflections and then interferes constructively to make rectangular (higher order) modes. The frequency separation between the two fundamental modes is called *Free Spectral Range* (FSR) and is given by

$$\nu_0 = \frac{c}{2d} \tag{3.6}$$

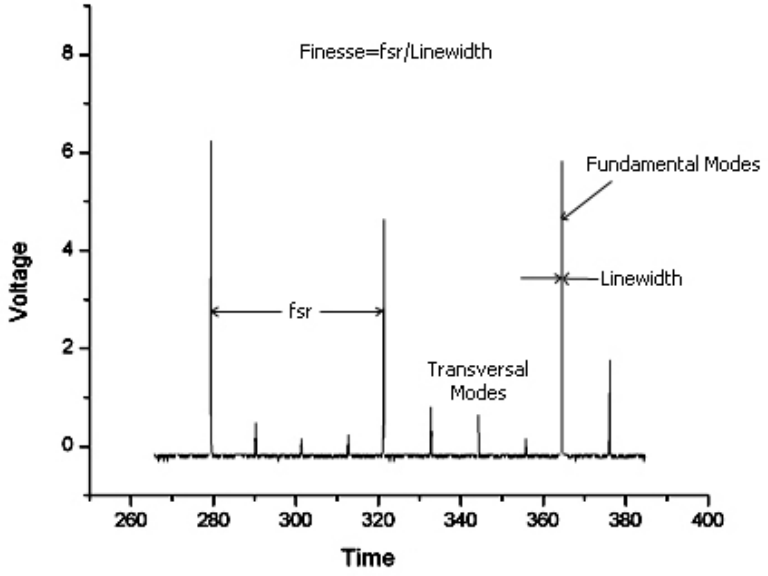

FIGURE 3.11: The cavity scan with the laser injected showing the fundamental mode and higher order (transversal) modes.

The resonant frequency in terms of the fundamental mode separation (FSR) is given by

$$\frac{\nu}{\nu_0} = (q+1) + \frac{(m+n+1)}{\pi} arccos\sqrt{\left(1-\frac{d}{R_1}\right)\left(1-\frac{d}{R_2}\right)} \tag{3.7}$$

Here d is the separation between the mirrors and q is the fundamental mode number and m and n are the rectangular mode numbers. Inside our cavity we have set the separation between the mirrors to 110mm. The radii of curvature of mirrors are -250mm and -1000mm with reflectivity 99.5%. So the resonant frequency is given by

$$\frac{\nu}{\nu_0} = (q+1) + (m+n+1)\,0.2505 \tag{3.8}$$

The calculated free spectral range is

$$\nu_0 = 1363MHz \tag{3.9}$$

The theoretical finesse of a cavity made by two mirrors of reflectivity R is given by

$$F = \frac{\pi R^{\frac{1}{2}}}{1-R} \tag{3.10}$$

For our setup the theoretically calculated finesse is 626 hence the calculated line width of the cavity is 2.177MHz.

3.3.1 Optical cavity setup

We have two optical cavities made of INVAR with an adjustable mirror separation. The radii of curvatures of the mirrors we had were -1000mm and -250mm respectively. We did put the cavity in the hemispherical configuration as shown in the figure 3.10 with one mirror nearly flat and one concave mirror. The perfect separation for the two mirrors for this configuration should be 125mm and the modes will be given by the equation

$$\frac{\nu}{\nu_0} = (q+1) + \frac{(m+n+1)}{4} \tag{3.11}$$

At this value of d the higher order modes, for which $(m + n + 1)$ is a multiple of 4, will coincide with the fundamental mode. However due to experimental imperfections these superimposed higher order modes can distort the symmetry of the fundamental mode (transmission or reflection) profile. While stabilizing we will lock the lasers to the fundamental mode which is the strongest among all. This distortion will eventually lead to an asymmetry in the error signal while locking. Thus to prevent this overlap we have chosen the length of the cavity to be around 110mm.

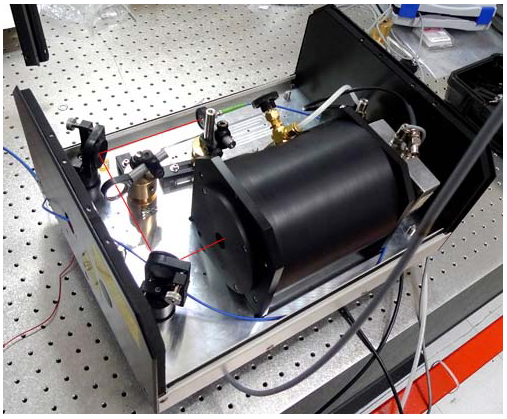

(A) Photograph of the thermally stabilized vacuum chamber in which the cavity is placed.

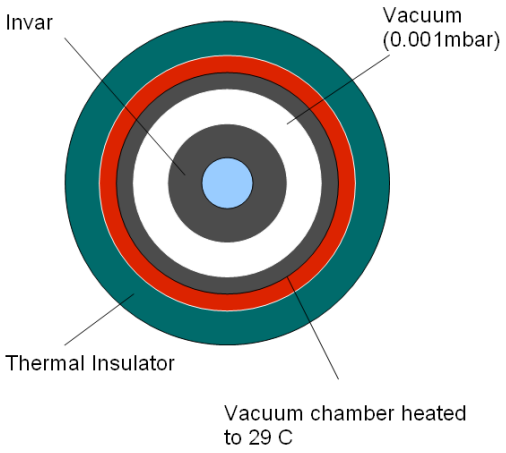

(B) The crossection of the chamber shown in figure 3.12a.

FIGURE 3.12: The cavity under vacuum setup.

To reduce the noise on the cavity we had put it in a vacuum chamber and stabilized its temperature. This container is shown in the figure. The setup in which the cavity is put has an outermost layer which is the thermal insulation. Then inside there is a heating system for the temperature stabilization around the chamber. The temperature was set at 29 degree Celsius. The chamber has a vacuum set at 0.001mbar. The beam is carried to the cavity using an optical fiber.

Modes inside the cavity after injection

In order to mode match the injection with the beam of wavelength 1320nm, we entered with a beam focused at the flat mirror. The waist size at the flat mirror is 230μm satisfying the equation 3.4. Figure 3.13 shows the transmission modes over the laser scan for a well aligned cavity.

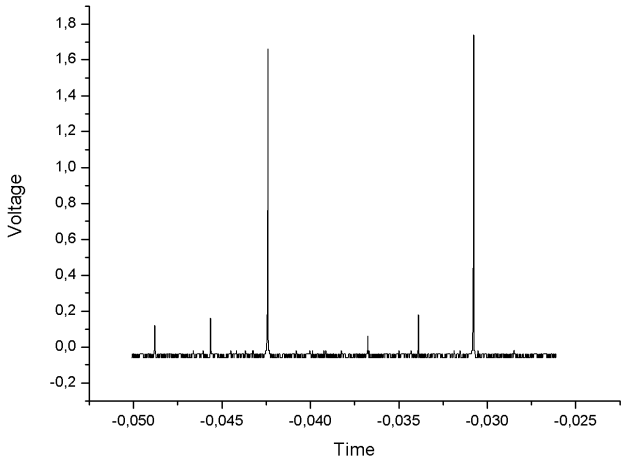

FIGURE 3.13: The cavity scan with the 1320nm laser injected and well aligned showing the fundamental mode and higher order (transversal) modes.

When the laser is kept at one particular transmission line in the output beam, we can see the patterns of that particular transmission mode. Figure 3.1 shows images of these mode patterns captures on a CCD.

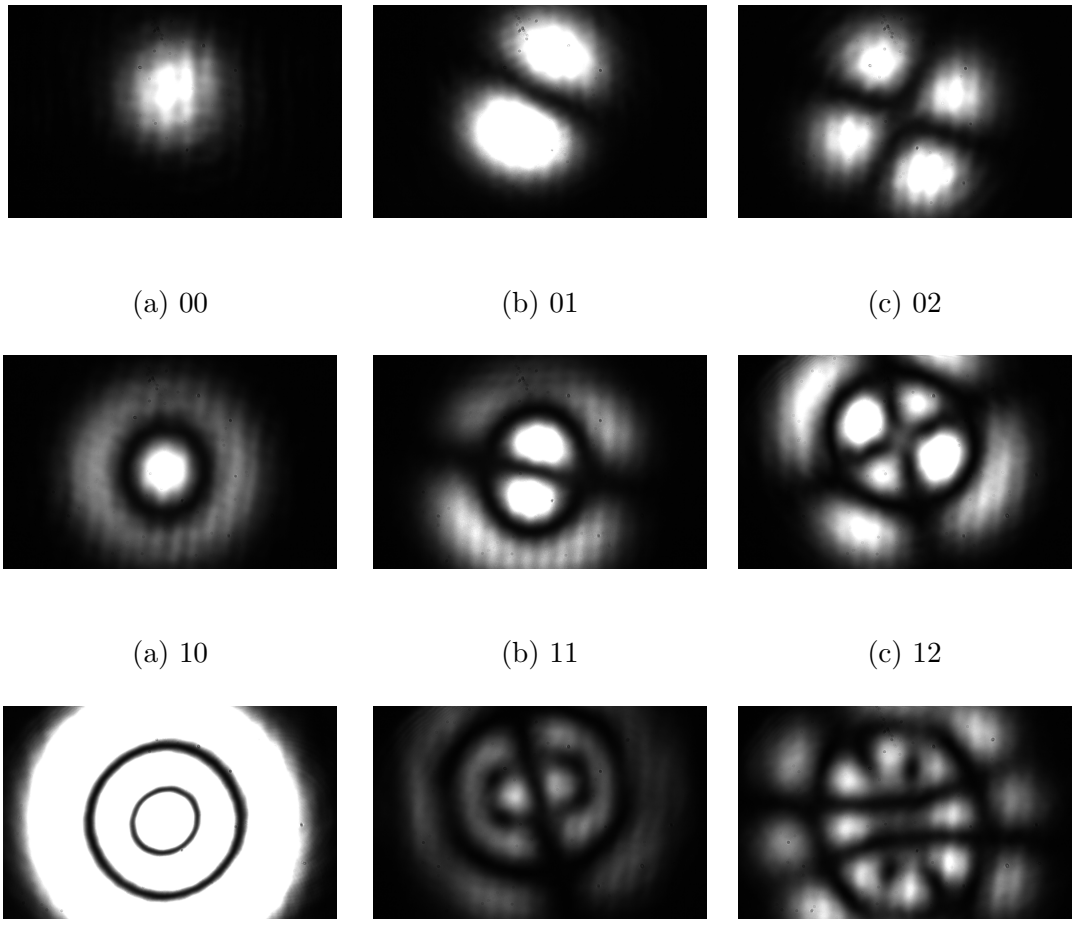

(a) 00 (b) 01 (c) 02

(a) 10 (b) 11 (c) 12

(a) 20 (b) 21 (c) 18

TABLE 3.1: Various transmission modes captured on CCD.

Line-Width

The transmission line of the cavity after injecting the 1320nm wavelength is shown in the figure below. The experimental finesse is the ratio of the separation between the fundamental modes and the line width as shown in figure 3.11. From the plot analysis the finesse calculated after curve fitting is 442.98 and the line width(FWHM) calculated is 3.08MHz. This line width is a convolution of the laser line width (200kHz) and the cavity line width.

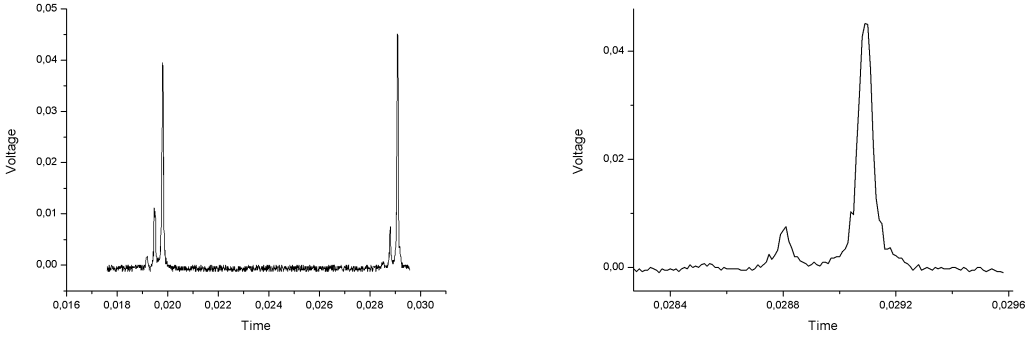

(A) The transmission peaks with the fundmental mode (right most peak) and higher order modes.

(B) The zoomed fundamental transmission peak from the plot 3.14a).

FIGURE 3.14: The transmission lines from the cavity injected with 1320nm wavelength laser.

Nevertheless this large line width as compared to the theoretical predictions can be explained as due to the noise on the laser and on the cavity and also the inaccuracy of curve fitting. In this case the line width was calculated from the plot 3.14 by extracting the separation between the peaks and the with of the peaks. However because of less data points on around the peak leads to larger error. A more precise value of line width will be calculated in section 3.4.2.

3.4 Pound–Drever–Hall laser frequency stabilization

As discussed before since the lasers are not stable up to the requirements for the STIRAP scheme, we will stabilize them by frequency locking to an external resonator. Pound-Drever-Hall (PDH) frequency stabilization is an effective method to frequency stabilize the laser with respect to an external Fabry-Perot cavity [6].

In this technique the frequency is phase modulated using an Electro-optic modulator (EOM) to create two side bands before injecting into the cavity. The signal from the cavity is seen on a fast photodetector. This signal is then mixed with a phase shifted local oscillator to achieve the error signal.

3.4.1 PDH setup scheme

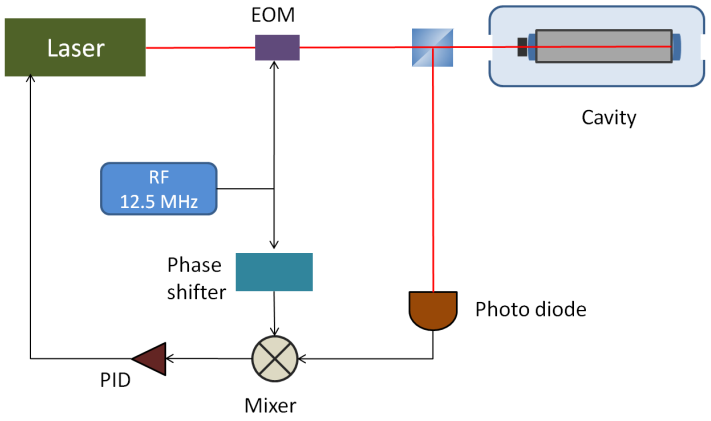

FIGURE 3.15: Schematic of PDH locking loop.

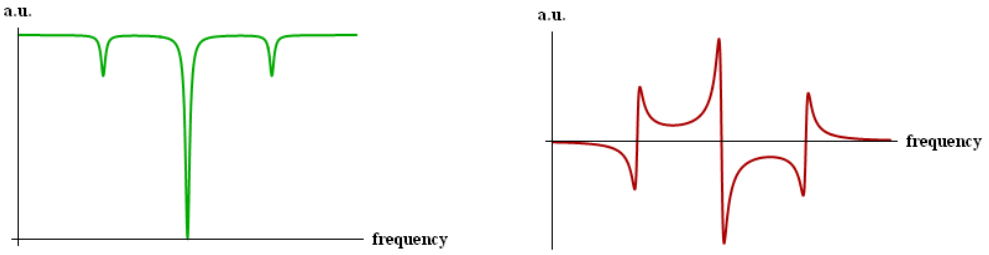

(A) (B)

FIGURE 3.16: The simulated reflection and PDH signals.

Suppose the laser is at a frequency ω, then the radiation emitted from it can be written as $E_0 e^{i\omega t}$. This beam passes through an electro-optic modulator (EOM) which modulates the phase of the beam. Assuming the modulation frequency is ω_m and the amplitude is A_m then the radiation field after it passes the EOM can be written as

$$E = E_0 e^{i\omega t + iA_m sin(\omega_m t)} \tag{3.12}$$

This equation can be expanded using the Bessel functions to obtain

$$\begin{aligned} E &= E_0 \left[J_0(A_m) + 2iJ_1(A_m)sin(\omega_m t)\right] e^{i\omega t} \\ &= E_0 \left[J_0(A_m)e^{i\omega t} + J_1(A_m)e^{i(\omega+\omega_m)t} - J_1(A_m)e^{i(\omega-\omega_m)t}\right] \end{aligned} \tag{3.13}$$

This wave can be seen a superposition of three waves at frequencies $\omega - \omega_m$, ω and $\omega + \omega_m$. Here the radiation at frequency ω is called the carrier wave and the other are called side bands.

This beam is sent to the cavity and after reflection from the cavity it gets a transformation. If we have a cavity with mirror's reflectivity r and separation between the mirrors L then the transfer function is

$$R(\omega) = \frac{E_{ref}}{E_{in}} = \frac{r\left(e^{2i\omega L/c} - 1\right)}{1 - r^2 e^{2i\omega L/c}} \tag{3.14}$$

here ω is the frequency of the incident beam. The reflected intensity is zero when $e^{2i\omega L/c} = 1$ known as resonance condition and the frequency at which this is satisfied is called resonance frequency. The separation between these resonance frequencies is equal to the *free spectral range*.

Thus after the reflection from the cavity the radiation field 3.13 get transformed to

$$E_r = E_0\left[R(\omega)J_0(A_m)e^{i\omega t} + R(\omega+\omega_m)J_1(A_m)e^{i(\omega+\omega_m)t} - R(\omega-\omega_m)J_1(A_m)e^{i(\omega-\omega_m)t}\right] \tag{3.15}$$

where each of the wave components get transformed according to their frequency.

This beam is seen by the photodiode which converts it to a voltage proportional to the intensity $E_r^* E_r$. In figure 3.16a $E_r^* E_r$ is plotted against the scan frequency ω which shows resonance of carrier wave and two side bands separated by the frequency ω_m. However if we look on the transmission signal we see a signal proportional to $1 - E_r^* E_r$. The strength of the side bands depends on $J_1(A_m)$ and hence on the amplitude of the phase modulation A_m.

The expression of the power on the photodiode is

$$\begin{aligned} P = {} & P_c|R(w)|^2 + P_s\left\{|R(\omega+\omega_m)|^2 + |R(\omega-\omega_m)|^2\right\} \\ & + 2\sqrt{P_c P_s}Re\left[R(\omega)R^*(\omega+\omega_m) - R^*(\omega)R(\omega+\omega_m)\right]cos(\omega_m t) \\ & + 2\sqrt{P_c P_s}Im\left[R(\omega)R^*(\omega+\omega_m) - R^*(\omega)R(\omega+\omega_m)\right]sin(\omega_m t) \\ & + (2\omega_m\ terms) \end{aligned} \tag{3.16}$$

where P_c and P_s are the powers in carrier and side bands.

The error signal is processed out from this signal. The sinusoidal terms of ω_m are canceled by mixing the signal which is sent to the EOM after adding a phase to it i.e. $sin(\omega_m t + \phi)$ to this signal. The high frequency terms in the last term are filtered out by a low pass filter. The figure 3.16 plots the terms

$$\begin{aligned} & 2\sqrt{P_c P_s}Re\left[R(\omega)R^*(\omega+\omega_m) - R^*(\omega)R(\omega+\omega_m)\right]cos(\phi) \\ & \quad + 2\sqrt{P_c P_s}Im\left[R(\omega)R^*(\omega+\omega_m) - R^*(\omega)R(\omega+\omega_m)\right]sin(\phi) \end{aligned} \tag{3.17}$$

as a function of ω which is sent as feedback to the laser.

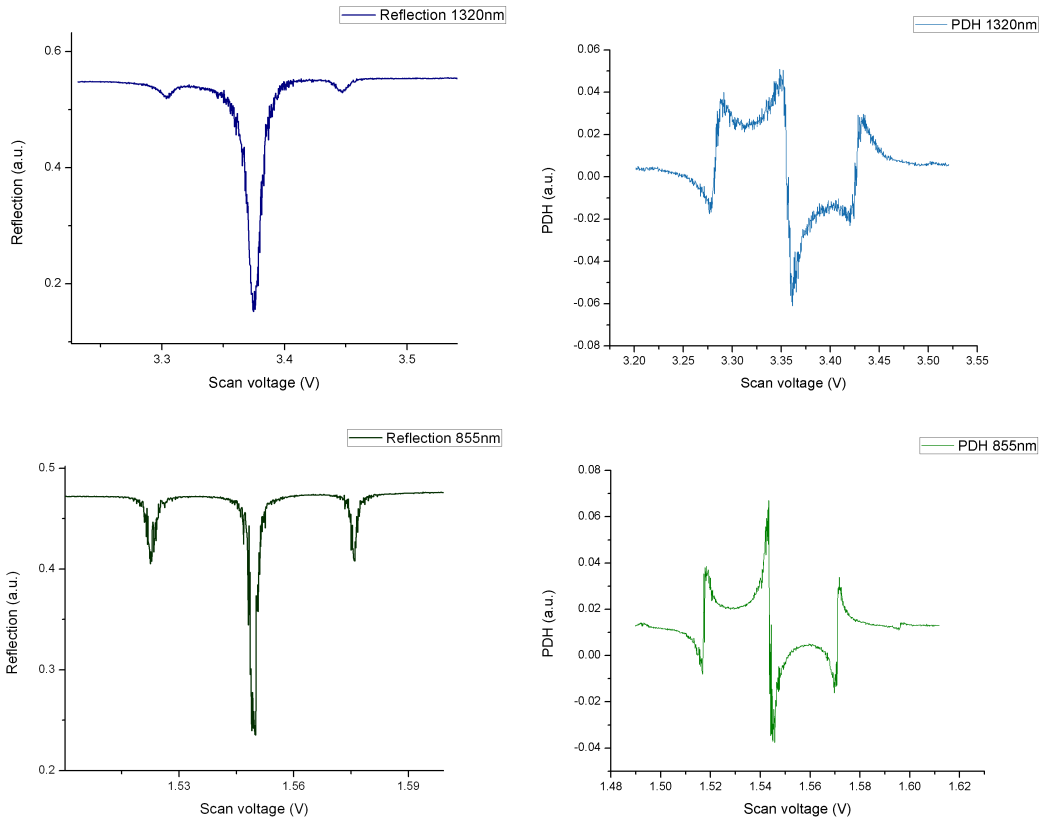

TABLE 3.2: Left: The reflection signals from the cavity with the side bands generated by the phase modulation of the injected beam. Right: The Pound Drever Hall error signal after mixing the transmission signal with a phase shifted local oscillator.

In practice the phase ϕ can depend on many experimental factors and has to be tuned to achieve the best error signal. Figure 3.2 shows the optimized reflection signals and PDH signals for both the lasers and they are in agreement with the simulations. After optical alignments, these signals are optimized using the modulation amplitude and the phase. In the reflection signal, the strength of the side bands can be adjusted by the amplitude of the modulation sent to the EOM. The side bands extract the power form the career wave, therefore a too high modulation amplitude will decreases the strength of the career's reflected signal, which will lead to a poor slope in the error signal. Modulation amplitude and the phase added using the phase shifter are tuned to maximize the slope of the error signal.

3.4.2 Cavity linewidth using the EOM modulation

The transmitted signal from a cavity (given by $T = 1 - R$, where R is the reflected signal) shows a peak at the resonance. The modulation in the phase using EOM adds two side peaks to the career frequency (figure 3.17). Since the side peaks are separated from the central peak by 12.5 MHz it is possible to scale the width of the central peaks

in the units of frequency more precisely. From curve fitting the linewidth of the cavity is calculated to be 2.67MHz.

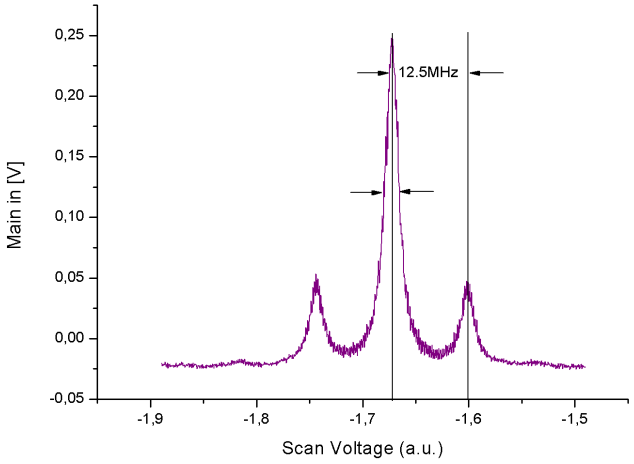

FIGURE 3.17: Line width calculation using the side peaks produced by the EOM in the transmission line.

3.4.3 Feedback

The feedback to lock the laser is divided into two parts and sent to the laser-cavity piezo and laser current separately. The low frequency part of the feedback also known as slow feedback is sent to the laser piezo because a piezo cannot respond fast to the voltage. The high frequency feedback (>100Hz) is sent to the laser current. The PID (Proportional Integral Derivative) values of the individual feedbacks and their overall gain values were adjusted to give the smallest error signal once locked.

Linewidth estimation after the lock

After the feedback is sent to the laser and the PID values are optimized the line width can be roughly estimated from the RMS value of the error signal.

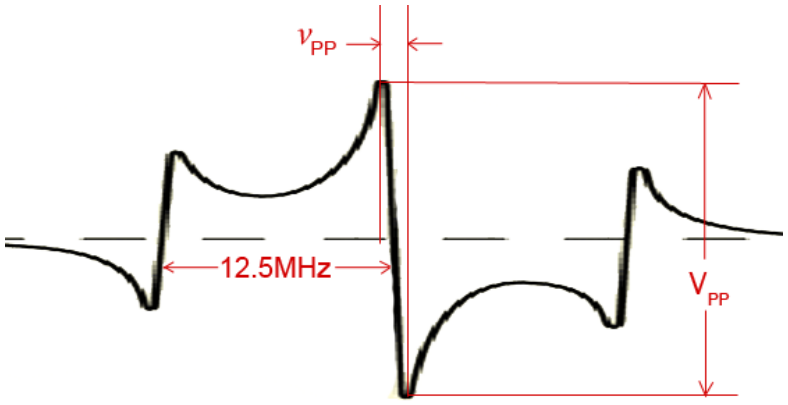

FIGURE 3.18: The fluctuations in error signal can be transformed into frequency fluctuations.

For a very precise frequency noise detection (∼Hz) one has to measure the noise on the phase through phase detection. However for the range of kHz the frequency noise can be estimated from the noise on the error signal after the lock. The noise on the error signal $\Delta\nu$ is converted to the frequency noise using the formula

$$\Delta\nu = \frac{\nu_{PP}}{V_{PP}}\Delta V \tag{3.18}$$

where V_{PP} is the peak to peak voltage value for the central slope of error signal and ν_{PP} is the corresponding frequency difference as shown in figure 3.18.

3.5 Noise spectrum

One of the most powerful ways to find the noise on any signal in different band width ranges is to analyze its noise spectrum using a spectrum analyzer. In general a spectrum analyzer has its own specification like resolution and its integration time which limits the frequency window in which it works. The requirement needs to be taken care is that the frequency range in which we want to analyze a noise must be within the range of the spectrum analyzer.

3.5.1 Power spectral density

The power spectral density of a signal (electromagnetic, electric, acoustic etc) is the distribution of power carried by the signal over the frequencies. It is normally measured in WHz^{-1}, however in case of electrical signals as in our case it is measured in $\mathrm{V}^2\mathrm{Hz}^{-1}$. We lock the lasers using the PDH scheme to a set-point *zero* (V=0) of the error signal.

When it is locked, we want to reduce the fluctuations from this set-point. Ideally we want that the error signal after the lock approaches to zero which implies that the power spectral density of the error signal ($\sim V^2$) after the lock must also go to zero. However in an experimental setup the error signal after the lock has a non-zero power spectral density which corresponds to the noise (fluctuations from the set-point) over the lock.

3.5.2 Calculation of line-width

Parseval's theorem

A very general statement of Parseval's theorem is that the sum (or integral) of the square of a function is equal to the sum (or integral) of the square of its transform. In the context of power spectral density it can be stated that the area under the power spectral density curve is equal to the area under the square of the magnitude of the signal.

$$\int_{-\infty}^{\infty} |f(t)|^2 \, \mathrm{d}t = \int_{-\infty}^{\infty} \Phi(\omega) \, \mathrm{d}\omega \tag{3.19}$$

here $f(t)$ is the signal and $\Phi(\omega)$ is given by

$$\Phi(\omega) = \left| \frac{1}{\sqrt{2\pi}} \int_{-\infty}^{\infty} f(t) e^{-i\omega t} \, \mathrm{d}t \right|^2 \tag{3.20}$$

RMS noise

In a case where the ideal situation is the zero power spectral density, the finite value of the power spectral density (PSD) corresponds to the noise. The noise power can be calculated by integrating the area under the PSD. And then the root mean square value of the noise can be calculated by taking its square root.

$$NoisePower = \int_a^b S(\omega) \, \mathrm{d}\omega \tag{3.21}$$

where $S(\omega)$ is the spectrum and a to b is the frequecy range in which we want to compute the noise.

$$RMSNoise = \sqrt{NoisePower} \tag{3.22}$$

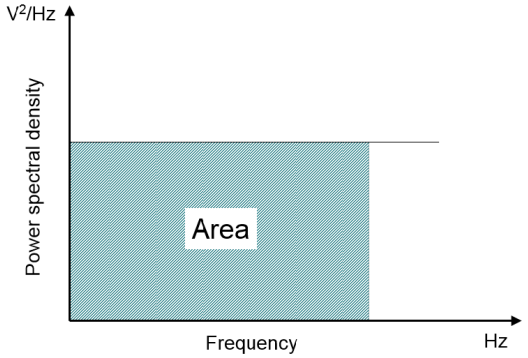

FIGURE 3.19: Area under the power spectral density curve.

Spectrum of error signal

The spectrum of the error signal after lock for different feedback (overall) gain values is shown in figure 3.20 and 3.21 in logarithmic and linear scale.

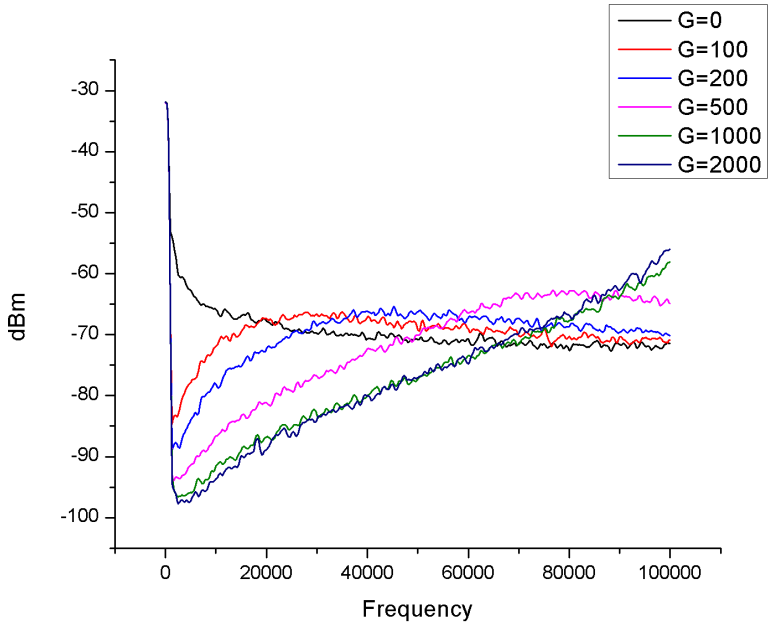

FIGURE 3.20: The spectrum of the error signal after the lock with different PID gain values.

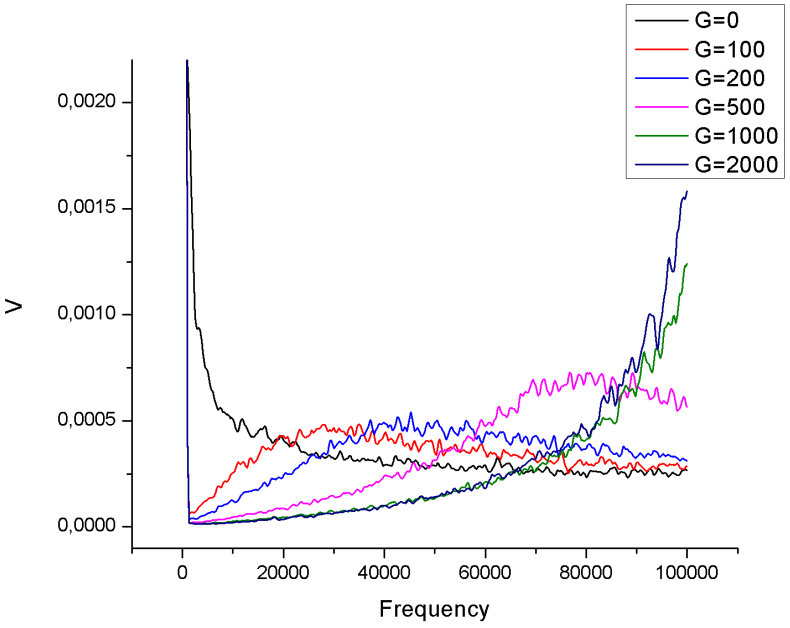

FIGURE 3.21: The spectrum of the error signal in linear scale the lock with different PID gain values.

In order to calculate the linewidth after the lock, the spectrum data points which are in logarithmic scale (dBm) are converted into the power units (V^2/Hz). After that area under the PSD is integrated and using equations 3.21 and 3.22 the RMS noise on the error signal is calculated. This noise is converted into frequency noise using equation 3.18. Table 3.3 summarizes the line width calculated from the spectrum shown in figure 3.21 within the detection bandwidth of 50KHz.

Gain	Linewidth
0	40kHz
100	25kHz
200	20kHz
500	10kHz
1000	7kHz
2000	5kHz

TABLE 3.3: The line width after lock within the detection bandwidth of 50kHz for different PID gain values.

3.6 Phase locking

3.6.1 Frequency comb

Frequency comb is a light source whose spectrum is composed of discrete frequency peaks with equal separation. These equally spaced frequency peaks are a perfect frequency ruler reference for the phase stability of two or more lasers. The spectrum of a comb is similar to a Dirac delta comb however with a finite spectrum range. Hence in the time domain its output is a train of short intensity pulses as shown in figure. The broader is the spectral range of a comb the shorter are the pulses in the time domain. Because of dispersion and nonlinearities in the source, the envelope of the intensity pulse suffers a phase slip with respect to the oscillating electric field (shown in figure 3.22). In the frequency spectrum this phase slip is reflected as an offset from the zero as shown in figure 3.23.

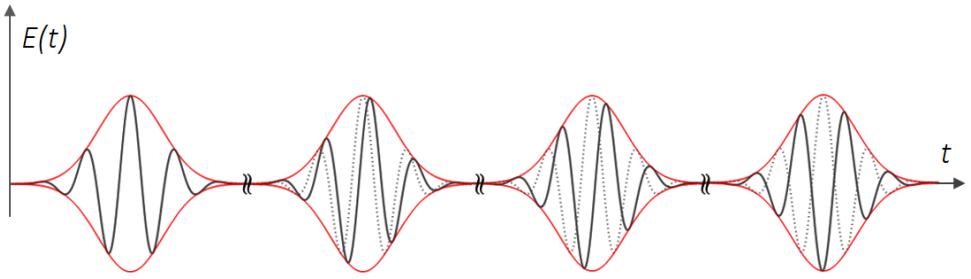

FIGURE 3.22: Pulse train emitted from a frequency comb with a phase slip of the envelope.

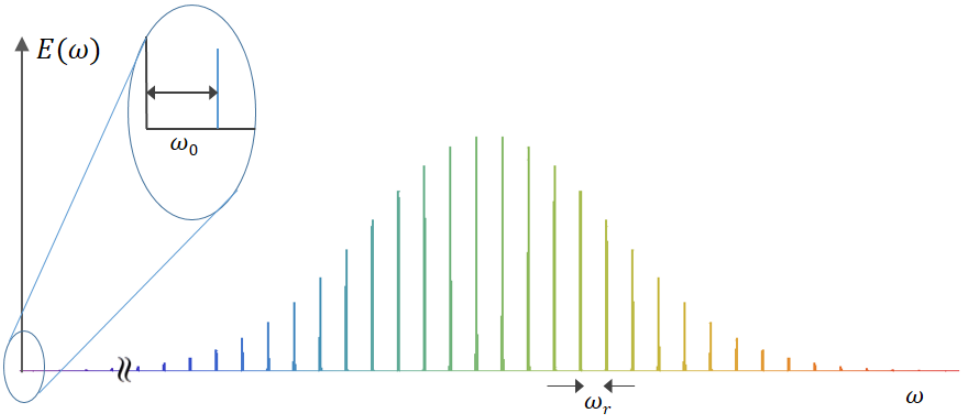

FIGURE 3.23: The spectrum of a frequency comb with offset of first frequency mode from zero.

A general expression for the frequency output of a frequency comb can be written as

$$\omega_n = n\omega_r + \omega_0 \tag{3.23}$$

where n is an integer, ω_n is the frequency of n^{th} peak, ω_r is the frequency separation between the peaks called as repetition rate frequency, ω_0 is the offset frequency.

In our setup we used a commercial frequency comb manufactured by MenloSystems (model: FC1500 Optical Frequency Synthesizer) which has a spectral range from 1 to 2 microns and a repetition rate of 250MHz. The output power was measured to be 100mW. In order to lock the 855nm laser this light is frequency doubled to obtain a frequency range peaked at 855nm.

3.6.2 Locking scheme

The phase locking of two laser which are line narrowed using an external optical cavity, can be done by beating the laser light with the frequency comb light. This beat signal can be precessed into an error signal and can be fed to the piezos of the cavity to which the lasers are locked. And for stability the frequency comb can be locked to a Rb clock which is disciplined by GPS (Global Positioning System) clock. This scheme is shown in figure 3.24. The ultimate stability reference in this scheme is the GPS controlled Rb clock signal, which is used to stabilize the comb. The comb is used to stabilize the external optical cavities which in the end are used to stabilize the lasers. The Rb/GPS-disciplined 10-MHz quartz have a stability of 6×10^{-13} at 1 s and a minimum accuracy of 2×10^{-12}.

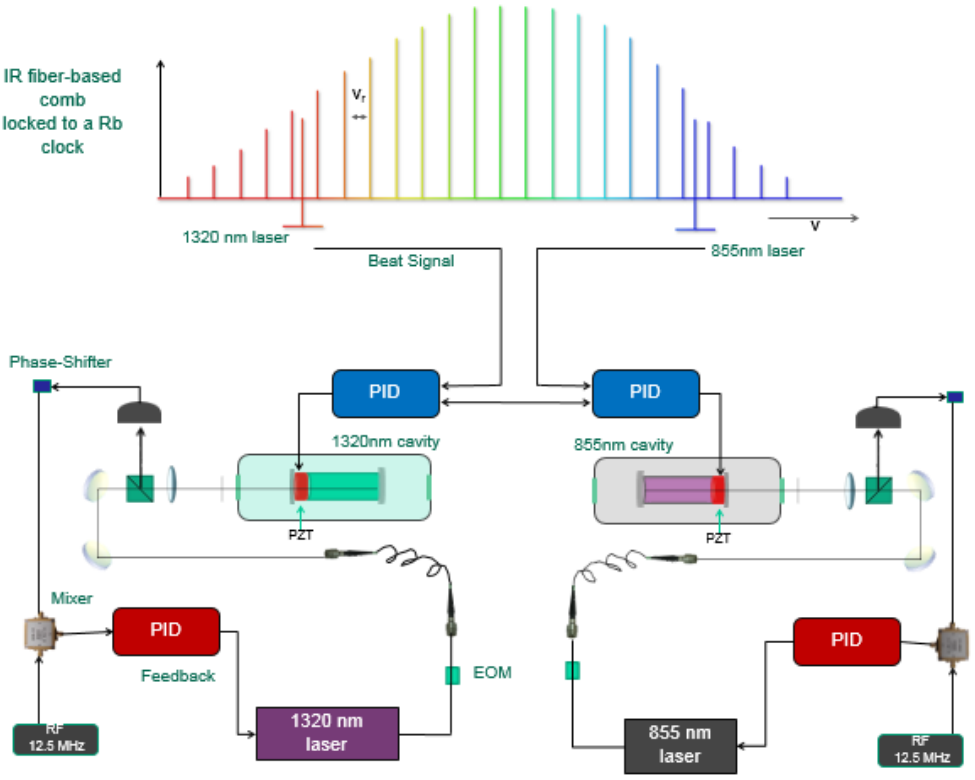

FIGURE 3.24: The locking scheme of the two lasers stabilized to an external cavity to an optical frequency comb.

Stabilizing the frequency comb

In a frequency comb, due to various types of noise both frequency offset ω_0 and repetition frequency ω_r can fluctuate. In order to make a comb stable its offset and repetition frequency need to be locked to a stable signal. The repetition frequency can be accessed easily by the self beating of the comb teeth. The offset frequency is accessed by doubling the 2100nm part of the comb and beating it with the 1050nm part, as demonstrated in figure 3.25.

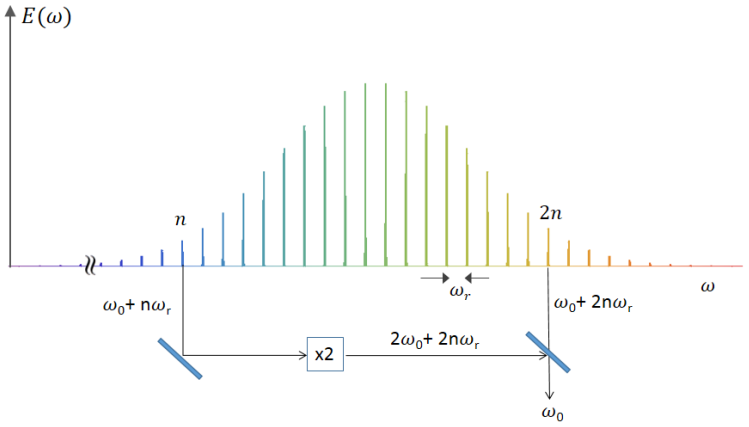

FIGURE 3.25: The scheme to access the offset frequency.

These frequencies are locked using 10MHz clock as reference. After locking the stability of the repetition frequency is 250 ($\pm 10^{-9}$)MHz and the offset frequency is 20 ($\pm 5 \times 10^{-6}$)MHz with respect to the clock signal.

Beating

The beat frequency between laser and the comb is measured on a fast photodiode. The set of beats seen by the photodiode includes the self beating between the comb teeth, the beat between the laser frequency and the two nearest teeth and beating between the laser frequency and the rest of the teeth. Out of these the beating of our interest is the one with the nearest (in frequency) tooth. Hence the value of this beat is less than 250MHz and can be detected by the photodiode. The other beats being at higher frequency are out of range of the photodiode and hence just add to the offset. This offset can be enough to even hide the beat signal.

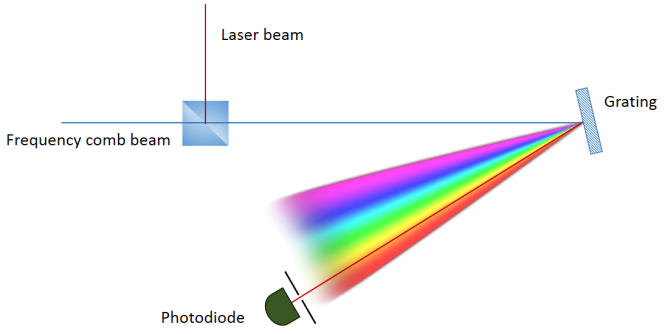

FIGURE 3.26: Beat unit used to detect the beat between laser and the nearest comb teeth.

In order to avoid this offset we use a grating to separate out the frequency teeth which are closer to the frequency of the beating laser. This is illustrated in figure 3.26. After reflection from the grating the different frequency component of the frequency comb spreads angularly. The components which go along with the laser are those which are closer to the laser frequency. The strength of the beat signal after the spread depends on the power of both the frequencies (laser and comb) which are beating. In the case of comb the power per frequency component is much less as compared to the total power. Also sending more power of the frequency comb results in both increase of the beat signal strength as well as the offset. Therefore the signal can be improved by sending more power of the laser for the beating.

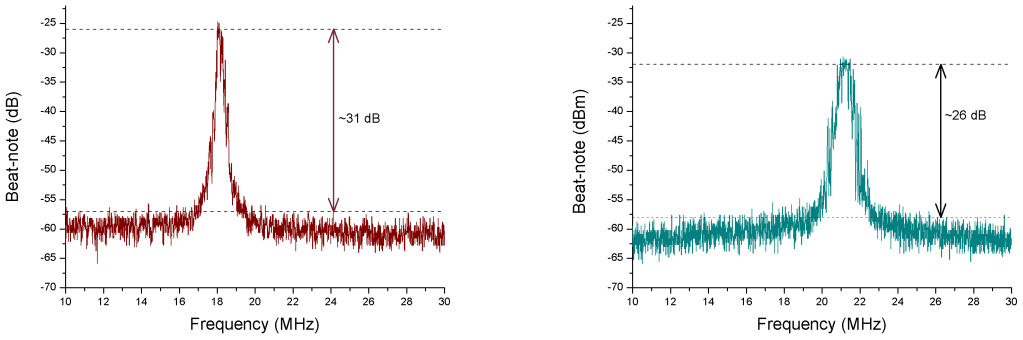

FIGURE 3.27: Beat signal from the frequency comb beating with 1320nm laser (left) and 855nm laser (right).

For our phase locking system the requirement of the beat signal strength is nearly 30dBm. Figure 3.27 shows the beat signal of the 1320nm laser and the 855nm laser.

Locking

The beat signal is locked using a phase locked loop (PLL). In this locking the beat signal between the laser and the comb is detected on a photodiode. This beat signal and a signal from the reference local oscillator (20MHz in our case derived from the 10MHz Rb clock) are sent to a phase detector which forms the phase difference between the two signals. This signal is processed and fed to the laser. (In our locking scheme this feedback is sent to the external cavity to which laser is locked.)

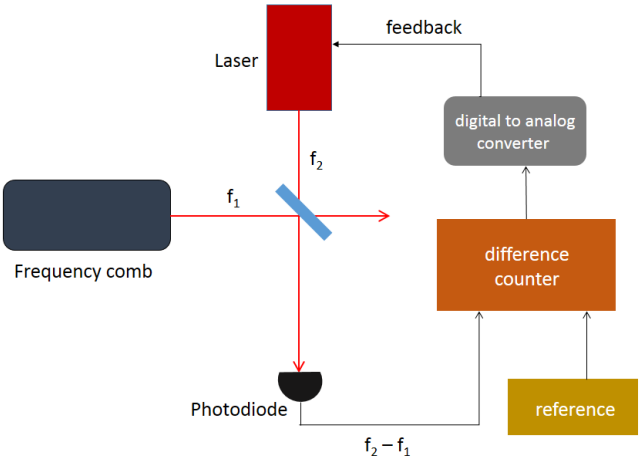

FIGURE 3.28: The schematic of the phase locking of the laser to the comb.

The phase difference measured in radians can vary from zero (in case of perfect match) to any value, however from the phase detector it is seen only varying from $-\pi$ to π as shown in figure 3.29. This sawtooth like signal becomes broad in time when the beat signal is close to the reference and becomes flat after the lock.

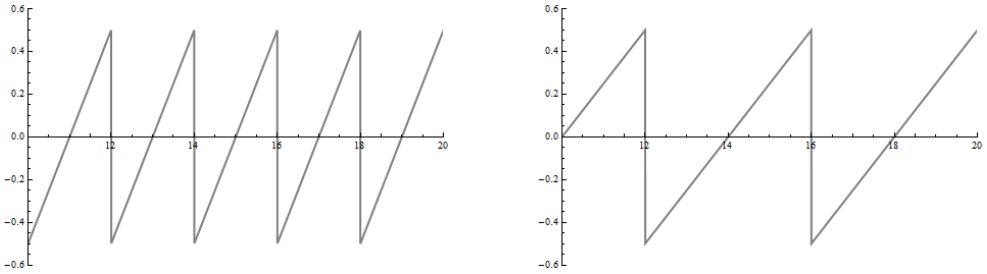

FIGURE 3.29: The phase difference between the beat signal and the reference signal, which changes continuously with time but seen like sawtooth because of the $+/-\pi$ bound on the angle.

Figure 3.30 shows the actual display panel before and after locking the laser to the comb using the beat signal. After locking the Allan variance is less than 10Hz.

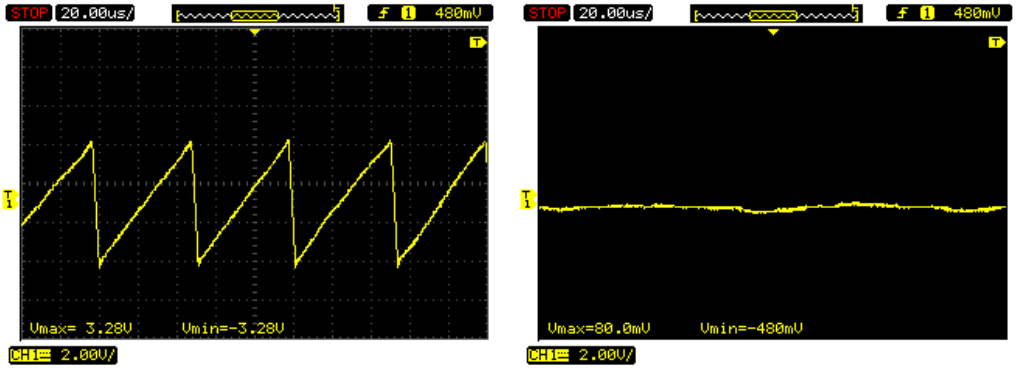

(A) Error signal without locking. (B) The error signal after the lock.

FIGURE 3.30: The display panel showing the digitized error signal (phase difference) before and after lock.

3.7 Wavemeter

To measure the absolute frequency of the lasers we made a wavemeter based on moving Michelson interferometer with the varying path length in both arms using a running corner cube. A He-Ne laser is used as the reference laser, with a frequency at 473612298 MHz with an accuracy of 6 MHz.

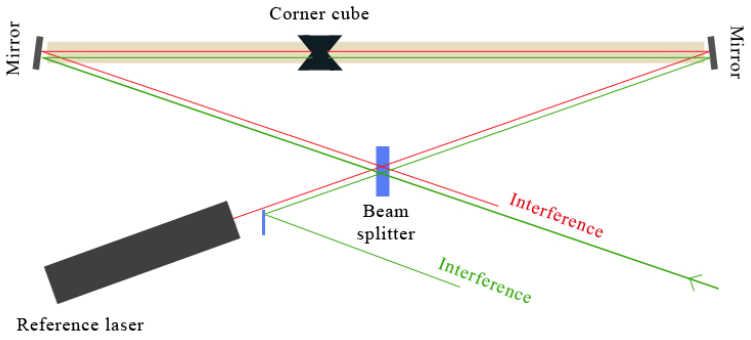

FIGURE 3.31: Schematic diagram of the wavemeter based on moving Michelson interferometer.

As shown in figure 3.31 a corner cube runs between the two mirrors at nearly constant speed. The beam from the reference laser splits from the beam splitter and via reflection from the mirrors, falls on the corner cube. After reflection from the corner cube it follows back the a same length parallel path and interferes after passing through the beam splitter. The unknown laser beam follows a similar path but from the other side of the beam splitter. At the interference we see consecutive maximas and minimas along the beam which are detected on the photodiode. From the photodiodes the signal is sent to

a universal counter which counts the maximas for both the inferences and gives us their ratio. Both interferences are scanned simultaneously while cube is moving. Since the rate at which the path difference is changing is same for both the lasers so the ratio of the numbers of fringes counted over a fixed time are same as the ratio of the wavelengths of two lasers.

$$\lambda = \frac{N_r}{N}\lambda_r \tag{3.24}$$

here N is the number of interference maximas, λ is the wavelength of the laser and the index r refers to the reference laser.

The accuracy of this wavemeter can be increased by increasing the number of fringes counted, thus running the corner cube over a large path helps in terms of accuracy. However the speed of the cube should not be too fast for the counter. Apart from the optical alignment the interference fringes are very sensitive to the collimation of the beams.

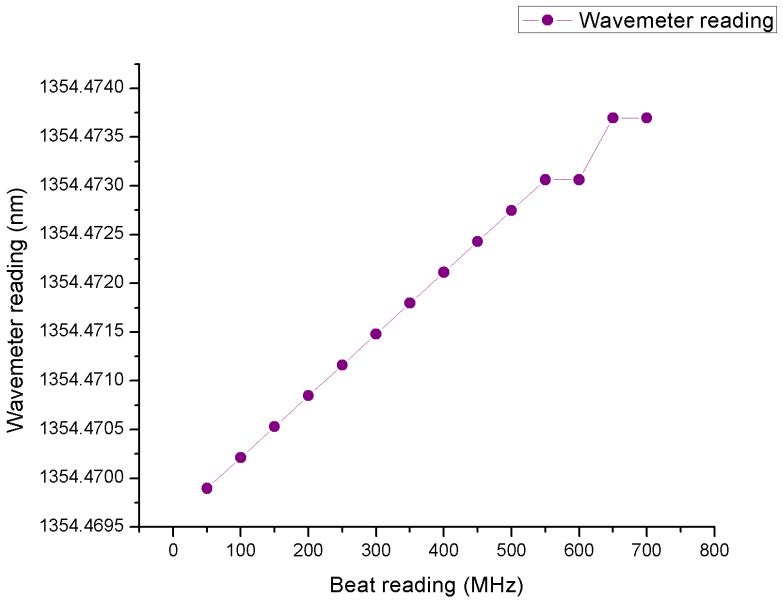

FIGURE 3.32: The wavemeter reading versus the beat signal with one of the frequency comb lines. From the plot it is clear that we can estimate the frequency of the laser upto an accuracy of ∼50MHz by doing repeated measurements.

In our wavemeter the length of the rail is 1100mm. During measurements of the wavelength we counted the fringes while the corner cube completes one full cycle between the mirrors (2200mm) at a speed of nearly 0.25m/s. Therefore we count typically of the order of 10^8 fringes. In the interference fringes the fringe contrast can be calculated as

$$C_{fringe} = \frac{I_{max} - I_{min}}{I_{max} + I_{min}} \tag{3.25}$$

The experimentally observed fringe contrast was 71% for the He-Ne laser, , 90% for the primary (1320nm) laser and 84% for the secondary (855nm) laser. Figure 3.32 shows the wavelength estimated using this wavemeter versus the beat note of the same laser with one of the lines of frequency comb. These measurements were done to estimate the least count of the wavemeter by precisely setting the beat note to a value and then estimating the wavelength of the laser from the wavemeter reading. From a linear fit the least count of the wavemeter is estimated to be 50 ± 1MHz.

3.7.1 Wavemeter and Frequency comb

The frequency comb can be used to find the frequency of the laser from the beat signal. The accuracy of the wavemeter alone is limited to 50MHz. But this accuracy is enough to find out with which comb tooth the laser is beating with. Because the repetition frequency of the comb is 250MHz. If N be the tooth number with which the laser is beating the frequency of the laser can be calculated as

$$\nu = \omega_0 + N\omega_r \pm \nu_b \tag{3.26}$$

here ν_b is the beat frequency, the sign $\pm$ depends from which side the laser is beating with the comb tooth which can be found easily by changing any of laser frequency parameter. Using this method the frequency of the laser can be estimated within an accuracy of 2MHz.

3.8 Conclusions

For the requirements of the STIRAP transfer the lasers are needed to be line narrowed to $<$ 10kHz. For this I built an external high finesse Fabry Perot cavity to lock each laser, and stabilized it by mounting it in a temperature stabilized vacuum chamber. The lasers are line narrowed by locking them to these stable cavities. I reportedly discuss the stabilization scheme and the apparatus we used to line narrow the diode laser using the external cavity. Finally using the power spectral density, the linewidth of the lasers are reported to be 5kHz in the bandwidth of 50kHz.

To stabilize the relative frequency noise of the lasers, they are locked to a commercial optical frequency comb (manufactured by MenloSystems). For the locking, they are beat with the comb, and beating with the nearest tooth was filtered out and enhanced to improve the lock. After phase locking to two teeth of the comb the relative stability of the lasers is accomplished to $\sim$1kHz. The frequency comb is locked to an ultrastable

Rb/GPS-disciplined 10MHz quartz clock. This clock have a stability of 6×10^{-13} at 1 s and a minimum accuracy of 2×10^{-12}.

For the molecular transfer, in the first step we will do association spectroscopy, in which we will excite the Feshbach molecules to the excited hyperfine states, just by scanning the primary laser. Therefore the tuning characteristics of the primary laser (1320nm) with various methods going from the most fine to the coarse one have been reported. To measure the absolute frequency of the laser I have build a wavemeter which is based on moving Michelson interferometer. This wavemeter is aligned to a fringe contrast of nearly $\sim$84% and its measuring accuracy is achieved to 50MHz. By using the wavemeter as well as the beat signal from the frequency comb, the accuracy of the frequency measurement can be reached to 2MHz.

Bibliography

[1] J. D. Weinstein, R. deCarvalho, T. Guillet, BretislavFriedrich, and J. M. Doyle, *Magnetic trapping of calcium monohydride molecules at millikelvin temperatures*, Nature 395, 148 (1998).

[2] H. L. Bethlem, G. Berden, and G. Meijer, *Decelerating Neutral Dipolar Molecules*, Phys. Rev. Lett. 83, 1558 (1999).

[3] J. M. Sage, S. Sainis, T. Bergeman, and D. DeMille, *Optical Production of Ultracold Polar Molecules*, Phys. Rev. Lett. 94, 203001 (2005).

[4] K.-K. Ni, S. Ospelkaus, M. H. G. de Miranda, A. Péer, B. Neyenhuis, J. J. Zirbel, S. Kotochigova, P. S. Julienne, D. S. Jin, and J. Ye, *A high phase-space-density gas of polar molecules*, Science 322, 231 (2008).

[5] W. C. Stwalley *Efficient conversion of ultracold Feshbach-resonance-related polar molecules into ultracold ground state ($X^1\Sigma^+$ $v = 0$, $J = 0$) molecules*, EPJD, 31, 221 (2004).

[6] Eric D. Black, *An introduction to Pound–Drever–Hall laser frequency stabilization*, Am. J. Phys. 69 (1), January 2001.

Acknowledgements

Though only my name appears on the cover of this dissertation, many others have contributed to its production. I therefore take this opportunity to thanks all those people from the bottom of my soul, who have made this thesis possible and because of whom my PhD experience has been one that I will cherish for the rest of my life.

First and foremost, my hearty thanks and deep sense of gratitude to my supervisors Prof. Giovanni Modugno, who without their inspiration, knowledge, guidance and motivation, none of this would be possible. Then I heartedly thank Prof. Massimo Inguscio for giving me opportunity to work within the group of Quantum gases at LENS. I want to express gratitude to my referee Prof. Gabriele Ferrari from BEC center, Trento for taking time to review this thesis report.

I deeply thank Dr. Saptarishi Chaudhuri for everyday guidance and motivations towards being a researcher. A special thanks to my seniors and colleagues Dr. Chiara D'errico, Dr. Eleonora Lucioni, Luca Tanzi and Lorenzo Gori for their day to day guidance to run the BEC setup and various scientific discussions.

I am also sincerely thankful to my Indian friends Vasanth, Rajesh, Bhushan and Suresh from Florence. My childhood friends Bhatia, Batish and Vinay have been great motivators throughout my career in science. In the process of admission to the PhD program I have no words to thank my friend Harish Kumar for doing all the bureaucratic work for me.

My family is always source of inspiration and great moral support for me in perceiving my education, it is impossible to express my sense of gratitude for my family: Mom, Dad, both Chachu and both Chachi, grandmother and my late grandfather in mere words. My sisters Arti, Neha, Sofia and Mayu have added colors to my life.

In the last most importantly I respectfully thank my spiritual guru Asaram bapu whose daily teachings helped me to make my path towards spirituality and successful life.